
Part I

The Thesis

CHAPTER 1

INTRODUCTION

1.1 Motivation

The principal motivation for this work is the analysis of different nanoparticles following two concepts:

First, the use of second-order nonlinear optical effects that are very effective for surface analysis.

Second, the use of a special technique for optical spectroscopy – the two beam, cross-polarized second harmonic/sum-frequency generation (XP2SHG/SFG) technique.

Metallic nanoparticles are currently a “hot topic” in the scientific world because the scope of their potential applications is very large, from biological applications [1], imaging and detection [2, 3, 4], and more [5, 6]. Silicon nanoparticles, although more common, are not far behind – their use in new solar cell technologies [7] and biological markers [8] are also cutting edge research.

None of the techniques described in this thesis are particularly new, but they have been used with great success in a variety of different materials. Although some literature exists on metallic nanoparticles characterized by these techniques, there is a relatively small amount of research on the subject. The optical methods included here are both non-destructive and potentially surface specific. Combining these with interesting nanostructures may prove to be a promising path for future developments in the nanosciences.

The focus of this thesis will be the study of second-order nonlinear effects in nanosystems. Nanoparticles have huge surface to volume ratios because they are so small; they contain few atoms and the bulk is tiny compared to the outside surface. The second-order nonlinearities, second harmonic generation (SHG) and sum-frequency generation (SFG), are both suitable for spectroscopic analysis of nanoparticles. These can be greatly enhanced using the two beam, cross-polarized SHG/SFG (XP2SHG/SFG) technique [9]. The purpose of this work is to study the properties of these nanostructures using the aforementioned methods.

1.2 Nonlinear Optics in a Nutshell

Linear optics has long dominated the study of light. Much like Newton's mechanics, it describes an incomplete picture of the interaction between light and the matter that forms our world. This is not to say the picture is incorrect; the interactions described work for our everyday situations. We call them "linear" because matter interacts in a directly proportional way with the electric field of the incoming light. The linear response of most materials is more appreciable than the other responses, making them difficult to observe – we call these "nonlinear effects." We will elaborate further on this point in chapter ??.

We can approximate most potentials within the atom using a harmonic oscillator model. These potentials represent the effect electrons feel when confined. They restrict the way electrons can move and determine many of the important material properties. These can tell us whether a material would make a good semiconductor for an optical device or for a computer microprocessor, or would make a very conductive metal, amongst many other things.

An example of a harmonic oscillator is a spring with a mass on one end. The other end is fixed and unmovable. If the mass is moved a little ways away from the equilibrium point and released, the mass will begin to oscillate for some time until it eventually stops once again at equilibrium (as it is dampened by gravity or friction). However, if you pull the spring too far it can deform from all the extra force. The spring follows a linear response according to the well established SHO equations when the displacement is small. Larger displacements are unaccounted for in this model – now we are talking about *nonlinear* behavior.

So the electrons behave in a similar manner if we model our electronic potentials as SHOs. This model works well for low intensities of incoming light, when the electron is displaced only a little from the "bottom" of the potential well. This provides the linear response between light and matter and is the reason why linear interactions dominate our everyday life. Although the light is very intense, the radiation that does reach us is spread out over half our world. Even when focused down to a very bright point it lacks the ability to deliver energy in an organized and efficient way. So our everyday light can only give electrons a little bit of energy and they move accordingly. Even the sun cannot provide the necessary conditions to allow electrons to move significantly from the bottom of a potential well.

We had the sun and different light bulbs, and used them often for experiments. I just explained why these sources can't help us past the linear

regime. So people were stuck with this problem for a long time until a new light source, the LASER, was invented. LASER is an acronym for *Light Amplification by Stimulated Emission of Radiation*. One of the main characteristics of a laser is that it emits an energetic, unidirectional, coherent beam of light that can be focused to a very small spot further concentrating the energy.

This discovery revolutionized optical science. The laser was precisely what was needed to produce high energy densities that could move the electrons away from the bottom of the potential well. Experimentalists starting shooting lasers into all kinds of materials – and just like the spring and mass, the model stopped describing the experiment and all sorts of strange things started happening.

In this way we discovered nonlinear optics. These strange effects were difficult to explain at first. A new model had to be devised and tested against the experiments. Fortunately, it was not very long before one was created and found to work; not only did it explain everything observed until then, but it also predicted many things that had not yet been discovered [10, 11, 12]. I will elaborate on the math of this new model in chapter.

SHG, a special case of SFG, was one of the first observed, and predominant optical nonlinearities that can appear from many substances. While all materials are technically nonlinear, the response of most are not appreciable for low intensities of incoming light, and are destroyed before we can see the effects. Some metals and semiconductors are excellent nonlinear materials, as are many different crystals. SHG is usually the first nonlinear effect to appear and can be the easiest to produce. As we will explain in section , it is often attributed to surface emission which makes it an excellent tool for studying and characterizing surfaces and interfaces.

1.3 Outline

This thesis is divided into 5 chapters including this introduction. Chapter details the mathematics, formalism, and theory that make up our description of nonlinear optics. Chapter describes the materials to be characterized and the experimental setup used to study them. Chapter consists of the experimental data and analysis, with comparisons to existing literature. Finally, chapter is dedicated to the final observations and remarks. The complete bibliography is located at the end of the document for easy reference.

1.4 A Review of Nonlinear Optics

1.4.1 Historical Overview

The discovery of the optical maser by Townes [13] and the construction of the laser by Maiman in the late 1950s and early 1960s ushered a new age of optical discoveries. The ability to produce optical beams with these devices automatically lead to very highly focused energies distributed over very small areas. These concentrated energies allowed scientists to finally move into the optical nonlinear regime for many different materials.

The optical maser allowed for the first recorded observation of optical SHG by Franken et al. in 1961 [14]. They produced a second beam of light at twice the frequency of the original by exciting a piece of crystalline quartz. This frequency doubling effect was dubbed SHG and was observed to be much less intense than the exciting beam.

There is a humorous anecdote about this experiment. Apparently, the editor of Physical Review Letters thought that the second harmonic dot on the photographic plate was a speck of dust, which he edited out. The image found in the article has an arrow pointing at the empty spot where it should be. However, this did not detract from the importance of the find.

Other developments followed promptly. In 1962, Bloembergen et al. [15, 16] developed the mathematical framework to explain nonlinear optical phenomena. That same year, Terhune et al. [17] observed SHG in calcite. These discoveries were amongst others [18] that lead to further research into the geometrical dependence of nonlinear effects, and helped verify that the majority of the SHG signal produced in a centrosymmetric material comes from surface contribution, where inversion symmetry is broken.

In the late 1960s, Bloembergen [19] and others [20] studied SHG in a variety of centrosymmetric materials and semiconductors. The advent of pulsed lasers during the 1970s [21] allowed for even greater intensities to be obtained. Dye lasers came to prominence during these years, offering very large bandwidths and relatively short picosecond pulses. However, these lasers were very difficult to maintain and the dyes used were typically very toxic and presented serious health risks.

Interest began to form around using SHG to study surfaces and interfaces, since it had been proven [22] to be exclusive to the surface area of a centrosymmetric material in the dipole approximation. Shen et al. published [23] that there is also a quadrupole bulk contribution for this kind of material, and in 1989 [24] published a review article summarizing most of the trends in surface spectroscopy using SHG. Theoretical work also played

an important role in the 1990s, with new theoretical models by Sipe [25] and others [26, 27, 28, 29]. Downer et al. [30] and Lüpke [31] both produced very thorough and referenced texts on SHG surface spectroscopy of semiconductors in the late 1990s and early 2000s. This period of time provided the foundations for surface optics today.

At around the same time, the first Ti:sapphire lasers were being produced and analyzed [32]. These early ultrafast lasers were capable of producing femtosecond pulses via mode-locked oscillators. Since the active medium is in solid state form, they present none of the risks of using dyes. These lasers were considerably more compact than dye lasers since they no longer needed external dye control systems. These lasers became commercial in the early 1990s.

Chirped pulse amplification (CPA) was invented in 1985 by Mourou and Strickland [33]. This technique allowed Ti:sapphire lasers to achieve much higher peak energy without compromising the ultrashort pulse duration. During the 1990s, CPA became the prominent method for increasing energy output in Ti:sapphire lasers. At this point, Ti:sapphire lasers using the CPA technique were both compact, efficient, and cost effective. These factors would only improve over the following decade as the Ti:sapphire laser became the standard for high energy, ultrashort pulse applications.

1.4.2 Defintion of Nonlinear Optics

As explained briefly in section 1.2, linear optics predominate in our everyday lives. The intensity of the light sources that surround us is typically not sufficient to modify the optical properties of a material. The discovery of the laser gave us access to higher intensity of polarized, directional, and coherent light. Beyond this, the ultrafast pulsed laser provides energy distributed into a much shorter time-frame which increases the peak irradiance delivered. These advances have greatly reduced the cost and effort needed to study nonlinear phenomena.

Light is nothing more than electromagnetic radiation, and is therefore composed of electromagnetic fields. This means that the study of how matter interacts with light is merely the study of how the light fields interact with the structure of matter. This can be readily appreciated for crystals and materials with very organized structures – in fact, the best nonlinear materials are almost always crystalline in nature.

Nonlinear Polarization and Susceptibility

So what happens when very intense light coincides on a given material? Let us talk about the dipole moment per unit volume, or polarization $\mathbf{P}(t)$. This polarization describes the effect light has on a material and vice versa; it represents the optical response of a material. Taking Maxwell's equations with the usual considerations of zero charge density ($\rho = 0$) and no free currents ($\mathbf{J} = 0$), we have

$$\nabla \cdot \mathbf{D} = 0, \quad (1.1)$$

$$\nabla \cdot \mu_0 \mathbf{H} = 0, \quad (1.2)$$

$$\nabla \times \mathbf{E} = -\mu_0 \frac{\partial \mathbf{H}}{\partial t}, \quad (1.3)$$

$$\nabla \times \mathbf{H} = \frac{\partial \mathbf{D}}{\partial t}. \quad (1.4)$$

We take into account the nonlinearity of the material by relating the \mathbf{D} and \mathbf{E} fields with the total (linear and nonlinear) polarization \mathbf{P} ,

$$\mathbf{D} = \epsilon_0 \mathbf{E} + \mathbf{P}. \quad (1.5)$$

Proceeding in the usual manner for deriving the wave equation, we obtain

$$\nabla \times \nabla \times \mathbf{E} + \frac{1}{c^2} \frac{\partial^2}{\partial t^2} \mathbf{E} = -\frac{1}{\epsilon_0 c^2} \frac{\partial^2 \mathbf{P}}{\partial t^2}, \quad (1.6)$$

which can be considerably simplified thanks to the identity

$$\nabla \times \nabla \times \mathbf{E} = \nabla (\nabla \cdot \mathbf{E}) - \nabla^2 \mathbf{E}. \quad (1.7)$$

The $\nabla (\nabla \cdot \mathbf{E})$ term is usually negligible (for instance, if \mathbf{E} is of the form of a transverse, infinite plane wave), so we can finally express the inhomogeneous wave equation as

$$\nabla^2 \mathbf{E} - \frac{1}{c^2} \frac{\partial^2}{\partial t^2} \mathbf{E} = \frac{1}{\epsilon_0 c^2} \frac{\partial^2 \mathbf{P}}{\partial t^2}. \quad (1.8)$$

In this form, it is clear that the polarization acts as a source for this differential equation and we can recall our oscillator example from section 1.2. The polarization can be expressed by a power series of the form

$$P(t) = \epsilon_0 \left[\chi^{(1)} E(t) + \chi^{(2)} E^2(t) + \chi^{(3)} E^3(t) + \dots \right] \quad (1.9)$$

$$\equiv P^{(1)}(t) + P^{(2)}(t) + P^{(3)}(t) + \dots, \quad (1.10)$$

where $\chi^{(n)}$ is the n^{th} -order susceptibility of the material. We can define the susceptibility as a constant of proportionality that describes the degree of polarizability a material has in terms of the strength of an incoming optical electric field. The first term

$$P(t) = \epsilon_0 \chi^{(1)} E(t), \quad (1.11)$$

is the linear term that describes most everyday interactions between light and matter. When taking into account that the incoming fields are vectorial in nature, the linear susceptibility $\chi^{(1)}$ becomes a second-rank tensor. $\chi^{(2)}$, the second-order nonlinear optical susceptibility is a third-rank tensor [10].

The nonlinear susceptibilities are very small in nature. If $\chi^{(1)}$ is unity, $\chi^{(2)}$ is on the order of $\approx 10^{-12}$ m/V. This explains why such high intensity fields are needed to produce nonlinear interactions – each term in equation (1.9) depends on a higher power of the incoming field but has a much smaller value for the corresponding susceptibility.

A more general definition of the nonlinear polarization can be found when treating the input field as a superposition of plane waves. We assume that the electric field vector is of the form

$$\mathbf{E}(\mathbf{r}, t) = \sum_n \mathbf{E}_n(\mathbf{r}, t), \quad (1.12)$$

where

$$\mathbf{E}_n(\mathbf{r}, t) = \mathbf{E}_n(\mathbf{r}) e^{-i\omega_n t} + \text{c.c.} \quad (1.13)$$

If we look at the form of equation (1.10), we can express the nonlinear polarization in its full form as

$$\mathbf{P}(\mathbf{r}, t) = \sum_n \mathbf{P}(\omega_n) e^{-i\omega_n t}. \quad (1.14)$$

Since we are only interested in second-order effects we can define the corresponding nonlinear polarization in terms of the second order susceptibility as

$$P_i(\omega_n + \omega_m) = \epsilon_0 \sum_{jk} \sum_{(nm)} \chi_{ijk}^{(2)}(\omega_n + \omega_m; \omega_n, \omega_m) E_j(\omega_n) E_k(\omega_m), \quad (1.15)$$

where the indices ijk refer to the Cartesian components of the fields, and (nm) notes that n and m can be varied while the sum $\omega_n + \omega_m$ remains fixed.

We can study the generalized case when we have two incoming fields with frequencies ω_1 and ω_2 . We can represent this in the following form

$$E(t) = E_1 e^{-i\omega_1 t} + E_2 e^{-i\omega_2 t} + \text{c.c.} \quad (1.16)$$

Assuming the form of equation (1.9)

$$P^{(2)} = \epsilon_0 \chi^{(2)} E(t)^2, \quad (1.17)$$

and substituting expression (1.16) we get

$$\begin{aligned} P^{(2)}(t) = \epsilon_0 \chi^{(2)} [& E_1^2 e^{-i2\omega_1 t} + E_2^2 e^{-i2\omega_2 t} \\ & + 2E_1 E_2 e^{-i(\omega_1 + \omega_2)t} + 2E_1 E_2^* e^{-i(\omega_1 - \omega_2)t} + \text{c.c.}] \\ & + 2\epsilon_0 \chi^{(2)} [E_1 E_1^* + E_2 E_2^*]. \end{aligned} \quad (1.18)$$

We separate this expression into its components and the nonlinear effect that each represents in the following manner (abbreviations defined in table 1.1),

$$\begin{aligned} P(2\omega_1) &= \epsilon_0 \chi^{(2)} E_1^2 e^{-i2\omega_1 t} + \text{c.c.} \quad (\text{SHG}), \\ P(2\omega_2) &= \epsilon_0 \chi^{(2)} E_2^2 e^{-i2\omega_2 t} + \text{c.c.} \quad (\text{SHG}), \\ P(\omega_1 + \omega_2) &= 2\epsilon_0 \chi^{(2)} E_1 E_2 e^{-i(\omega_1 + \omega_2)t} + \text{c.c.} \quad (\text{SFG}), \\ P(\omega_1 - \omega_2) &= 2\epsilon_0 \chi^{(2)} E_1 E_2^* e^{-i(\omega_1 - \omega_2)t} + \text{c.c.} \quad (\text{DFG}), \\ P(0) &= 2\epsilon_0 \chi^{(2)} (E_1 E_1^* + E_2 E_2^*) + \text{c.c.} \quad (\text{OR}). \end{aligned} \quad (1.19)$$

Janner [34] has a wonderfully formatted table in her dissertation that summarizes the first few optical processes, which I reproduce here as follows.

From this point forward we will only be concerned with second-order effects.

Symmetry Considerations for Centrosymmetric Materials

As mentioned previously, $\chi^{(2)}$ is a third-rank tensor with 27 elements. The amount of non-zero elements varies with the symmetry properties of the medium. Knowing these properties can help us reduce the amount of unknown elements to calculate.

I will mention only one that proves to be of extreme importance for surface optics. A centrosymmetric material, or a material with an inversion

$\chi^{(n)}(-\omega; \omega_1, \dots, \omega_n)$	Process	Order
$-\omega$; ω	Linear absorption / emission and refractive index	1
0 ; $\omega, -\omega$	Optical rectification (OR)	2
$-\omega$; $0, \omega$	Pockels effect	2
-2ω ; ω, ω	Second-harmonic generation (SHG)	2
$-(\omega_1 + \omega_2)$; ω_1, ω_2	Sum-frequency generation (SFG)	2
$-(\omega_1 - \omega_2)$; ω_1, ω_2	Difference-frequency generation (DFG) / Parametric amplification and oscillation	2
$-\omega$; $0, 0, \omega$	d.c. Kerr effect	3
-2ω ; $0, \omega, \omega$	Electric Field induced SHG (EFISH)	3
-3ω ; ω, ω, ω	Third-harmonic generation (THG)	3
$-\omega$; $\omega, -\omega, \omega$	Degenerate four-wave mixing (DFWM)	3
$-\omega$; $-\omega_2, \omega_2, \omega_1$	Two-photon absorption (TPA) / ionization / emission	3

Table 1.1: Optical processes described by $\chi^{(n)}(-\omega; \omega_1, \dots, \omega_n)$

center, is a material that for every point at coordinates (x, y, z) , there is an identical point located at $(-x, -y, -z)$. For instance, many crystals are centrosymmetric. If we assume that we are in the bulk of a centrosymmetric material, we can write the nonlinear polarization as

$$P(t) = \epsilon_0 \chi^{(2)} E^2(t). \quad (1.20)$$

If the medium is centrosymmetric, a sign change must affect both the electric field and the polarization. So,

$$-P(t) = \epsilon_0 \chi^{(2)} [-E(t)]^2, \quad (1.21)$$

$$= \epsilon_0 \chi^{(2)} E^2(t). \quad (1.22)$$

However, substituting (1.22) into (1.20) we get $P(t) = -P(t)$. We can finally deduce that

$$\chi^{(2)} = 0. \quad (1.23)$$

Therefore, all second-order processes are forbidden in the bulk of centrosymmetric materials in the dipole approximation. We will talk about the other important approximation in section 1.4.3. This property is broken at the surface since that region no longer presents an inversion center. This very special property is what enables second-order nonlinearities to be so effective for surface and interface measurements. Likewise, any other mechanism that breaks the symmetry, such as an electric field or mechanical stress

will also allow a second-order signal to be produced. See Bloembergen's [35] excellent review about second-order effects for surface spectroscopy for further reading.

1.4.3 Bulk Quadrupolar and Other Contributions

Everything that I have stated up to this point assumes what we call the *dipole approximation* that arises from assuming that the polarization can take the form of a multipole expansion. The dipole approximation simply assumes that the dipolar contribution is significantly greater than all the others. This is not necessarily the case in many materials. In particular, we find that there can be a non-negligible electric quadrupole contribution from the bulk of centrosymmetric materials. Bloembergen et al. [19] elaborate on this as early as the 1960s. This adds a severe complication to the use of second-order nonlinearities as surface probes since signal is actually produced from both surface and bulk. Sipe et al. [36] go into some detail about this problem, stating that it is very difficult to separate the surface and bulk contributions as the various nonlinear coefficients cannot be measured separately. Guyot-Sionnest and Shen [23] go one step further and state that the contributions are impossible to separate. They suggest that the best way to distinguish one from the other is by taking measurements before and after altering the surface and observing the overall changes to the produced signal. About a decade later, Shen et al. [37] state that bulk contributions not only come from the electric quadrupole, but also from the magnetic dipole, although the latter is typically much less intense than either of the former. They express the bulk polarization as a multipole series as follows,

$$\mathbf{P}^B(\omega) = \mathbf{P}_D(\omega) - \nabla \cdot \mathbf{Q}(\omega) - \left(\frac{c}{i\omega}\right) \nabla \times \mathbf{M}(\omega) + \dots, \quad (1.24)$$

where $\mathbf{P}_D(\omega)$ is the dipolar polarization, $\mathbf{Q}(\omega)$ is the electric quadrupole polarization, and $\mathbf{M}(\omega)$ is the magnetic dipole polarization. Indeed, if only the dipolar contribution is forbidden for centrosymmetric materials then there will be a contribution from the other two in addition to the dipolar contribution at the surface. The group does however go on to explain that there are a few experimental ways to help distinguish between surface and bulk contributions.

If $\mathbf{Q}(\omega)$ is assumed to take some form similar to

$$\mathbf{Q}(\omega) \approx \chi_q^{(2)}(\omega_1 + \omega_2) \mathbf{E}(\omega_1) \nabla \mathbf{E}(\omega_2), \quad (1.25)$$

then $\chi_q^{(2)}$ is a fourth-rank tensor with 81 independent elements. Clearly this adds some considerable complication to our problem and makes selecting the appropriate symmetry that much more important.

In summary, bulk electric quadrupole and magnetic dipole contributions to second-order surface effects may not be negligible and need to be taken into account. We will see later in sections 1.5 and 1.6 that these considerations are important for studying nanoparticles when using the XP2SHG/SFG technique.

1.4.4 SFG and SHG

We call the third process in expression (1.19) Sum-frequency generation (SFG). It is a second-order process that involves two photons, of frequencies ω_1 and ω_2 that combine to form one photon of frequency $\omega_3 = \omega_1 + \omega_2$. This is represented mathematically in the previous expression

$$P(\omega_1 + \omega_2) = 2\epsilon_0\chi^{(2)}E_1E_2e^{-i(\omega_1+\omega_2)t} + \text{c.c.}, \quad (1.26)$$

where the term is explicitly stated in the exponential.

A special case of sum-frequency generation is when both incoming frequencies are the same, i.e. $\omega_1 = \omega_2$. The resulting frequency is then exactly double that of the input frequency.

As mentioned previously, second-order nonlinear processes are prohibited in the bulk of centrosymmetric materials (in the dipole approximation). Since it has a very strong surface contribution (where the inversion symmetry is broken), it can be used as a very precise diagnostic tool for surface and interface regions.

The use of these second-order nonlinearities for surface studies had gained momentum in the 1990s. McGilp wrote a review about using SHG and SFG as surface and interface probes in 1996 [38]. He adds experimental confirmation to his theories in 1999 [39] in an extremely thorough review about using SHG on the surface of almost any material you can think of. Aktsipetrov et al. [40] followed a different approach by establishing what they call electric field induced second-harmonic generation, or EFISH. In this paper he elaborates how the sensitivity of SHG to surfaces can be enhanced by applying an electric field across the interface.

The theoretical side of things was further developed in a paper by Maytorena et al. [29] discussing the formalities of SFG from surfaces by finding the exact expressions for the susceptibility based on modeling conductors and dielectrics. These models include fluid based, classical dynamics in addition to the wave equation treatment. A couple of interesting review papers

by Downer et al. [30] and Scheidt et al. [41] exist, where they report results of SHG spectroscopies from a variety of different surfaces and interfaces including nanocrystals. These works are all predecessors for the later works we will discuss in section 1.5.

Phase-Matching

What happens when the generated nonlinear wave propagates through a medium is that it becomes out of phase with the induced polarization after some distance. When this happens, the induced polarization will create new light out of phase with the light it created earlier and the two contributions will cancel out. This can be avoided if both frequencies of light (the fundamental and the produced second-order field) travel at the same phase velocity through the medium. Each wave with a different frequency will have a different wave-vector (\mathbf{k}) and wavenumber (k). Optimally, we would like a material such that

$$\Delta k = k_1 + k_2 - k_3 = 0, \quad (1.27)$$

where $k_1 = k_2$ for SHG. Equation (1.27) exemplifies a *phase-matched* process. In practice, dispersion does not let this happen since the index of refraction of a material is almost never the same for different frequencies. There are certain materials that overcome this limitation (such as birefringent materials) that possess two indices of refraction.

Introducing equation (1.27) into the wave equation and solving, we can obtain the intensity profile [10] as

$$I(L) = \beta |P|^2 L^2 \text{sinc}^2 \left(\frac{\Delta k L}{2} \right), \quad (1.28)$$

where L is the length of the material, Δk is the phase mismatch, and β are constants. The sinc function has a maximum at zero, so it is important to reduce the phase mismatch as much as possible. The inclusion of L also indicates a relation to the material thickness. These considerations are important when selecting a nonlinear material such as a crystal – most are sold in varying thicknesses that are optimized to work with certain frequencies.

In practice, phase-matching is usually improved through crystal orientation, selecting the right crystal thickness, and careful selection of the type of crystal being used.

1.4.5 Optical Parametric Amplifiers

We talked about how we can obtain different frequencies of light through wave mixing in section 1.4.4. In practice however, it is considerably more difficult to implement a system in which we can easily create frequency addition or difference. It is no small task even with a fixed input wavelength. Most ultrafast lasers are tunable to some degree by adjusting internal components. We'll need something much more sophisticated if we want a variety of frequency choices.

An optical parametric amplifier (OPA) is a device that allows the user to obtain a wide bandwidth of wavelengths to work with, via the nonlinear processes of difference frequency generation (DFG) and optical parametric generation (OPG). Additionally, many commercial OPAs allow the user to tune the output by means of a motorized, computer-controlled interface. Some OPAs work on the basis of sum and difference frequency generation, using crystals to add and subtract the different frequencies in order to obtain the desired one.

OPG is a by-product of DFG. DFG occurs when a high frequency (ω_1) photon is absorbed by an atom that jumps to a virtual level after being excited. It then decays producing two photons of lower frequency (ω_2 and ω_3). The creation of the ω_2 photon is what we call OPG. If we instigate this process in the presence of an ω_2 field, the same frequency (ω_2) gets amplified at expense of the original ω_1 photon. The ω_3 frequency is called the idler and can be used in the same way as ω_2 if desired. This effect is called optical parametric amplification. Therefore, we can create an OPA by creating a new frequency via OPG, and amplifying it using a crystal or other nonlinear media through optical parametric amplification.

In practice most OPAs work like this: a high frequency, high power pump beam amplifies a lower frequency, lower power signal beam in a nonlinear crystal which is our desired ω_2 . This pump beam is usually the laser fundamental. This fixed pump beam transfers energy to produce the signal beam that is selectable via phase matching. This signal beam then feeds a second crystal to produce optical parametric amplification. We might be inclined to think that this is a form of stimulated emission similar to what happens in a laser (sans cavity). In stimulated emission, an electron drops from a higher level to a lower level due to the outside perturbing influence of an incident photon. It radiates with the exact same characteristics as the incoming field. OPA involves a transfer of energy from one photon to another (in our example, ω_2 and ω_1) to amplify ω_2 while annihilating ω_1 .

1.4.6 Noncollinear Optical Parametric Amplifiers

A noncollinear optical parametric amplifier (NOPA) replaces the ω_2 signal with a white light super continuum. Tuning a NOPA is achieved by changing the angle between the seed and the pump beam, by changing the orientation of the crystal, or by using a delay stage to temporally overlap the fundamental with the desired frequency from the continuum.

In practice, the white light seed is typically generated from a sapphire window. The pump is normally the frequency doubled fundamental at 400 nm [42, 43]. The NOPA has a larger bandwidth than a regular OPA, and the resulting pulsewidth is dependent only on the bandwidth of the seed and not on the pulsewidth of the laser. For this reason, the NOPA has improved stability and spatial qualities. The added flexibility of the NOPA allows for different geometries to be implemented [44]. Gale [45] and Wilhelm et al. [46] wrote some of the earliest papers referring to this type of OPA. Lee [47] explains some of the formalism behind the operation of a NOPA.

1.5 Second-Order Nonlinear Response of Nanoparticles

The theory up to this point explains how second-order nonlinearities interact with matter and how they have been used for studying planar surfaces. I mentioned in chapter ?? how nanoparticles have very large surface to volume ratios. The study of nanosystems with conventional optics has further motivated scientists to begin using second-order nonlinear phenomena to obtain more information from their samples.

I will briefly review some of the current models for describing the optical response for nanoparticles. These models consist of parametrizing the nonlinear response and then calculating the second-order emissions from the idealized nanosystem.

Dadap et al. [48] developed some early work in 1999, and later expanded on that in 2004 [49]. They modeled SHG for a centrosymmetric nanosphere and concluded that SHG is produced via nonlocal excitation of the electric dipole moment and local excitation of the electric quadrupole moment. In other words, the electric-dipole can have excitation from either the electric quadrupole or the magnetic dipole, in addition to excitation provided by the incoming field. These results were verified experimentally by Shan et al. [50] in an article from 2006, by taking angle- and polarization-resolved measurements of dye-coated polystyrene spheres. Brudny et al. [51] created

a similar model that focuses on analytical expressions for the dipolar and quadrupolar second-order susceptibilities for a small dielectric sphere, and the nonlinear response for a Si sphere above a substrate.

A more relevant treatment was published by Mochán et al. for an array of nanoparticles [52] that builds on their previous article [51]. This approach assumes spherical nanoparticles and should work well with the samples described in this work (see figures ?? and ??). I'll briefly review the method as follows.

1.5.1 Theoretical Model

Let us assume a nanosphere centered at the origin. It has a linear response characterized in the usual way by its dielectric function $\epsilon(\omega)$. We assume the applied field, $\mathbf{E}^{\text{ex}}(\mathbf{r})$ is inhomogeneous and varies on a much larger scale than R , the radius of the nanoparticle. The dipole moment $\mathbf{p}^{(2)}$ is in some way related to $\mathbf{E}^{\text{ex}}(0)$ and $\nabla \mathbf{E}^{\text{ex}}(0)$, and is nonlocal as dictated by the symmetry of the sphere. We can express this relation as

$$\mathbf{p}^{(2)} = \gamma^\rho \mathbf{E}^{\text{ex}}(0) \nabla \cdot \mathbf{E}^{\text{ex}}(0) + \gamma^e \mathbf{E}^{\text{ex}}(0) \cdot \nabla \mathbf{E}^{\text{ex}}(0) + \gamma^m \mathbf{E}^{\text{ex}}(0) \times [\nabla \times \mathbf{E}^{\text{ex}}(0)], \quad (1.29)$$

where γ^ρ , γ^e , and γ^m are nonlinear response parameters. It is clearly nonlocal as it contains the field derivative. Likewise, [51] shows that the quadrupole moment, $\mathbf{Q}^{(2)}$, should be local, and symmetric of the form

$$\mathbf{Q}^{(2)} = \gamma^q \left(\mathbf{E}^{\text{ex}}(0) \mathbf{E}^{\text{ex}}(0) - \frac{1}{3} [\mathbf{E}^{\text{ex}}(0)]^2 \mathbf{1} \right), \quad (1.30)$$

where γ^q is the parametric response parameter. Note that it is local and does not depend on the field derivative. As there is no external charge inside the sphere, $\gamma^\rho = 0$. A lengthy derivation is necessary to obtain the remaining response parameters and I will not include it here. From those parameters we obtain the values of $\mathbf{p}^{(2)}$ and $\mathbf{Q}^{(2)}$, with

$$Q^{(2)} = \gamma^q [\mathbf{E}^{\text{ex}}(0)]^2. \quad (1.31)$$

Substituting these into the expression for the macroscopic nonlinear polarization for the entire array of spheres

$$\mathbf{P}^{nl} = n_s \mathbf{p}^{(2)} - \frac{1}{6} \nabla \cdot n_s \mathbf{Q}^{(2)} - \frac{1}{6} \nabla n_s Q^{(2)}, \quad (1.32)$$

where n_s is the nanocrystal volume density; we can then obtain

$$\mathbf{P}^{nl} = \Gamma \nabla E^2 + \Delta' (\mathbf{E} \cdot \nabla \mathbf{E}). \quad (1.33)$$

The first term can be neglected because it is longitudinal and does not radiate. With $\Delta' \equiv n_s (\gamma^e - \gamma^m - \gamma^q/6)$, we can finally write the expression for the polarization as

$$\mathbf{P}^{(2)} = \Delta' (\mathbf{E} \cdot \nabla \mathbf{E}), \quad (1.34)$$

where \mathbf{E} represents the incoming laser field. The relevance of this expression will become apparent in section 1.6, when we discuss the XP2SHG/SFG technique.

1.5.2 Other Works

Two relatively recent articles have studied different nonlinear effects on a variety of nanoscale gold shapes (primarily split-ring resonators) [53, 54]. The group hypothesizes that the samples show improved SHG due to local and nonlocal fields; in this case, magnetic resonances.

Zeng et al. [55] developed a model based on classical electrodynamics to predict SHG in metallic nanostructures. Solving Maxwell's equations yields an expression for the SHG signal intensity and is surprisingly close to experimental values. However, the derivation is considerably easier due to the approximations.

For further reading, Link and El-Sayed [56] offer a very extensive review of many other optical properties of nanoparticles.

1.5.3 Summary

In this section we saw how the theory indicates that the second-order response of nanoparticles depends both on the strength of the incoming field, but also on its characteristics. We also introduced the dependence on $(\mathbf{E} \cdot \nabla) \mathbf{E}$ of the nonlinear second-order polarization. With this information in hand we can determine the best technique to optimize our nonlinear signal.

Formally, we learned that the second-order nonlinearities are produced in nanoparticles thanks to local interface electric dipole contributions, plus quadrupolar contributions from the interior of the nanoparticles.

1.6 Theory for the XP2SHG/SFG Technique

In 2003, Cattaneo and Kauranen [57] published about a promising new technique involving two beams coinciding on a thin film. They proposed that the use of the second beam reduces the number of nonlinear coefficients to

be determined if the polarization of the two beams is properly described beforehand. The method was simple enough – they expressed the parallel and perpendicular fields separately as a sum of expansion coefficients that are in themselves linear combinations of susceptibility components. Changing the polarization of the control and probe beam would determine different coefficients. Adding the linear optical properties of the film and modeling with Green’s-function led to the desired $\chi^{(2)}$ coefficients.

Following in 2005, Figliozzi et al. [9] note the importance of the aforementioned $(\mathbf{E} \cdot \nabla \mathbf{E})$ term and relate it to the enhanced quadrupolar contribution; they go on to experimentally verify that dependence. They also discover that the two beam arrangement greatly enhances the entire SHG signal, both from the microscopic contributions of the particles as well as the bulk quadrupolar contribution from the substrate. This brings up the issue of how to discriminate between the two contributions to the SHG signal, which they manage to do by contrasting the difference in signal at different polarizations between the particles and the unimplanted glass.

In 2009 Wang et al. with some of the same people from references [53] and [54] elaborate a study on a gold thin film using a two-beam configuration [58]. They follow a similar model to that described in [9], but their goal is separating the surface and bulk components of the SH field. This is done by finding material parameters due to the magnetic dipole and electric quadrupole by varying the polarization of the incoming beams. They succeed in finding which components of $\chi^{(2)}$ belong to surface only, bulk only, or both.

A very recent and thorough article [43] by Wei et al. presents experimental evidence that supports the use of two-beam SHG with nanoparticles. They go into detail about the linear characterization of the Si nanocrystals used, which includes photoluminescence spectra, spectroscopic ellipsometry, and Raman microspectroscopy. By moving the sample across the overlapping beam region (the Z-scan technique) they were able to effectively determine which signal was produced by nanoparticles and which by bulk contributions from the substrate. They conclude with a very complete characterization of the Si nanocrystals after comparing the obtained data with that of the other conventional spectroscopies. Coincidentally, the setup described in this article is the exact one used in the experimental portion of this work, and is detailed in chapter ??.

A 2008 article [59] by Wirth et al. provides excellent review of the exact technique used in this work. It is also noteworthy in that it is the first article to refer to this technique as XP2SHG. Following on the work that we discussed in section 1.5.1, they establish that the polarization of the samples

can be separated into two expressions,

$$\mathbf{P}_{nc}^{(2)} \equiv n_b \left(\gamma^e - \gamma^m - \frac{\gamma^q}{6} \right) (\mathbf{E} \cdot \nabla) \mathbf{E}, \quad (1.35)$$

$$\mathbf{P}_g^{(2)} \equiv (\delta - \beta - 2\gamma) (\mathbf{E} \cdot \nabla) \mathbf{E}, \quad (1.36)$$

where equation (1.35) is identical to (1.34). The article confirms that the XP2SHG technique enhances both the nanocrystal and glass signals, and goes on to say that the detected SHG signal is a product of the interference of both. This would account for shape of the plotted data from the results of the Z-scan presented in [59], in [43], and in chapter ?? of this thesis.

The fields can be described by the amplitudes of the SH field from the nanocrystals $|\Gamma_{nc}|$, the glass Γ_g , and the phase Φ between them such that

$$\mathbf{P}_{nc}^{(2)} \equiv |\Gamma_{nc}| e^{i\Phi} (\mathbf{E} \cdot \nabla) \mathbf{E}, \quad (1.37)$$

$$\mathbf{P}_g^{(2)} \equiv \Gamma_g (\mathbf{E} \cdot \nabla) \mathbf{E}. \quad (1.38)$$

Three independent Z-scan measurements are needed to enable isolation of the nanocrystal signal and obtain the three unknowns $|\Gamma_{nc}|$, Γ_g , and Φ : a glass scan, a scan with the nanocrystals at the entrance position, and with the nanocrystals at the exit position. They establish an empirical model based on the wave equations for each measurement, thus determining the intensity profile expressions in terms of the unknowns. All that is left is running the scans and plugging in the data to determine them and fully isolate the different contributions.

Studies like those included in [43] and [59] are precisely in line with the work presented in this thesis.

1.6.1 Signal enhancement with XP2SHG/SFG

It was confirmed [9, 60] by Sun and Figliozzi et al. that the dipolar SHG single beam count rate scales as

$$N_{SHG} \sim f_{\text{rep}} I^2 A \tau = \frac{f_{\text{rep}} \mathcal{E}^2}{\tau A}, \quad (1.39)$$

where A is the beam spot size ($A = \pi w_0^2$), τ is the pulse duration, \mathcal{E} is the pulse energy, and f_{rep} is the repetition rate of the pulses. In correlation with the $(\mathbf{E} \cdot \nabla) \mathbf{E}$ dependence, that same group determined that the derivative

creates an additional term for a Gaussian beam. This term comes from the quadrupolar contribution and introduces an extra factor of A , such that

$$N_{SHG} \sim \frac{f_{\text{rep}} \mathcal{E}^2}{\tau A^2}. \quad (1.40)$$

If we use two incoming plane wave fields, we obtain from (1.35) (ignoring constants)

$$\mathbf{P}_{nc}^{(2)} \approx [(\mathbf{E}_1 \cdot \nabla) \mathbf{E}_2 + (\mathbf{E}_2 \cdot \nabla) \mathbf{E}_1] e^{i(\mathbf{k}_1 + \mathbf{k}_2) \cdot \mathbf{r}}. \quad (1.41)$$

We define the incoming fields as

$$\mathbf{E}_i(\mathbf{r}) = \hat{\epsilon}_i \mathcal{E} e^{i\mathbf{k}_i \cdot \mathbf{r}}, \quad (1.42)$$

where $\hat{\epsilon}_i$ is the polarization. For *cross-polarized* beams, $\hat{\epsilon}_1 \perp \hat{\epsilon}_2$; if $\hat{\epsilon}_1 = \hat{y}$, then

$$\mathbf{P}_{nc}^{(2)} \approx \frac{1}{\lambda} \mathcal{E}_1 \mathcal{E}_2 \sin \alpha \hat{y}, \quad (1.43)$$

where $\frac{1}{\lambda} = k$. Now the signal intensity scales as

$$N_{SHG} \sim \frac{f_{\text{rep}} \mathcal{E}_1 \mathcal{E}_2 \sin^2 \alpha}{\lambda^2 \tau A^2}, \quad (1.44)$$

where α is the angle between the beams. The $\frac{1}{\lambda}^2$ factor increases the intensity of the signal very significantly, while the $\sin^2 \alpha$ term allows us to optimize the beam angle.

1.6.2 Summary

We used this section to discuss the fine points behind the XP2SHG/SFG technique. It offers three benefits over single beam second-order spectroscopy:

1. The SHG/SFG signal intensities are much higher than for single beam SHG/SFG.
2. The enhanced SHG/SFG signal allows for more elements of the nonlinear susceptibility $\chi^{(2)}$, and therefore of the second order polarization to be determined.
3. Dipole contribution from the surface can be discriminated from electric quadrupole and magnetic dipole contributions from bulk for planar materials.

4. Hybrid (dipole and quadrupole) contribution from the nanoparticles can be discriminated from electric quadrupole and magnetic dipole contributions from the substrate bulk.

1.7 some old shit

Second harmonic generation (SHG) is a powerful spectroscopic tool for studying the optical properties of surfaces and interfaces since it has the advantage of being surface sensitive. Within the dipole approximation, inversion symmetry forbids SHG from the bulk of centrosymmetric materials. SHG is allowed at the surface of these materials where the inversion symmetry is broken and should necessarily come from the localized surface region. SHG allows the study of the structural atomic arrangement and phase transitions of clean and adsorbate covered surfaces. Since it is also an optical probe it can be used out of UHV conditions and is non-invasive and non-destructive. Experimentally, new tunable high intensity laser systems have made SHG spectroscopy readily accessible and applicable to a wide range of systems.[61, 62]

However, theoretical development of the field is still an ongoing subject of research. Some recent advances for the cases of semiconducting and metallic systems have appeared in the literature, where the use of theoretical models with experimental results have yielded correct physical interpretations for observed SHG spectra. [61, 63, 64, 65, 66, 67, 68, 69, 70]

In a previous article[71] we reviewed some of the recent results in the study of SHG using the velocity gauge for the coupling between the electromagnetic field and the electron. In particular, we demonstrated a method to systematically analyze the different contributions to the observed SHG peaks.[72] This approach consists of separating the different contributions to the nonlinear susceptibility according to 1ω and 2ω transitions, and the surface or bulk nature of the states among which the transitions take place.

To compliment those results, in this article we review the calculation of the nonlinear susceptibility using the longitudinal gauge. We show that it is possible to clearly obtain the “layer-by-layer” contribution for a slab scheme used for surface calculations.

CHAPTER 2

CHI2

2.1 Non-linear Surface Susceptibility

In this section we outline the general procedure to obtain the surface susceptibility tensor for second harmonic generation. We start with the non-linear polarization \mathbf{P} written as

$$P_a(2\omega) = \chi_{abc}(-2\omega; \omega, \omega) E_b(\omega) E_c(\omega) + \chi_{abcl}(-2\omega; \omega, \omega) E_b(\omega) \nabla_c E_l(\omega) + \dots, \quad (2.1)$$

where $\chi_{abc}(-2\omega; \omega, \omega)$ and $\chi_{abcl}(-2\omega; \omega, \omega)$ correspond to the dipolar and quadrupolar susceptibilities. We drop the $(-2\omega; \omega, \omega)$ argument to ease on the notation. The sum continues with higher multipolar terms. If we consider a semi-infinite system with a centrosymmetric bulk, the equation above can be separated into two contributions from symmetry considerations alone; one from the surface of the system and the other from the bulk of the system. We take

$$P_a(\mathbf{r}) = \chi_{abc} E_b(\mathbf{r}) E_c(\mathbf{r}) + \chi_{abcl} E_b(\mathbf{r}) \frac{\partial}{\partial \mathbf{r}_c} E_l(\mathbf{r}) + \dots, \quad (2.2)$$

as the polarization with respect to the original coordinate system, and

$$P_a(-\mathbf{r}) = \chi_{abc} E_b(-\mathbf{r}) E_c(-\mathbf{r}) + \chi_{abcl} E_b(-\mathbf{r}) \frac{\partial}{\partial (-\mathbf{r}_c)} E_l(-\mathbf{r}) + \dots, \quad (2.3)$$

as the polarization in the coordinate system where inversion is taken, i.e. $\mathbf{r} \rightarrow -\mathbf{r}$. Note that we have kept the same susceptibility tensors, and they must be invariant under $\mathbf{r} \rightarrow -\mathbf{r}$ since the system is centrosymmetric. Recalling that $\mathbf{P}(\mathbf{r})$ and $\mathbf{E}(\mathbf{r})$ are polar vectors [?], we have that Eq. (2.3) reduces to

$$\begin{aligned} -P_a(\mathbf{r}) &= \chi_{abc}(-E_b(\mathbf{r}))(-E_c(\mathbf{r})) - \chi_{abcl}(-E_b(\mathbf{r}))\left(-\frac{\partial}{\partial \mathbf{r}_c}\right)(-E_l(\mathbf{r})) + \dots, \\ P_a(\mathbf{r}) &= -\chi_{abc} E_b(\mathbf{r}) E_c(\mathbf{r}) + \chi_{abcl} E_b(\mathbf{r}) \frac{\partial}{\partial \mathbf{r}_c} E_l(\mathbf{r}) + \dots, \end{aligned} \quad (2.4)$$

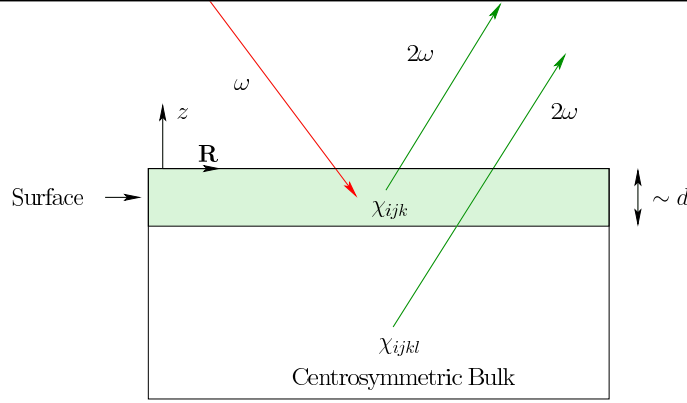


Figure 2.1: (Color Online) Sketch of the semi-infinite system with a centrosymmetric bulk. The surface region is of width $\sim d$. The incoming photon of frequency ω is represented by a downward red arrow, whereas both the surface and bulk created second harmonic photons of frequency 2ω are represented by upward green arrows. The red color suggests an incoming infrared photon with a green second harmonic photon. The dipolar (χ_{abc}), and quadrupolar (χ_{abcl}) susceptibility tensors are shown in the regions where they are different from zero. The axis has z perpendicular to the surface and \mathbf{R} parallel to it.

that when compared with Eq. (2.2) leads to the conclusion that

$$\chi_{abc} = 0 \quad (2.5)$$

for a centrosymmetric bulk.

If we move to the surface of the semi-infinite system our assumption of centrosymmetry breaks down, and there is no restriction in χ_{abc} . We conclude that the leading term of the polarization in a surface region is given by

$$\int dz P_a(\mathbf{R}, z) \approx dP_a \equiv P_a^S \equiv \chi_{abc}^S E_b E_c, \quad (2.6)$$

where d is the surface region from which the dipolar signal of \mathbf{P} is different from zero (see Fig. 2.1), and $\mathbf{P}^S \equiv d\mathbf{P}$ is the surface SH polarization. Then, from Eq. (2.1) we obtain that

$$\chi_{abc}^S = d\chi_{abc} \quad (2.7)$$

is the SH surface susceptibility. On the other hand,

$$P_a^b(\mathbf{r}) = \chi_{abcl} E_b(\mathbf{r}) \nabla_c E_l(\mathbf{r}), \quad (2.8)$$

gives the bulk polarization. We immediately recognize that the surface polarization is of dipolar order while the bulk polarization is of quadrupolar order. The surface, χ_{abc}^S , and bulk, χ_{abcl} , susceptibility tensor ranks are three and four, respectively. We will only concentrate on surface SHG in this article even though bulk generated SH is also a very important optical phenomenon. Also, we leave out of this article other interesting surface SH phenomena like, electric field induced second harmonic (EFISH), which would be represented by a surface susceptibility tensor of quadrupolar origin. In centrosymmetric systems for which the quadrupolar bulk response is much smaller than the dipolar surface response, SH is readily used as a very useful and powerful optical surface probe.[61]

In the following sections we present the theoretical approach to derive the expressions for the surface susceptibility tensor χ_{abc}^S .

2.2 Length Gauge

We follow the article by Aversa and Sipe[73] to calculate the optical properties of a given system within the longitudinal gauge. More recent derivations can also be found in Refs. [74, 75]. Assuming the long-wavelength approximation which implies a position independent electric field, $\mathbf{E}(t)$, the Hamiltonian in the length gauge approximation is given by

$$\hat{H} = \hat{H}_0^\sigma - e\hat{\mathbf{r}} \cdot \mathbf{E}, \quad (2.9)$$

with

$$\hat{H}_0^\sigma = \hat{H}_0^{\text{LDA}} + \mathcal{S}(\mathbf{r}, \mathbf{p}), \quad (2.10)$$

as the unperturbed Hamiltonian. The LDA Hamiltonian can be expressed as follows,

$$\begin{aligned} \hat{H}_0^{\text{LDA}} &= \frac{\hat{p}^2}{2m_e} + \hat{V}^{\text{ps}} \\ \hat{V}^{\text{ps}} &= \hat{V}^l(\hat{\mathbf{r}}) + \hat{V}^{\text{nl}}, \end{aligned} \quad (2.11)$$

where $\hat{V}^l(\hat{\mathbf{r}})$ and \hat{V}^{nl} are the local and the non-local parts of the crystal pseudopotential \hat{V}^{ps} . For the latter, we have that

$$V^{\text{nl}}(\mathbf{r}, \mathbf{r}') \equiv \langle \mathbf{r} | \hat{V}^{\text{nl}} | \mathbf{r}' \rangle \neq 0 \quad \text{for} \quad \mathbf{r} \neq \mathbf{r}', \quad (2.12)$$

where $V^{\text{nl}}(\mathbf{r}, \mathbf{r}')$ is a function of \mathbf{r} and \mathbf{r}' representing the non-local contribution of the pseudopotential. The Schrödinger equation reads

$$\left(\frac{-\hbar^2}{2m_e}\nabla^2 + \hat{V}^l(\mathbf{r})\right)\psi_{n\mathbf{k}}(\mathbf{r}) + \int d\mathbf{r}' \hat{V}^{\text{nl}}(\mathbf{r}, \mathbf{r}')\psi_{n\mathbf{k}}(\mathbf{r}') = E_i\psi_{n\mathbf{k}}(\mathbf{r}), \quad (2.13)$$

where $\psi_{n\mathbf{k}}(\mathbf{r}) = \langle \mathbf{r} | n\mathbf{k} \rangle = e^{i\mathbf{k}\cdot\mathbf{r}} u_{n\mathbf{k}}(\mathbf{r})$, are the real space representations of the Bloch states $|n\mathbf{k}\rangle$ labelled by the band index n and the crystal momentum \mathbf{k} , and $u_{n\mathbf{k}}(\mathbf{r})$ is cell periodic. m_e is the bare mass of the electron and Ω is the unit cell volume. The nonlocal scissors operator is given by

$$\mathcal{S}(\mathbf{r}, \mathbf{p}) = \hbar\Sigma \sum_n \int d^3k' (1 - f_n(\mathbf{k})) |n\mathbf{k}'\rangle \langle n\mathbf{k}'|, \quad (2.14)$$

where $f_n(\mathbf{k})$ is the occupation number, that for $T = 0$ K, is independent of \mathbf{k} , and is one for filled bands and zero for unoccupied bands. For semiconductors the filled bands correspond to valence bands ($n = v$) and the unoccupied bands to conduction bands ($n = c$). We have that

$$\begin{aligned} H_0^{\text{LDA}} |n\mathbf{k}\rangle &= \hbar\omega_n^{\text{LDA}}(\mathbf{k}) |n\mathbf{k}\rangle \\ H_0^\sigma |n\mathbf{k}\rangle &= \hbar\omega_n^\sigma(\mathbf{k}) |n\mathbf{k}\rangle, \end{aligned} \quad (2.15)$$

where

$$\hbar\omega_n^\sigma(\mathbf{k}) = \hbar\omega_n^{\text{LDA}}(\mathbf{k}) + \hbar\Sigma(1 - f_n), \quad (2.16)$$

is the scissored energy. Here, $\hbar\Sigma$ is the value by which the conduction bands are rigidly (\mathbf{k} -independent) shifted upwards in energy, also known as the scissors shift. Σ could be taken to be \mathbf{k} dependent, but for most calculations (like the ones presented here), a rigid shift is sufficient. We can take $\hbar\Sigma = E_g - E_g^{\text{LDA}}$ where E_g could be the experimental band gap or GW band gap taken at the Γ point, i.e. $\mathbf{k} = 0$. We used the fact that $|n\mathbf{k}\rangle^{\text{LDA}} \approx |n\mathbf{k}\rangle^\sigma$, thus negating the need to label the Bloch states with the LDA or σ superscripts. The matrix elements of \mathbf{r} are split between the *intra*band (\mathbf{r}_i) and *inter*band (\mathbf{r}_e) parts, where $\mathbf{r} = \mathbf{r}_i + \mathbf{r}_e$ and [76, 77, 73]

$$\langle n\mathbf{k} | \hat{\mathbf{r}}_i | m\mathbf{k}' \rangle = \delta_{nm} [\delta(\mathbf{k} - \mathbf{k}') \boldsymbol{\xi}_{nn}(\mathbf{k}) + i\nabla_{\mathbf{k}} \delta(\mathbf{k} - \mathbf{k}')], \quad (2.17)$$

$$\langle n\mathbf{k} | \hat{\mathbf{r}}_e | m\mathbf{k}' \rangle = (1 - \delta_{nm}) \delta(\mathbf{k} - \mathbf{k}') \boldsymbol{\xi}_{nm}(\mathbf{k}), \quad (2.18)$$

and

$$\boldsymbol{\xi}_{nm}(\mathbf{k}) \equiv i \frac{(2\pi)^3}{\Omega} \int_{\Omega} d\mathbf{r} u_{n\mathbf{k}}^*(\mathbf{r}) \nabla_{\mathbf{k}} u_{m\mathbf{k}}(\mathbf{r}). \quad (2.19)$$

The interband part \mathbf{r}_e can be obtained as follows. We start by introducing the velocity operator

$$\hat{\mathbf{v}}^\sigma = \frac{1}{i\hbar} [\hat{\mathbf{r}}, \hat{H}_0^\sigma], \quad (2.20)$$

and calculating its matrix elements

$$i\hbar \langle n\mathbf{k} | \hat{\mathbf{v}}^\sigma | m\mathbf{k} \rangle = \langle n\mathbf{k} | [\hat{\mathbf{r}}, \hat{H}_0^\sigma] | m\mathbf{k} \rangle = \langle n\mathbf{k} | \hat{\mathbf{r}} \hat{H}_0^\sigma - \hat{H}_0^\sigma \hat{\mathbf{r}} | m\mathbf{k} \rangle = (\hbar\omega_m^\sigma(\mathbf{k}) - \hbar\omega_n^\sigma(\mathbf{k})) \langle n\mathbf{k} | \hat{\mathbf{r}} | m\mathbf{k} \rangle, \quad (2.21)$$

thus defining $\omega_{nm}^\sigma(\mathbf{k}) = \omega_n^\sigma(\mathbf{k}) - \omega_m^\sigma(\mathbf{k})$ we get

$$\mathbf{r}_{nm}(\mathbf{k}) = \frac{\mathbf{v}_{nm}^\sigma(\mathbf{k})}{i\omega_{nm}^\sigma(\mathbf{k})} \quad n \notin D_m, \quad (2.22)$$

which can be identified as $\mathbf{r}_{nm} = (1 - \delta_{nm})\boldsymbol{\xi}_{nm} \rightarrow \mathbf{r}_{e,nm}$. Here, D_m are all the possible degenerate m -states. When \mathbf{r}_i appears in commutators we use [73]

$$\langle n\mathbf{k} | [\hat{\mathbf{r}}_i, \hat{\mathcal{O}}] | m\mathbf{k}' \rangle = i\delta(\mathbf{k} - \mathbf{k}') (\mathcal{O}_{nm})_{;\mathbf{k}}, \quad (2.23)$$

with

$$(\mathcal{O}_{nm})_{;\mathbf{k}} = \nabla_{\mathbf{k}} \mathcal{O}_{nm}(\mathbf{k}) - i\mathcal{O}_{nm}(\mathbf{k}) (\boldsymbol{\xi}_{nn}(\mathbf{k}) - \boldsymbol{\xi}_{mm}(\mathbf{k})), \quad (2.24)$$

where “ $;\mathbf{k}$ ” denotes the generalized derivative (see Appendix ??).

As can be seen from Eq. (2.10) and (2.11), both \hat{S} and \hat{V}^{nl} are nonlocal potentials. Their contribution in the calculation of the optical response has to be taken in order to get reliable results.[78] We proceed as follows; from Eqs. (2.20), (2.10) and (2.11) we find

$$\begin{aligned} \hat{\mathbf{v}}^\sigma &= \frac{\hat{\mathbf{p}}}{m_e} + \frac{1}{i\hbar} [\hat{\mathbf{r}}, \hat{V}^{\text{nl}}(\mathbf{r}, \mathbf{r}')] + \frac{1}{i\hbar} [\hat{\mathbf{r}}, \hat{S}(\mathbf{r}, \mathbf{p})] \\ &\equiv \hat{\mathbf{v}} + \hat{\mathbf{v}}^{\text{nl}} + \hat{\mathbf{v}}^{\text{S}} = \hat{\mathbf{v}}^{\text{LDA}} + \hat{\mathbf{v}}^{\text{S}}, \end{aligned} \quad (2.25)$$

where we have defined

$$\begin{aligned} \hat{\mathbf{v}} &= \frac{\hat{\mathbf{p}}}{m_e} \\ \hat{\mathbf{v}}^{\text{nl}} &= \frac{1}{i\hbar} [\hat{\mathbf{r}}, \hat{V}^{\text{nl}}] \\ \hat{\mathbf{v}}^{\text{S}} &= \frac{1}{i\hbar} [\hat{\mathbf{r}}, \hat{S}(\mathbf{r}, \mathbf{p})] \\ \hat{\mathbf{v}}^{\text{LDA}} &= \hat{\mathbf{v}} + \hat{\mathbf{v}}^{\text{nl}} \end{aligned} \quad (2.26)$$

with $\hat{\mathbf{p}} = -i\hbar\nabla$ the momentum operator. Using Eq. (2.14), we obtain that the matrix elements of $\hat{\mathbf{v}}^S$ are given by

$$\mathbf{v}_{nm}^S = i\Sigma f_{mn}\mathbf{r}_{nm}, \quad (2.27)$$

with $f_{nm} = f_n - f_m$, where we see that $\mathbf{v}_{nn}^S = 0$, then

$$\begin{aligned} \mathbf{v}_{nm}^\sigma &= \mathbf{v}_{nm}^{\text{LDA}} + i\Sigma f_{mn}\mathbf{r}_{nm} \\ &= \mathbf{v}_{nm}^{\text{LDA}} + i\Sigma f_{mn} \frac{\mathbf{v}_{nm}^\sigma(\mathbf{k})}{i\omega_{nm}^\sigma(\mathbf{k})} \\ \mathbf{v}_{nm}^\sigma \frac{\omega_{nm}^\sigma - \Sigma f_{mn}}{\omega_{nm}^\sigma} &= \mathbf{v}_{nm}^{\text{LDA}} \\ \mathbf{v}_{nm}^\sigma \frac{\omega_{nm}^{\text{LDA}}}{\omega_{nm}^\sigma} &= \mathbf{v}_{nm}^{\text{LDA}} \\ \frac{\mathbf{v}_{nm}^\sigma}{\omega_{nm}^\sigma} &= \frac{\mathbf{v}_{nm}^{\text{LDA}}}{\omega_{nm}^{\text{LDA}}}, \end{aligned} \quad (2.28)$$

since $\omega_{nm}^\sigma - \Sigma f_{mn} = \omega_{nm}^{\text{LDA}}$. Therefore,

$$\begin{aligned} \mathbf{v}_{nm}^\sigma(\mathbf{k}) &= \frac{\omega_{nm}^\sigma}{\omega_{nm}^{\text{LDA}}} \mathbf{v}_{nm}^{\text{LDA}}(\mathbf{k}) = \left(1 + \frac{\Sigma}{\omega_c(\mathbf{k}) - \omega_v(\mathbf{k})}\right) \mathbf{v}_{nm}^{\text{LDA}}(\mathbf{k}) \quad n \notin D_m \\ \mathbf{v}_{nn}^\sigma(\mathbf{k}) &= \mathbf{v}_{nn}^{\text{LDA}}(\mathbf{k}), \end{aligned} \quad (2.29)$$

and Eq. (2.22) gives

$$\mathbf{r}_{nm}(\mathbf{k}) = \frac{\mathbf{v}_{nm}^\sigma(\mathbf{k})}{i\omega_{nm}^\sigma(\mathbf{k})} = \frac{\mathbf{v}_{nm}^{\text{LDA}}(\mathbf{k})}{i\omega_{nm}^{\text{LDA}}(\mathbf{k})} \quad n \notin D_m. \quad (2.30)$$

The matrix elements of \mathbf{r}_e are the same whether we use the LDA or the scissored Hamiltonian and there is no need to label them with either LDA or S superscripts. Thus, we can write

$$\mathbf{r}_{e,nm} \rightarrow \mathbf{r}_{nm}(\mathbf{k}) = \frac{\mathbf{v}_{nm}^{\text{LDA}}(\mathbf{k})}{i\omega_{nm}^{\text{LDA}}(\mathbf{k})} \quad n \notin D_m, \quad (2.31)$$

which gives the interband matrix elements of the position operator in terms of the matrix elements of $\hat{\mathbf{v}}^{\text{LDA}}$. These matrix elements include the matrix elements of $\mathbf{v}_{nm}^{\text{nl}}(\mathbf{k})$ which can be readily calculated[?] for fully separable nonlocal pseudopotentials in the Kleinman-Bylander form.[79, 80, 81] In Appendix ?? we outline how this can be accomplished.

2.3 Time-dependent Perturbation Theory

In the independent particle approximation, we use the electron density operator $\hat{\rho}$ to obtain the expectation value of any observable \mathcal{O} as

$$\mathcal{O} = \text{Tr}(\hat{\mathcal{O}}\hat{\rho}) = \text{Tr}(\hat{\rho}\hat{\mathcal{O}}), \quad (2.32)$$

where Tr is the trace and is invariant under cyclic permutations. The dynamic equation of motion for ρ is given by

$$i\hbar \frac{d\hat{\rho}}{dt} = [\hat{H}, \hat{\rho}], \quad (2.33)$$

where it is more convenient to work in the interaction picture. We transform all operators according to

$$\hat{\mathcal{O}}_I = \hat{U}\hat{\mathcal{O}}\hat{U}^\dagger, \quad (2.34)$$

where

$$\hat{U} = e^{i\hat{H}_0 t/\hbar}, \quad (2.35)$$

is the unitary operator that shifts us to the interaction picture. Note that $\hat{\mathcal{O}}_I$ depends on time even if $\hat{\mathcal{O}}$ does not. Then, we transform Eq. (2.33) into

$$i\hbar \frac{d\hat{\rho}_I(t)}{dt} = [-e\hat{\mathbf{r}}_I(t) \cdot \mathbf{E}(t), \hat{\rho}_I(t)], \quad (2.36)$$

that leads to

$$\hat{\rho}_I(t) = \hat{\rho}_I(t = -\infty) + \frac{ie}{\hbar} \int_{-\infty}^t dt' [\hat{\mathbf{r}}_I(t') \cdot \mathbf{E}(t'), \hat{\rho}_I(t')]. \quad (2.37)$$

We assume that the interaction is switched-on adiabatically and choose a time-periodic perturbing field, to write

$$\mathbf{E}(t) = \mathbf{E}e^{-i\omega t}e^{\eta t} = \mathbf{E}e^{-i\tilde{\omega}t}, \quad (2.38)$$

with

$$\tilde{\omega} = \omega + i\eta, \quad (2.39)$$

where $\eta > 0$ assures that at $t = -\infty$ the interaction is zero and has its full strength \mathbf{E} at $t = 0$. After computing the required time integrals one takes $\eta \rightarrow 0$. Also, $\hat{\rho}_I(t = -\infty)$ should be time independent and thus $[\hat{H}, \hat{\rho}]_{t=-\infty} = 0$. This implies that $\hat{\rho}_I(t = -\infty) = \hat{\rho}(t = -\infty) \equiv \hat{\rho}_0$, where $\hat{\rho}_0$ is the density matrix of the unperturbed ground state, such that

$$\langle n\mathbf{k} | \hat{\rho}_0 | m\mathbf{k}' \rangle = f_n(\hbar\omega_n^\sigma(\mathbf{k}))\delta_{nm}\delta(\mathbf{k} - \mathbf{k}'), \quad (2.40)$$

with $f_n(\hbar\omega_n^\sigma(\mathbf{k})) = f_{n\mathbf{k}}$ as the Fermi-Dirac distribution function.

We solve Eq. (2.37) using the standard iterative solution, for which we write

$$\hat{\rho}_I = \hat{\rho}_I^{(0)} + \hat{\rho}_I^{(1)} + \hat{\rho}_I^{(2)} + \cdots, \quad (2.41)$$

where $\hat{\rho}_I^{(N)}$ is the density operator to order N in $\mathbf{E}(t)$. Then, Eq. (2.37) reads

$$\hat{\rho}_I^{(0)} + \hat{\rho}_I^{(1)} + \hat{\rho}_I^{(2)} + \cdots = \hat{\rho}_0 + \frac{ie}{\hbar} \int_{-\infty}^t dt' [\hat{\mathbf{r}}_I(t') \cdot \mathbf{E}(t'), \hat{\rho}_I^{(0)} + \hat{\rho}_I^{(1)} + \hat{\rho}_I^{(2)} + \cdots], \quad (2.42)$$

where, by equating equal orders in the perturbation, we find

$$\hat{\rho}_I^{(0)} \equiv \hat{\rho}_0, \quad (2.43)$$

and

$$\hat{\rho}_I^{(N)}(t) = \frac{ie}{\hbar} \int_{-\infty}^t dt' [\hat{\mathbf{r}}_I(t') \cdot \mathbf{E}(t'), \hat{\rho}_I^{(N-1)}(t')]. \quad (2.44)$$

It is simple to show that matrix elements of Eq. (2.44) satisfy $\langle n\mathbf{k} | \rho_I^{(N+1)}(t) | m\mathbf{k}' \rangle = \rho_{I,nm}^{(N+1)}(\mathbf{k}) \delta(\mathbf{k} - \mathbf{k}')$, with

$$\rho_{I,nm}^{(N+1)}(\mathbf{k}; t) = \frac{ie}{\hbar} \int_{-\infty}^t dt' \langle n\mathbf{k} | [\hat{\mathbf{r}}_I(t'), \hat{\rho}_I^{(N)}(t')] | m\mathbf{k} \rangle \cdot \mathbf{E}(t'). \quad (2.45)$$

We now work out the commutator of Eq. (2.45). Then,

$$\begin{aligned} \langle n\mathbf{k} | [\hat{\mathbf{r}}_I(t), \hat{\rho}_I^{(N)}(t)] | m\mathbf{k} \rangle &= \langle n\mathbf{k} | [\hat{U} \hat{\mathbf{r}} \hat{U}^\dagger, \hat{U} \hat{\rho}^{(N)}(t) \hat{U}^\dagger] | m\mathbf{k} \rangle \\ &= \langle n\mathbf{k} | \hat{U} [\hat{\mathbf{r}}, \hat{\rho}^{(N)}(t)] \hat{U}^\dagger | m\mathbf{k} \rangle \\ &= e^{i\omega_{nm}^\sigma t} \left(\langle n\mathbf{k} | [\hat{\mathbf{r}}_e, \hat{\rho}^{(N)}(t)] + [\hat{\mathbf{r}}_i, \hat{\rho}^{(N)}(t)] | m\mathbf{k} \rangle \right). \end{aligned} \quad (2.46)$$

We calculate the interband term first, so using Eq. (2.31) we obtain

$$\begin{aligned} \langle n\mathbf{k} | [\hat{\mathbf{r}}_e, \hat{\rho}^{(N)}(t)] | m\mathbf{k} \rangle &= \sum_{\ell} \left(\langle n\mathbf{k} | \hat{\mathbf{r}}_e | \ell\mathbf{k} \rangle \langle \ell\mathbf{k} | \hat{\rho}^{(N)}(t) | m\mathbf{k} \rangle \right. \\ &\quad \left. - \langle n\mathbf{k} | \hat{\rho}^{(N)}(t) | \ell\mathbf{k} \rangle \langle \ell\mathbf{k} | \hat{\mathbf{r}}_e | m\mathbf{k} \rangle \right) \\ &= \sum_{\ell \neq n, m} \left(\mathbf{r}_{n\ell}(\mathbf{k}) \rho_{\ell m}^{(N)}(\mathbf{k}; t) - \rho_{n\ell}^{(N)}(\mathbf{k}; t) \mathbf{r}_{\ell m}(\mathbf{k}) \right) \\ &\equiv \mathbf{R}_e^{(N)}(\mathbf{k}; t), \end{aligned} \quad (2.47)$$

and from Eq. (2.23),

$$\langle n\mathbf{k} | [\hat{\mathbf{r}}_i, \hat{\rho}^{(N)}(t)] | m\mathbf{k}' \rangle = i\delta(\mathbf{k} - \mathbf{k}')(\rho_{nm}^{(N)}(t))_{;\mathbf{k}} \equiv \delta(\mathbf{k} - \mathbf{k}')\mathbf{R}_i^{(N)}(\mathbf{k}; t). \quad (2.48)$$

Then Eq. (2.45) becomes

$$\rho_{I,nm}^{(N+1)}(\mathbf{k}; t) = \frac{ie}{\hbar} \int_{-\infty}^t dt' e^{i(\omega_{nm}^\sigma - \tilde{\omega})t'} \left[R_e^{b(N)}(\mathbf{k}; t') + R_i^{b(N)}(\mathbf{k}; t') \right] E^b, \quad (2.49)$$

where the roman superindices a, b, c denote Cartesian components that are summed over if repeated. Starting from the linear response and proceeding from Eq. (2.40) and (2.47),

$$\begin{aligned} R_e^{b(0)}(\mathbf{k}; t) &= \sum_{\ell} \left(r_{n\ell}^b(\mathbf{k}) \rho_{\ell m}^{(0)}(\mathbf{k}) - \rho_{n\ell}^{(0)}(\mathbf{k}) r_{\ell m}^b(\mathbf{k}) \right) \\ &= \sum_{\ell} \left(r_{n\ell}^b(\mathbf{k}) \delta_{\ell m} f_m(\hbar\omega_m^\sigma(\mathbf{k})) - \delta_{n\ell} f_n(\hbar\omega_n^\sigma(\mathbf{k})) r_{\ell m}^b(\mathbf{k}) \right) \\ &= f_{mn\mathbf{k}} r_{nm}^b(\mathbf{k}), \end{aligned} \quad (2.50)$$

where $f_{mn\mathbf{k}} = f_{m\mathbf{k}} - f_{n\mathbf{k}}$. From now on, it should be clear that the matrix elements of \mathbf{r}_{nm} imply $n \notin D_m$. We also have from Eq. (2.48) and Eq. (2.24) that

$$R_i^{b(0)}(\mathbf{k}) = i(\rho_{nm}^{(0)})_{;\mathbf{k}^b} = i\delta_{nm}(f_{n\mathbf{k}})_{;\mathbf{k}^b} = i\delta_{nm}\nabla_{\mathbf{k}^b} f_{n\mathbf{k}}. \quad (2.51)$$

For a semiconductor at $T = 0$, $f_{n\mathbf{k}}$ is one if the state $|n\mathbf{k}\rangle$ is a valence state and zero if it is a conduction state; thus $\nabla_{\mathbf{k}} f_{n\mathbf{k}} = 0$ and $\mathbf{R}_i^{(0)} = 0$ and the linear response has no contribution from intraband transitions. Then,

$$\begin{aligned} \rho_{I,nm}^{(1)}(\mathbf{k}; t) &= \frac{ie}{\hbar} f_{mn\mathbf{k}} r_{nm}^b(\mathbf{k}) E^b \int_{-\infty}^t dt' e^{i(\omega_{nm}^\sigma - \tilde{\omega})t'} \\ &= \frac{e}{\hbar} f_{mn\mathbf{k}} r_{nm}^b(\mathbf{k}) E^b \frac{e^{i(\omega_{nm}^\sigma - \tilde{\omega})t}}{\omega_{nm}^\sigma - \tilde{\omega}} \\ &= e^{i\omega_{nm}^\sigma t} B_{mn}^b(\mathbf{k}) E^b(t) \\ &= e^{i\omega_{nm}^\sigma t} \rho_{nm}^{(1)}(\mathbf{k}; t), \end{aligned} \quad (2.52)$$

with

$$B_{nm}^b(\mathbf{k}, \omega) = \frac{e}{\hbar} \frac{f_{mn\mathbf{k}} r_{nm}^b(\mathbf{k})}{\omega_{nm}^\sigma - \tilde{\omega}}, \quad (2.53)$$

and

$$\rho_{nm}^{(1)}(\mathbf{k}; t) = B_{mn}^b(\mathbf{k}, \omega) E^b(\omega) e^{-i\tilde{\omega}t}. \quad (2.54)$$

Now, we calculate the second-order response. Then, from Eq. (2.47)

$$\begin{aligned} R_e^{b(1)}(\mathbf{k}; t) &= \sum_{\ell} \left(r_{n\ell}^b(\mathbf{k}) \rho_{\ell m}^{(1)}(\mathbf{k}; t) - \rho_{n\ell}^{(1)}(\mathbf{k}; t) r_{\ell m}^b(\mathbf{k}) \right) \\ &= \sum_{\ell} \left(r_{n\ell}^b(\mathbf{k}) B_{\ell m}^c(\mathbf{k}, \omega) - B_{n\ell}^c(\mathbf{k}, \omega) r_{\ell m}^b(\mathbf{k}) \right) E^c(t), \end{aligned} \quad (2.55)$$

and from Eq. (2.48)

$$R_i^{b(1)}(\mathbf{k}; t) = i(\rho_{nm}^{(1)}(t))_{;k^b} = iE^c(t)(B_{nm}^c(\mathbf{k}, \omega))_{;k^b}. \quad (2.56)$$

Using Eqs. (2.55) and (2.56) in Eq. (2.49), we obtain

$$\begin{aligned} \rho_{I,nm}^{(2)}(\mathbf{k}; t) &= \frac{ie}{\hbar} \left[\sum_{\ell} \left(r_{n\ell}^b(\mathbf{k}) B_{\ell m}^c(\mathbf{k}, \omega) - B_{n\ell}^c(\mathbf{k}, \omega) r_{\ell m}^b(\mathbf{k}) \right) \right. \\ &\quad \left. + i(B_{nm}^c(\mathbf{k}, \omega))_{;k^b} \right] E_{\omega}^b E_{\omega}^c \int_{-\infty}^t dt' e^{i(\omega_{nm\mathbf{k}}^{\sigma} - 2\tilde{\omega})t'} \\ &= \frac{e}{\hbar} \left[\sum_{\ell} \left(r_{n\ell}^b(\mathbf{k}) B_{\ell m}^c(\mathbf{k}, \omega) - B_{n\ell}^c(\mathbf{k}, \omega) r_{\ell m}^b(\mathbf{k}) \right) \right. \\ &\quad \left. + i(B_{nm}^c(\mathbf{k}, \omega))_{;k^b} \right] E_{\omega}^b E_{\omega}^c \frac{e^{i(\omega_{nm\mathbf{k}}^{\sigma} - 2\tilde{\omega})t}}{\omega_{nm\mathbf{k}}^{\sigma} - 2\tilde{\omega}} \\ &= e^{i\omega_{nm\mathbf{k}}^{\sigma} t} \rho_{nm}^{(2)}(\mathbf{k}; t). \end{aligned} \quad (2.57)$$

Now, we write $\rho_{nm}^{(2)}(\mathbf{k}; t) = \rho_{nm}^{(2)}(\mathbf{k}; 2\omega) e^{-i2\tilde{\omega}t}$, with

$$\begin{aligned} \rho_{nm}^{(2)}(\mathbf{k}; 2\omega) &= \frac{e}{i\hbar} \frac{1}{\omega_{nm\mathbf{k}}^{\sigma} - 2\tilde{\omega}} \left[- (B_{nm}^c(\mathbf{k}, \omega))_{;k^b} \right. \\ &\quad \left. + i \sum_{\ell} \left(r_{n\ell}^b B_{\ell m}^c(\mathbf{k}, \omega) - B_{n\ell}^c(\mathbf{k}, \omega) r_{\ell m}^b \right) \right] E^b(\omega) E^c(\omega) \end{aligned} \quad (2.58)$$

where $B_{\ell m}^a(\mathbf{k}, \omega)$ are given by Eq. (2.53). We remark that $\mathbf{r}_{nm}(\mathbf{k})$ are the same whether calculated with the LDA or the scissored Hamiltonian. We chose the former in this article.

2.4 Layered Current Density

In this section, we derive the expressions for the microscopic current density of a given layer in the unit cell of the system. The approach we use to study

the surface of a semi-infinite semiconductor crystal is as follows. Instead of using a semi-infinite system, we replace it by a slab (see Fig. 2.2). The slab consists of a front and back surface, and in between these two surfaces is the bulk of the system. In general the surface of a crystal reconstructs or relaxes as the atoms move to find equilibrium positions. This is due to the fact that the otherwise balanced forces are disrupted when the surface atoms do not find their partner atoms that are now absent at the surface of the slab.

To take the reconstruction or relaxation into account, we take “surface” to mean the true surface of the first layer of atoms, and some of the atomic sub-layers adjacent to it. Since the front and the back surfaces of the slab are usually identical the total slab is centrosymmetric. This implies that $\chi_{\text{abc}}^{\text{slab}} = 0$, and thus we must find a way to bypass this characteristic of a centrosymmetric slab in order to have a finite χ_{abc}^s representative of the surface. Even if the front and back surfaces of the slab are different, breaking the centrosymmetry and therefore giving an overall $\chi_{\text{abc}}^{\text{slab}} \neq 0$, we still need a procedure to extract the front surface χ_{abc}^f and the back surface χ_{abc}^b from the non-linear susceptibility $\chi_{\text{abc}}^{\text{slab}} = \chi_{\text{abc}}^f - \chi_{\text{abc}}^b$ of the entire slab.

A convenient way to accomplish the separation of the SH signal of either surface is to introduce a “cut function”, $\mathcal{C}(z)$, which is usually taken to be unity over one half of the slab and zero over the other half.[82] In this case $\mathcal{C}(z)$ will give the contribution of the side of the slab for which $\mathcal{C}(z) = 1$. We can generalize this simple choice for $\mathcal{C}(z)$ by a top-hat cut function $\mathcal{C}^\ell(z)$ that selects a given layer,

$$\mathcal{C}^\ell(z) = \Theta(z - z_\ell + \Delta_\ell^b)\Theta(z_\ell - z + \Delta_\ell^f), \quad (2.59)$$

where Θ is the Heaviside function. Here, $\Delta_\ell^{f/b}$ is the distance that the ℓ -th layer extends towards the front (f) or back (b) from its z_ℓ position. $\Delta_\ell^f + \Delta_\ell^b$ is the thickness of layer ℓ (see Fig. 2.2).

Now, we show how this “cut function” $\mathcal{C}^\ell(z)$ is introduced in the calculation of χ_{abc} . The microscopic current density is given by

$$\mathbf{j}(\mathbf{r}, t) = \text{Tr}(\hat{\mathbf{j}}(\mathbf{r})\hat{\rho}(t)), \quad (2.60)$$

where the operator for the electron’s current is

$$\hat{\mathbf{j}}(\mathbf{r}) = \frac{e}{2} (\hat{\mathbf{v}}^\sigma |\mathbf{r}\rangle \langle \mathbf{r}| + |\mathbf{r}\rangle \langle \mathbf{r}| \hat{\mathbf{v}}^\sigma), \quad (2.61)$$

where $\hat{\mathbf{v}}^\sigma$ is the electron’s velocity operator to be dealt with below. We

define $\hat{\mu} \equiv |\mathbf{r}\rangle\langle\mathbf{r}|$ and use the cyclic invariance of the trace to write

$$\begin{aligned}
\text{Tr}(\hat{\mathbf{j}}(\mathbf{r})\hat{\rho}(t)) &= \text{Tr}(\hat{\rho}(t)\hat{\mathbf{j}}(\mathbf{r})) = \frac{e}{2} (\text{Tr}(\hat{\rho}\hat{\mathbf{v}}^\sigma\hat{\mu}) + \text{Tr}(\hat{\rho}\hat{\mu}\hat{\mathbf{v}}^\sigma)) \\
&= \frac{e}{2} \sum_{n\mathbf{k}} (\langle n\mathbf{k}|\hat{\rho}\hat{\mathbf{v}}^\sigma\hat{\mu}|n\mathbf{k}\rangle + \langle n\mathbf{k}|\hat{\rho}\hat{\mu}\hat{\mathbf{v}}^\sigma|n\mathbf{k}\rangle) \\
&= \frac{e}{2} \sum_{nm\mathbf{k}} \langle n\mathbf{k}|\hat{\rho}|m\mathbf{k}\rangle (\langle m\mathbf{k}|\hat{\mathbf{v}}^\sigma|\mathbf{r}\rangle\langle\mathbf{r}|n\mathbf{k}\rangle + \langle m\mathbf{k}|\mathbf{r}\rangle\langle\mathbf{r}|\hat{\mathbf{v}}^\sigma|n\mathbf{k}\rangle) \\
\mathbf{j}(\mathbf{r}, t) &= \sum_{nm\mathbf{k}} \rho_{nm}(\mathbf{k}; t) \mathbf{j}_{mn}(\mathbf{k}; \mathbf{r}), \tag{2.62}
\end{aligned}$$

where

$$\mathbf{j}_{mn}(\mathbf{k}; \mathbf{r}) = \frac{e}{2} (\langle m\mathbf{k}|\hat{\mathbf{v}}^\sigma|\mathbf{r}\rangle\langle\mathbf{r}|n\mathbf{k}\rangle + \langle m\mathbf{k}|\mathbf{r}\rangle\langle\mathbf{r}|\hat{\mathbf{v}}^\sigma|n\mathbf{k}\rangle), \tag{2.63}$$

are the matrix elements of the microscopic current operator, and we have used the fact that the matrix elements between states $|n\mathbf{k}\rangle$ are diagonal in \mathbf{k} , i.e. proportional to $\delta(\mathbf{k} - \mathbf{k}')$.

Integrating the microscopic current $\mathbf{j}(\mathbf{r}, t)$ over the entire slab gives the averaged microscopic current density. If we want the contribution from only one region of the unit cell towards the total current, we can integrate $\mathbf{j}(\mathbf{r}, t)$ over the desired region. The contribution to the current density from the ℓ -th layer of the slab is given by

$$\frac{1}{\Omega} \int d^3r \mathcal{C}^\ell(z) \mathbf{j}(\mathbf{r}, t) \equiv \mathbf{J}^\ell(t), \tag{2.64}$$

where $\mathbf{J}^\ell(t)$ is the microscopic current in the ℓ -th layer. Therefore we define

$$e\mathcal{V}_{mn}^{\sigma, \ell}(\mathbf{k}) \equiv \int d^3r \mathcal{C}^\ell(z) \mathbf{j}_{mn}(\mathbf{k}; \mathbf{r}), \tag{2.65}$$

to write

$$J_a^{(N, \ell)}(t) = \frac{e}{\Omega} \sum_{mn\mathbf{k}} \mathcal{V}_{mn}^{\sigma, a, \ell}(\mathbf{k}) \rho_{nm}^{(N)}(\mathbf{k}; t), \tag{2.66}$$

as the induced microscopic current of the ℓ -th layer, to order N in the external perturbation. The matrix elements of the density operator for $N = 1, 2$ are given by Eqs. (2.53) and (2.58) respectively. The Fourier component of microscopic current of Eq. (2.66) is given by

$$J_a^{(N, \ell)}(\omega_3) = \frac{e}{\Omega} \sum_{mn\mathbf{k}} \mathcal{V}_{mn}^{\sigma, a, \ell}(\mathbf{k}) \rho_{nm}^{(N)}(\mathbf{k}; \omega_3). \tag{2.67}$$

We proceed to give an explicit expression of $\mathbf{v}_{mn}^{\sigma,\ell}(\mathbf{k})$. From Eqs. (2.65) and (2.63) we obtain

$$\mathbf{v}_{mn}^{\sigma,\ell}(\mathbf{k}) = \frac{1}{2} \int d^3r \mathcal{C}^\ell(z) \left[\langle m\mathbf{k} | \mathbf{v}^\sigma | \mathbf{r} \rangle \langle \mathbf{r} | n\mathbf{k} \rangle + \langle m\mathbf{k} | \mathbf{r} \rangle \langle \mathbf{r} | \mathbf{v}^\sigma | n\mathbf{k} \rangle \right], \quad (2.68)$$

and using the following property

$$\langle \mathbf{r} | \hat{\mathbf{v}}^\sigma(\mathbf{r}, \mathbf{r}') | n\mathbf{k} \rangle = \int d^3r'' \langle \mathbf{r} | \hat{\mathbf{v}}^\sigma(\mathbf{r}, \mathbf{r}') | \mathbf{r}'' \rangle \langle \mathbf{r}'' | n\mathbf{k} \rangle = \hat{\mathbf{v}}^\sigma(\mathbf{r}, \mathbf{r}'') \int d^3r'' \langle \mathbf{r} | \mathbf{r}'' \rangle \langle \mathbf{r}'' | n\mathbf{k} \rangle = \hat{\mathbf{v}}^\sigma(\mathbf{r}, \mathbf{r}') \psi_{n\mathbf{k}}(\mathbf{r}) \quad (2.69)$$

that stems from the fact that the operator $\mathbf{v}^\sigma(\mathbf{r}, \mathbf{r}')$ does not act on \mathbf{r}'' , we can write

$$\begin{aligned} \mathbf{v}_{mn}^{\sigma,\ell}(\mathbf{k}) &= \frac{1}{2} \int d^3r \mathcal{C}^\ell(z) \left[\psi_{n\mathbf{k}}(\mathbf{r}) \hat{\mathbf{v}}^{\sigma*} \psi_{m\mathbf{k}}^*(\mathbf{r}) + \psi_{m\mathbf{k}}^*(\mathbf{r}) \hat{\mathbf{v}}^\sigma \psi_{n\mathbf{k}}(\mathbf{r}) \right] \\ &= \int d^3r \psi_{m\mathbf{k}}^*(\mathbf{r}) \left[\frac{\mathcal{C}^\ell(z) \mathbf{v}^\sigma + \mathbf{v}^\sigma \mathcal{C}^\ell(z)}{2} \right] \psi_{n\mathbf{k}}(\mathbf{r}) \\ &= \int d^3r \psi_{m\mathbf{k}}^*(\mathbf{r}) \mathbf{v}^{\sigma,\ell} \psi_{n\mathbf{k}}(\mathbf{r}). \end{aligned} \quad (2.70)$$

We used the hermitian property of \mathbf{v}^σ and defined

$$\mathbf{v}^{\sigma,\ell} = \frac{\mathcal{C}^\ell(z) \mathbf{v}^\sigma + \mathbf{v}^\sigma \mathcal{C}^\ell(z)}{2}, \quad (2.71)$$

where the superscript ℓ is inherited from $\mathcal{C}^\ell(z)$ and we suppress the dependence on z from the increasingly crowded notation. We see that the replacement

$$\hat{\mathbf{v}}^\sigma \rightarrow \hat{\mathbf{v}}^{\sigma,\ell} = \left[\frac{\mathcal{C}^\ell(z) \hat{\mathbf{v}}^\sigma + \hat{\mathbf{v}}^\sigma \mathcal{C}^\ell(z)}{2} \right], \quad (2.72)$$

is all that is needed to change the velocity operator of the electron $\hat{\mathbf{v}}^\sigma$ to the new velocity operator $\mathbf{v}^{\sigma,\ell}$ that implicitly takes into account the contribution of the region of the slab given by $\mathcal{C}^\ell(z)$. From Eq. (2.25),

$$\begin{aligned} \mathbf{v}^{\sigma,\ell} &= \mathbf{v}^{\text{LDA},\ell} + \mathbf{v}^{\mathcal{S},\ell} \\ \mathbf{v}^{\text{LDA},\ell} &= \mathbf{v}^\ell + \mathbf{v}^{\text{nl},\ell} = \frac{1}{m_e} \mathcal{P}^\ell + \mathbf{v}^{\text{nl},\ell}. \end{aligned} \quad (2.73)$$

We remark that the simple relationship between $\mathbf{v}_{nm}^\sigma(\mathbf{k})$ and $\mathbf{v}_{nm}^{\text{LDA}}(\mathbf{k})$, given in Eq. (2.29), does not hold between $\mathbf{v}_{nm}^{\sigma,\ell}(\mathbf{k})$ and $\mathbf{v}_{nm}^{\text{LDA},\ell}(\mathbf{k})$, i.e. $\mathbf{v}_{nm}^{\sigma,\ell}(\mathbf{k}) \neq$

$(\omega_{nm}^\sigma/\omega_{nm})\mathbf{V}_{nm}^{\text{LDA},\ell}(\mathbf{k})$ and $\mathbf{V}_{nn}^{\sigma,\ell}(\mathbf{k}) \neq \mathbf{V}_{nn}^{\text{LDA},\ell}(\mathbf{k})$, and thus, to calculate $\mathbf{V}_{nm}^{\sigma,\ell}(\mathbf{k})$ we must calculate the matrix elements of $\mathbf{V}^{S,\ell}$ and $\mathbf{V}^{\text{LDA},\ell}$ (separately) according to the expressions of Appendix ?? **Aéroport Charles de Gaulle, Nov. 30, 2014, see Appendix ??**.

To limit the response to one surface, the equivalent of Eq. (2.71) for $\mathbf{V}^\ell = \mathcal{P}^\ell/m_e$ was proposed in Ref. [82] and later used in Refs. [67], [63], [83], and [84] also in the context of SHG. The layer-by-layer analysis of Refs. [85] and [86] used Eq. (2.59), limiting the current response to a particular layer of the slab and used to obtain the anisotropic linear optical response of semiconductor surfaces. However, the first formal derivation of this scheme is presented in Ref. [87] for the linear response, and here in this article, for the second harmonic optical response of semiconductors.

2.5 Microscopic surface susceptibility

In this section we obtain the expressions for the surface susceptibility tensor χ_{abc}^S . We start with the basic relation $\mathbf{J} = d\mathbf{P}/dt$ with \mathbf{J} the current calculated in Sec. 2.4. From Eq. (2.67) we obtain

$$J_{\text{a}}^{(2,\ell)}(2\omega) = -i2\tilde{\omega}P_{\text{a}}(2\omega) = \frac{e}{\Omega} \sum_{mn\mathbf{k}} \mathcal{V}_{mn}^{\sigma,\text{a},\ell}(\mathbf{k}) \rho_{nm}^{(2)}(\mathbf{k}; 2\omega), \quad (2.74)$$

and using Eqs. (2.58) and (2.7) leads to

$$\begin{aligned} \chi_{\text{abc}}^{S,\ell} &= \frac{ie}{AE_1^{\text{b}}E_2^{\text{c}}2\tilde{\omega}} \sum_{mn\mathbf{k}} \mathcal{V}_{mn}^{\sigma,\text{a},\ell}(\mathbf{k}) \rho_{nm}^{(2)}(\mathbf{k}; 2\tilde{\omega}) \\ &= \frac{e^2}{A\hbar 2\tilde{\omega}} \sum_{mn\mathbf{k}} \frac{\mathcal{V}_{mn}^{\sigma,\text{a},\ell}(\mathbf{k})}{\omega_{nm}^\sigma - 2\tilde{\omega}} \left[- (B_{nm}^{\text{c}}(\mathbf{k}, \omega))_{;k^{\text{b}}} \right. \\ &\quad \left. + i \sum_{\ell} \left(r_{n\ell}^{\text{b}} B_{\ell m}^{\text{c}}(\mathbf{k}, \omega) - B_{n\ell}^{\text{c}}(\mathbf{k}, \omega) r_{\ell m}^{\text{b}} \right) \right], \end{aligned} \quad (2.75)$$

which gives the surface-like susceptibility of ℓ -th layer, where \mathbf{V}^σ is given in Eq. (2.73), where $A = \Omega/d$ is the surface area of the unit cell that characterizes the surface of the system. Using Eq. (2.53) we split this equation into two contributions from the first and second terms on the right hand side,

$$\chi_{i,\text{abc}}^{S,\ell} = -\frac{e^3}{A\hbar^2 2\tilde{\omega}} \sum_{mn\mathbf{k}} \frac{\mathcal{V}_{mn}^{\sigma,\text{a},\ell}}{\omega_{nm}^\sigma - 2\tilde{\omega}} \left(\frac{f_{mn} r_{nm}^{\text{b}}}{\omega_{nm}^\sigma - \tilde{\omega}} \right)_{;k^{\text{c}}}, \quad (2.76)$$

and

$$\chi_{e,abc}^{S,\ell} = \frac{ie^3}{A\hbar^2 2\tilde{\omega}} \sum_{\ell m n \mathbf{k}} \frac{\mathcal{V}_{mn}^{\sigma,a,\ell}}{\omega_{nm}^\sigma - \tilde{\omega}} \left(\frac{r_{n\ell}^c r_{\ell m}^b f_{m\ell}}{\omega_{\ell m}^\sigma - \tilde{\omega}} - \frac{r_{n\ell}^b r_{\ell m}^c f_{\ell n}}{\omega_{n\ell}^\sigma - \tilde{\omega}} \right), \quad (2.77)$$

where $\chi_i^{S,\ell}$ is related to intraband transitions and $\chi_e^{S,\ell}$ to interband transitions. For the generalized derivative in Eq. (2.76) we use the chain rule

$$\left(\frac{f_{mn} r_{nm}^b}{\omega_{nm}^\sigma - \tilde{\omega}} \right)_{;k^c} = \frac{f_{mn}}{\omega_{nm}^\sigma - \tilde{\omega}} \left(r_{nm}^b \right)_{;k^c} - \frac{f_{mn} r_{nm}^b \Delta_{nm}^c}{(\omega_{nm}^\sigma - \tilde{\omega})^2}, \quad (2.78)$$

and the following result shown in Appendix ??,

$$(\omega_{nm}^\sigma)_{;k^a} = (\omega_{nm}^{\text{LDA}})_{;k^a} = v_{nn}^{\text{LDA},a} - v_{mm}^{\text{LDA},a} \equiv \Delta_{nm}^a. \quad (2.79)$$

In order to calculate the nonlinear susceptibility of any given layer ℓ we simply add the above terms $\chi^{S,\ell} = \chi_e^{S,\ell} + \chi_i^{S,\ell}$ and then calculate the surface susceptibility as

$$\chi^S \equiv \sum_{\ell=1}^N \chi^{S,\ell}, \quad (2.80)$$

where $\ell = 1$ is the first layer right at the surface, and $\ell = N$ is the bulk-like layer (at a distance $\sim d$ from the surface as seen in Fig. 2.1), such that

$$\chi^{S,\ell=N} = 0, \quad (2.81)$$

in accordance to Eq. (2.5) valid for a centrosymmetric environment. We note that the value of N is not universal. This means that the slab needs to have enough atomic layers for Eq. (2.81) to be satisfied and to give converged results for χ^S . We can use Eq. (2.80) for either the front or the back surface.

We can see from the prefactors of Eqs. (2.76) and (2.77) that they diverge as $\tilde{\omega} \rightarrow 0$. To remove this apparent divergence of $\chi^{S,\ell}$, we perform a partial fraction expansion over $\tilde{\omega}$. As shown in Appendix ??, we use time-reversal invariance to remove these divergences and obtain the following expressions for χ^S ,

$$\text{Im}[\chi_{e,abc,\omega}^{s,\ell}] = \frac{\pi|e|^3}{2\hbar^2} \sum_{v\mathbf{c}\mathbf{k}} \sum_{l \neq (v,c)} \frac{1}{\omega_{cv}^\sigma} \left[\frac{\text{Im}[\mathcal{V}_{lc}^{\sigma,a,\ell} \{r_{cv}^b r_{vl}^c\}]}{(2\omega_{cv}^\sigma - \omega_{cl}^\sigma)} - \frac{\text{Im}[\mathcal{V}_{vl}^{\sigma,a,\ell} \{r_{lc}^c r_{cv}^b\}]}{(2\omega_{cv}^\sigma - \omega_{lv}^\sigma)} \right] \delta(\omega_{cv}^\sigma - \omega), \quad (2.82)$$

$$\text{Im}[\chi_{i,abc,\omega}^{s,\ell}] = \frac{\pi|e|^3}{2\hbar^2} \sum_{c\mathbf{v}\mathbf{k}} \frac{1}{(\omega_{cv}^\sigma)^2} \left[\text{Re} \left[\left\{ r_{cv}^b \left(\mathcal{V}_{vc}^{\sigma,a,\ell} \right)_{;k^c} \right\} \right] + \frac{\text{Re} \left[\mathcal{V}_{vc}^{\sigma,a,\ell} \{r_{cv}^b \Delta_{cv}^c\} \right]}{\omega_{cv}^\sigma} \right] \delta(\omega_{cv}^\sigma - \omega), \quad (2.83)$$

$$\text{Im}[\chi_{e,\text{abc},2\omega}^{s,\ell}] = -\frac{\pi|e|^3}{2\hbar^2} \sum_{v\mathbf{c}\mathbf{k}} \frac{4}{\omega_{cv}^\sigma} \left[\sum_{v' \neq v} \frac{\text{Im}[\mathcal{V}_{vc}^{\sigma,\text{a},\ell} \{r_{cv'}^{\text{b}}, r_{v'v}^{\text{c}}\}]}{2\omega_{cv'}^\sigma - \omega_{cv}^\sigma} - \sum_{c' \neq c} \frac{\text{Im}[\mathcal{V}_{vc}^{\sigma,\text{a},\ell} \{r_{cc'}^{\text{c}}, r_{c'v}^{\text{b}}\}]}{2\omega_{c'v}^\sigma - \omega_{cv}^\sigma} \right] \delta(\omega_{cv}^\sigma - 2\omega), \quad (2.84)$$

and

$$\text{Im}[\chi_{i,\text{abc},2\omega}^{s,\ell}] = \frac{\pi|e|^3}{2\hbar^2} \sum_{v\mathbf{c}\mathbf{k}} \frac{4}{(\omega_{cv}^\sigma)^2} \left[\text{Re} \left[\mathcal{V}_{vc}^{\sigma,\text{a},\ell} \left\{ \left(r_{cv}^{\text{b}} \right)_{;k^c} \right\} \right] - \frac{2\text{Re} \left[\mathcal{V}_{vc}^{\sigma,\text{a},\ell} \{ r_{cv}^{\text{b}} \Delta_{cv}^{\text{c}} \} \right]}{\omega_{cv}^\sigma} \right] \delta(\omega_{cv}^\sigma - 2\omega), \quad (2.85)$$

where the limit of $\eta \rightarrow 0$ has been taken. We have split the interband and intraband 1ω and 2ω contributions. The real part of each contribution can be obtained through a Kramers-Kronig transformation,[88] and then $\chi_{\text{abc}}^{S,\ell} = \chi_{e,\text{abc},\omega}^{S,\ell} + \chi_{e,\text{abc},2\omega}^{S,\ell} + \chi_{i,\text{abc},\omega}^{S,\ell} + \chi_{i,\text{abc},2\omega}^{S,\ell}$. To fulfill the required intrinsic permutation symmetry,[89] the $\{\}$ notation symmetrizes the bc Cartesian indices, i.e. $\{u^{\text{b}}s^{\text{c}}\} = (u^{\text{b}}s^{\text{c}} + u^{\text{c}}s^{\text{b}})/2$, and thus $\chi_{\text{abc}}^{S,\ell} = \chi_{\text{acb}}^{S,\ell}$. In Appendices ?? and ?? we demonstrate how to calculate the generalized derivatives of $\mathbf{r}_{nm;\mathbf{k}}$ and $\mathcal{V}_{nm;\mathbf{k}}^{\sigma,\text{a},\ell}$. We find that

$$(r_{nm}^{\text{b}})_{;k^{\text{a}}} = -i\mathcal{T}_{nm}^{\text{ab}} + \frac{r_{nm}^{\text{a}}\Delta_{mn}^{\text{b}} + r_{nm}^{\text{b}}\Delta_{mn}^{\text{a}}}{\omega_{nm}^{\text{LDA}}} + \frac{i}{\omega_{nm}^{\text{LDA}}} \sum_{\ell} \left(\omega_{\ell m}^{\text{LDA}} r_{n\ell}^{\text{a}} r_{\ell m}^{\text{b}} - \omega_{n\ell}^{\text{LDA}} r_{n\ell}^{\text{b}} r_{\ell m}^{\text{a}} \right), \quad (2.86)$$

where

$$\mathcal{T}_{nm}^{\text{ab}} = [r^{\text{a}}, v^{\text{LDA},\text{b}}] = \frac{i\hbar}{m_e} \delta_{ab} \delta_{nm} + \mathcal{L}_{nm}^{\text{ab}}, \quad (2.87)$$

and

$$\mathcal{L}_{nm}^{\text{ab}} = \frac{1}{i\hbar} [r^{\text{a}}, v^{\text{nl},\text{b}}]_{nm}, \quad (2.88)$$

is the contribution to the generalized derivative of \mathbf{r}_{nm} coming from the nonlocal part of the pseudopotential. In Appendix ?? we calculate $\mathcal{L}_{nm}^{\text{ab}}$, that is a term with very small numerical value but with a computational time at least an order of magnitude larger than for all the other terms involved in the expressions for $\chi_{\text{abc}}^{s,\ell}$. [90] Therefore, we neglect it throughout this article and take

$$\mathcal{T}_{nm}^{\text{ab}} \approx \frac{i\hbar}{m_e} \delta_{ab} \delta_{nm}. \quad (2.89)$$

Finally, we also need the following term (Eq. (??))

$$\begin{aligned} (v_{nn}^{\text{LDA},a})_{;k^b} &= \nabla_{k^a} v_{nn}^{\text{LDA},b}(\mathbf{k}) = -i\mathcal{T}_{nn}^{ab} - \sum_{\ell \neq n} \omega_{\ell n}^{\text{LDA}} \left(r_{n\ell}^a r_{\ell n}^b + r_{n\ell}^b r_{\ell n}^a \right) \\ &\approx \frac{\hbar}{m_e} \delta_{ab} - \sum_{\ell \neq n} \omega_{\ell n}^{\text{LDA}} \left(r_{n\ell}^a r_{\ell n}^b + r_{n\ell}^b r_{\ell n}^a \right), \end{aligned} \quad (2.90)$$

among other quantities for $\mathcal{V}_{nm;\mathbf{k}}^{\sigma,a,\ell}$, where we also use Eq. (2.89). Above is the standard effective-mas sum rule. [91]

2.6 Conclusions

We have presented a complete derivation of the required elements to calculate in the independent particle approach (IPA) the microscopic surface second harmonic susceptibility tensor $\chi^S(-2\omega; \omega, \omega)$ using a layer-by-layer approach. We have done so for semiconductors using the length gauge for the coupling of the external electric field to the electron.

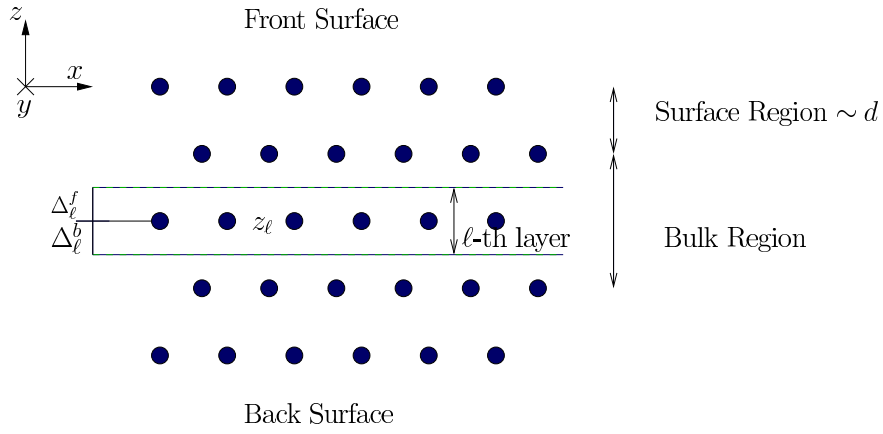


Figure 2.2: A sketch of a slab where the circles represent atoms.

CHAPTER 3

SHG YIELD

3.1 Three layer model for SHG radiation

In this section we derive the formulas required for the calculation of the SHG yield, defined by

$$\mathcal{R}(\omega) = \frac{I(2\omega)}{I^2(\omega)}, \quad (3.1)$$

with the intensity in the MKS system is given by[92]

$$I(\omega) = 2n(\omega)\epsilon_0 c |E(\omega)|^2, \quad (3.2)$$

where $n(\omega) = \sqrt{\epsilon(\omega)}$ is the index of refraction with $\epsilon(\omega)$ the dielectric function, ϵ_0 is the vacuum permittivity, and c the speed of light in vacuum.

There are several ways to calculate \mathcal{R} , one of which is the procedure followed by Cini [93]. This approach calculates the nonlinear susceptibility and at the same time the radiated fields. However, we present an alternative derivation based in the work of Mizrahi and Sipe [94], since the derivation of the three-layer-model is straightforward. In this scheme, we represent the surface by three regions or layers. The first layer is the vacuum region (denoted by v) with a dielectric function $\epsilon_v(\omega) = 1$ from where the fundamental electric field $\mathbf{E}_v(\omega)$ impinges on the material. The second layer is a thin layer (denoted by ℓ) of thickness d characterized by a dielectric function $\epsilon_\ell(\omega)$. Is in this layer where the second harmonic generation takes place. The third layer is the bulk region denoted by b and characterized by $\epsilon_b(\omega)$. Both the vacuum layer and the bulk layer are semiinfinite (see Fig. 3.1).

To model the electromagnetic response of the three-layer model we follow Ref. [94], and assume a polarization sheet of the form

$$\mathbf{P}(\mathbf{r}, t) = \mathcal{P} e^{i\boldsymbol{\kappa} \cdot \mathbf{R}} e^{-i\omega t} \delta(z - z_\beta) + \text{c.c.}, \quad (3.3)$$

where $\mathbf{R} = (x, y)$, $\boldsymbol{\kappa}$ is the component of the wave vector $\boldsymbol{\nu}_\beta$ parallel to the surface, and z_β is the position of the sheet within medium β (see Fig. 3.1).

In Ref. [95] it has been shown that the solution of the Maxwell equations for the radiated fields $E_{\beta,p\pm}$ and $E_{\beta,s}$ with $\mathbf{P}(\mathbf{r}, t)$ as a source can be written, at points $z \neq 0$, as

$$(E_{\beta,p\pm}, E_{\beta,s}) = \left(\frac{\gamma i \tilde{\omega}^2}{\tilde{w}_\beta} \hat{\mathbf{p}}_{\beta\pm} \cdot \mathcal{P}, \frac{\gamma i \tilde{\omega}^2}{\tilde{w}_\beta} \hat{\mathbf{s}} \cdot \mathcal{P} \right), \quad (3.4)$$

where $\gamma = 2\pi$ in cgs units and $\gamma = 1/2\epsilon_0$ in MKS units. Also, $\hat{\mathbf{s}}$ and $\hat{\mathbf{p}}_{\beta\pm}$ are the unitary vectors for the s and p polarization of the radiated field, respectively, and the \pm refers to upward (+) or downward (−) direction of propagation within medium β , as shown in Fig. 3.1, and $\tilde{\omega} = \omega/c$. Also, $\tilde{w}_\beta(\omega) = \tilde{\omega} w_\beta$, where

$$w_\beta(\omega) = (\epsilon_\beta(\omega) - \sin^2 \theta_0)^{1/2}, \quad (3.5)$$

where θ_0 is the angle of incidence of $\mathbf{E}_v(\omega)$, and

$$\hat{\mathbf{p}}_{\beta\pm}(\omega) = \frac{\kappa(\omega) \hat{\mathbf{z}} \mp \tilde{w}_\beta(\omega) \hat{\boldsymbol{\kappa}}}{\tilde{\omega} n_\beta(\omega)} = \frac{\sin \theta_0 \hat{\mathbf{z}} \mp w_\beta(\omega) \hat{\boldsymbol{\kappa}}}{n_\beta(\omega)}, \quad (3.6)$$

where $\kappa(\omega) = |\boldsymbol{\kappa}| = \tilde{\omega} \sin \theta_0$, $n_\beta(\omega) = \sqrt{\epsilon_\beta(\omega)}$ is the index of refraction of medium β , and z is the direction perpendicular to the surface that points towards the vacuum. We chose the plane of incidence along the $\boldsymbol{\kappa}z$ plane, then

$$\hat{\boldsymbol{\kappa}} = \cos \phi \hat{\mathbf{x}} + \sin \phi \hat{\mathbf{y}}, \quad (3.7)$$

and

$$\hat{\mathbf{s}} = -\sin \phi \hat{\mathbf{x}} + \cos \phi \hat{\mathbf{y}}, \quad (3.8)$$

where ϕ the angle with respect to the x axis.

In the three-layer model the nonlinear polarization responsible for the second harmonic generation (SHG) is immersed in the thin $\beta = \ell$ layer, and is given by

$$\mathcal{P}_i(2\omega) = \begin{cases} \chi_{ijk}(2\omega) E_j(\omega) E_k(\omega) & \text{(cgs units)} \\ \epsilon_0 \chi_{ijk}(2\omega) E_j(\omega) E_k(\omega) & \text{(MKS units)} \end{cases}, \quad (3.9)$$

where the tensor $\chi(2\omega)$ is the surface nonlinear dipolar susceptibility and the Cartesian indices i, j, k are summed if repeated. Also, $\chi_{ijk}(2\omega) = \chi_{ikj}(2\omega)$ is the intrinsic permutation symmetry due to the fact that SHG is degenerate in $E_j(\omega)$ and $E_k(\omega)$. As it was done in Ref. [94], in presenting the results Eq. (3.4)-(3.8) we have taken the polarization sheet (Eq. (3.3))

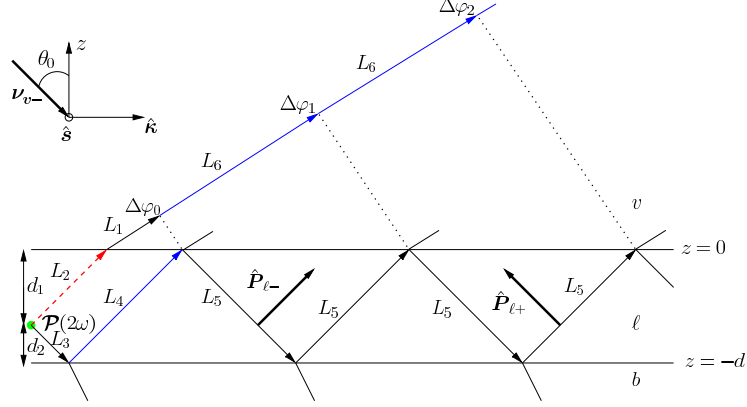


Figure 3.1: Sketch of the three layer model for SHG. Vacuum (v) is on top with $\epsilon_v = 1$; the layer ℓ , of thickness $d = d_1 + d_2$, is characterized with $\epsilon_\ell(\omega)$, and it is where the SH polarization sheet $\mathcal{P}(2\omega)$ is located at $z = d_1$; The bulk b is described with $\epsilon_b(\omega)$. The arrows point along the direction of propagation, and the p -polarization unit vector, $\hat{\mathbf{P}}_{\ell-/+}$, along the downward (upward) direction is denoted with a thick arrow. The s -polarization unit vector $\hat{\mathbf{s}}$, points out of the page. The fundamental field $\mathbf{E}(\omega)$ is incident from the vacuum side along the $z\hat{\mathbf{k}}$ -plane, with θ_0 its angle of incidence and $\boldsymbol{\nu}_{v-}$ its wave vector. $\Delta\varphi_i$ denote the phase difference of the multiply reflected beams with respect to the first vacuum transmitted beam (dashed-red arrow), where the dotted lines are perpendicular to this beam (see the text for details).

to be oscillating at some frequency ω . However, in the following we find it convenient to use ω exclusively to denote the fundamental frequency and $\boldsymbol{\kappa}$ to denote the component of the incident wave vector parallel to the surface. Then the nonlinear generated polarization is oscillating at $\Omega = 2\omega$ and will be characterized by a wave vector parallel to the surface $\mathbf{K} = 2\boldsymbol{\kappa}$. We can carry over Eqs. (3.3)-(3.8) simply by replacing the lowercase symbols $(\omega, \tilde{\omega}, \boldsymbol{\kappa}, n_\beta, \tilde{w}_\beta, w_\beta, \hat{\mathbf{P}}_{\beta\pm}, \hat{\mathbf{s}})$ with uppercase symbols $(\Omega, \tilde{\Omega}, \mathbf{K}, N_\beta, \tilde{W}_\beta, W_\beta, \hat{\mathbf{P}}_{\beta\pm}, \hat{\mathbf{S}})$, all evaluated at 2ω and we always have $\hat{\mathbf{S}} = \hat{\mathbf{s}}$.

To describe the propagation of the SH field, we see from Fig. 3.1, that it is refracted at the layer-vacuum interface (ℓv), and multiply reflected from the layer-bulk (ℓb) and layer-vacuum (ℓv) interfaces, thus we can define,

$$\mathbf{T}^{\ell v} = \hat{\mathbf{s}} T_s^{\ell v} \hat{\mathbf{s}} + \hat{\mathbf{P}}_{v+} T_p^{\ell v} \hat{\mathbf{P}}_{\ell+}, \quad (3.10)$$

as the tensor for transmission from ℓv interface,

$$\mathbf{R}^{\ell b} = \hat{\mathbf{s}} R_s^{\ell b} \hat{\mathbf{s}} + \hat{\mathbf{P}}_{\ell+} R_p^{\ell b} \hat{\mathbf{P}}_{\ell-}, \quad (3.11)$$

as the tensor of reflection from the ℓb interface, and

$$\mathbf{R}^{\ell v} = \hat{\mathbf{s}} R_s^{\ell v} \hat{\mathbf{s}} + \hat{\mathbf{P}}_{\ell-} R_p^{\ell v} \hat{\mathbf{P}}_{\ell+}, \quad (3.12)$$

as that of the ℓv interface. The Fresnel factors in uppercase letters, $T_{s,p}^{ij}$ and $R_{s,p}^{ij}$, are evaluated at 2ω from the following well known formulas

$$\begin{aligned} t_s^{ij}(\omega) &= \frac{2k_i(\omega)}{k_i(\omega) + k_j(\omega)}, & t_p^{ij}(\omega) &= \frac{2k_i(\omega)\sqrt{\epsilon_i(\omega)\epsilon_j(\omega)}}{k_i(\omega)\epsilon_j(\omega) + k_j(\omega)\epsilon_i(\omega)}, \\ r_s^{ij}(\omega) &= \frac{k_i(\omega) - k_j(\omega)}{k_i(\omega) + k_j(\omega)}, & r_p^{ij}(\omega) &= \frac{k_i(\omega)\epsilon_j(\omega) - k_j(\omega)\epsilon_i(\omega)}{k_i(\omega)\epsilon_j(\omega) + k_j(\omega)\epsilon_i(\omega)}. \end{aligned} \quad (3.13)$$

From these expressions one can show that,

$$\begin{aligned} 1 + r_s^{\ell b} &= t_s^{\ell b} \\ 1 + r_p^{\ell b} &= \frac{n_b}{n_\ell} t_p^{\ell b} \\ 1 - r_p^{\ell b} &= \frac{n_\ell}{n_b} \frac{w_b}{w_\ell} t_p^{\ell b} \\ t_p^{\ell v} &= \frac{w_\ell}{w_v} t_p^{v\ell} \\ t_s^{\ell v} &= \frac{w_\ell}{w_v} t_s^{v\ell}. \end{aligned} \quad (3.14)$$

3.1.1 Multiple SH reflections

The SH field $\mathbf{E}(2\omega)$ radiated by the SH polarization $\mathcal{P}(2\omega)$ will radiate directly into vacuum and also into the bulk, where it will be reflected back at the thin-layer-bulk interface into the thin layer again and this beam will be multiple-transmitted and reflected as shown in Fig. 3.1. As the two beams propagate a phase difference will develop between them, according to

$$\begin{aligned} \Delta\varphi_m &= \tilde{\Omega} \left((L_3 + L_4 + 2mL_5)N_\ell - (L_2N_\ell + (L_1 + mL_6)N_v) \right) \\ &= \delta_0 + m\delta \quad m = 0, 1, 2, \dots, \end{aligned} \quad (3.15)$$

where

$$\delta_0 = 8\pi \left(\frac{d_2}{\lambda_0} \right) \sqrt{n_\ell^2(2\omega) - \sin^2 \theta_0}, \quad (3.16)$$

$$\delta = 8\pi \left(\frac{d}{\lambda_0} \right) \sqrt{n_\ell^2(2\omega) - \sin^2 \theta_0}, \quad (3.17)$$

where λ_0 is the wavelength of the fundamental field in vacuum, d the thickness of layer ℓ and d_2 the distance of $\mathcal{P}(2\omega)$ from the ℓb interface (see Fig. 3.1). We see that δ_0 is the phase difference of the first and second transmitted beams, and $m\delta$ that of the first and third ($m = 1$), fourth ($m = 2$), etc. beams (see Fig. 3.1).

To take into account the multiple reflections of the generated SH field in the layer ℓ , we proceed as follows. We show the algebra for the p -polarized SH field, the s -polarized field could be worked out along the same steps. The multiple-reflected $\mathbf{E}_p(2\omega)$ field is given by

$$\begin{aligned} \mathbf{E}(2\omega) &= E_{p+}(2\omega) \mathbf{T}^{\ell v} \cdot \hat{\mathbf{P}}_{\ell+} + E_{p-}(2\omega) \mathbf{T}^{\ell v} \cdot \mathbf{R}^{\ell b} \cdot \hat{\mathbf{P}}_{\ell-} e^{i\Delta\varphi_0} + E_{p-}(2\omega) \mathbf{T}^{\ell v} \cdot \mathbf{R}^{\ell b} \cdot \mathbf{R}^{\ell v} \cdot \mathbf{R}^{\ell b} \cdot \hat{\mathbf{P}}_{\ell-} e^{i\Delta\varphi_2} \\ &\quad + E_{p-}(2\omega) \mathbf{T}^{\ell v} \cdot \mathbf{R}^{\ell b} \cdot \mathbf{R}^{\ell v} \cdot \mathbf{R}^{\ell b} \cdot \mathbf{R}^{\ell v} \cdot \mathbf{R}^{\ell b} \cdot \hat{\mathbf{P}}_{\ell-} e^{i\Delta\varphi_2} + \dots \\ &= E_{p+}(2\omega) \mathbf{T}^{\ell v} \cdot \hat{\mathbf{P}}_{\ell+} + E_{p-}(2\omega) \mathbf{T}^{\ell v} \cdot \sum_{m=0}^{\infty} (\mathbf{R}^{\ell b} \cdot \mathbf{R}^{\ell v} e^{i\delta})^m \cdot \mathbf{R}^{\ell b} \cdot \hat{\mathbf{P}}_{\ell-} e^{i\delta_0}. \end{aligned} \quad (3.18)$$

From Eqs. (3.10)-(3.12) is easy to show that

$$\mathbf{T}^{\ell v} \cdot (\mathbf{R}^{\ell b} \cdot \mathbf{R}^{\ell v})^n \cdot \mathbf{R}^{\ell b} = \hat{\mathbf{s}} T_s^{\ell v} (R_s^{\ell b} R_s^{\ell v})^n R_s^{\ell b} \hat{\mathbf{s}} + \hat{\mathbf{P}}_{v+} T_p^{\ell v} (R_p^{\ell b} R_p^{\ell v})^n R_p^{\ell b} \hat{\mathbf{P}}_{\ell-}, \quad (3.19)$$

then,

$$\mathbf{E}(2\omega) = \hat{\mathbf{P}}_{\ell+} T_p^{\ell v} \left(E_{p+}(2\omega) + \frac{R_p^{\ell b} e^{i\delta_0}}{1 + R_p^{v\ell} R_p^{\ell b} e^{i\delta}} E_{p-}(2\omega) \right), \quad (3.20)$$

where we used $R_{s,p}^{ij} = -R_{s,p}^{ji}$. Using Eq. (3.4), we can readily write

$$\mathbf{E}(2\omega) = \frac{\gamma i \tilde{\Omega}}{W_\ell} \mathbf{H}_\ell \cdot \mathcal{P}(2\omega), \quad (3.21)$$

where

$$\mathbf{H}_\ell = \hat{\mathbf{s}} T_s^{\ell v} (1 + R_s^M) \hat{\mathbf{s}} + \hat{\mathbf{P}}_{v+} T_p^{\ell v} (\hat{\mathbf{P}}_{\ell+} + R_p^M \hat{\mathbf{P}}_{\ell-}). \quad (3.22)$$

and

$$R_l^M \equiv \frac{R_l^{\ell b} e^{i\delta_0}}{1 + R_l^{v\ell} R_l^{\ell b} e^{i\delta}} \quad l = s, p, \quad (3.23)$$

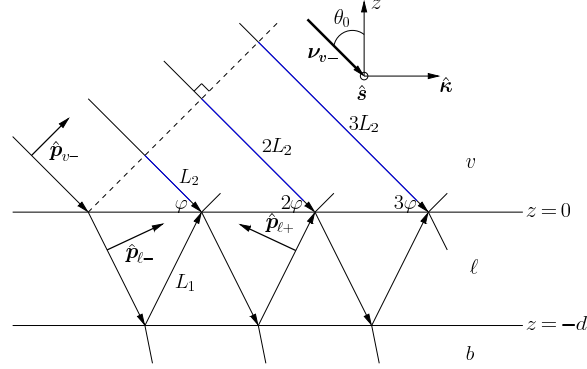


Figure 3.2: (color on line) Sketch for the multiple reflected fundamental field $\mathbf{E}(\omega)$, which impinges from the vacuum side along the $z\hat{\kappa}$ -plane, with θ_0 and ν_{v-} its angle of incidence and wave vector, respectively. The arrows point along the direction of propagation. The p -polarization unit vectors, $\hat{\mathbf{p}}_{\beta\pm}$, along the downward (-) or upward (+) direction are denoted with thick arrows, where $\beta = v$ or ℓ . The s -polarization unit vector $\hat{\mathbf{s}}$ points out of the page, and $(1, 2, 3, \dots)\phi$ denotes the phase difference for the multiply reflected beams with respect to the incident field, where the dotted line is perpendicular to this beam (see the text for details).

is defined as the multiple (M) reflection coefficient. To make touch with the work of Ref. [94] where $\mathcal{P}(2\omega)$ is located on top of the vacuum-surface interface and only the vacuum radiated beam and the first (and only) reflected beam need to be considered, we take $\ell = v$ and $d_2 = 0$, then $T^{\ell v} = 1$, $R^{v\ell} = 0$ and $\delta_0 = 0$, with which $R_i^M = R_i^{vb}$. Thus, Eq. (3.22) coincides with Eq. (3.8) of Ref. [94].

3.1.2 Multiple reflections for the linear field

Similar to the SH field, here we consider the multiple reflections of the fundamental field $\mathbf{E}(\omega)$ inside the thin ℓ layer. In Fig. 3.2 we show the situation where $\mathbf{E}(\omega)$ impinges from the vacuum side with an angle of incidence θ_0 . As the first transmitted beam is multiply reflected from the ℓb and the ℓv interfaces, it accumulates a phase difference of $n\phi$, with $n = 1, 2, 3, \dots$, given

by

$$\begin{aligned}\phi &= \frac{\omega}{c}(2L_1n_\ell - L_2n_v) \\ &= 4\pi \left(\frac{d}{\lambda_0} \right) \sqrt{n_\ell^2 - \sin^2 \theta_0},\end{aligned}\quad (3.24)$$

where $n_v = 1$. Besides the equivalent of Eqs. (3.11) and (3.12), for ω , we also need

$$\mathbf{t}^{v\ell} = \hat{\mathbf{s}} t_s^{v\ell} \hat{\mathbf{s}} + \hat{\mathbf{p}}_{\ell-} t_p^{v\ell} \hat{\mathbf{p}}_{v-}, \quad (3.25)$$

to write

$$\begin{aligned}\mathbf{E}(\omega) &= E_0 \left[\mathbf{t}^{v\ell} + \mathbf{r}^{\ell b} \cdot \mathbf{t}^{v\ell} e^{i\phi} + \mathbf{r}^{\ell b} \cdot \mathbf{r}^{\ell v} \cdot \mathbf{r}^{\ell b} \cdot \mathbf{t}^{v\ell} e^{i2\phi} + \mathbf{r}^{\ell b} \cdot \mathbf{r}^{\ell v} \cdot \mathbf{r}^{\ell b} \cdot \mathbf{r}^{\ell v} \cdot \mathbf{r}^{\ell b} \cdot \mathbf{t}^{v\ell} e^{i3\phi} + \dots \right] \cdot \mathbf{e}^{\text{in}} \\ &= E_0 \left[1 + \left(1 + \mathbf{r}^{\ell b} \cdot \mathbf{r}^{\ell v} e^{i\phi} + (\mathbf{r}^{\ell b} \cdot \mathbf{r}^{\ell v})^2 e^{i2\phi} + \dots \right) \cdot \mathbf{r}^{\ell b} e^{i\phi} \right] \cdot \mathbf{t}^{v\ell} \cdot \mathbf{e}^{\text{in}} \\ &= E_0 \left[\hat{\mathbf{s}} t_s^{v\ell} (1 + r_s^M) \hat{\mathbf{s}} + t_p^{v\ell} (\hat{\mathbf{p}}_{\ell-} + \hat{\mathbf{p}}_{\ell+} r_p^M) \hat{\mathbf{p}}_{v-} \right] \cdot \mathbf{e}^{\text{in}}\end{aligned}\quad (3.26)$$

where

$$r_l^M = \frac{r_l^{\ell b} e^{i\phi}}{1 + r_l^{v\ell} r_l^{\ell b} e^{i\phi}} \quad l = s, p. \quad (3.27)$$

We define $\mathbf{E}^l(\omega) \equiv E_0 \mathbf{e}_\ell^{\omega, l}$ ($l = s, p$), where using Eq. (3.6), we obtain that

$$\mathbf{e}_\ell^{\omega, p} = \frac{t_p^{v\ell}}{n_\ell} \left(r_p^{M+} \sin \theta_0 \hat{\mathbf{z}} + r_p^{M-} w_\ell \hat{\mathbf{k}} \right), \quad (3.28)$$

for p -input polarization, i.e. $\mathbf{e}^{\text{in}} = \hat{\mathbf{p}}_{v-}$, and

$$\mathbf{e}_\ell^{\omega, s} = t_s^{v\ell} r_s^{M+} \hat{\mathbf{s}}, \quad (3.29)$$

for s -input polarization, i.e. $\mathbf{e}^{\text{in}} = \hat{\mathbf{s}}$, where

$$r_l^{M\pm} = 1 \pm r^M \quad l = s, p. \quad (3.30)$$

3.1.3 SHG Yield

The magnitude of the radiated field is given by $E(2\omega) = \hat{\mathbf{e}}^{\text{out}} \cdot \mathbf{E}(2\omega)$, where $\hat{\mathbf{e}}^{\text{out}}$ is the polarization vector of the radiated field, for instance $\hat{\mathbf{s}}$ or $\hat{\mathbf{p}}_{v+}$. Then, we write

$$\begin{aligned}\hat{\mathbf{p}}_{\ell+} + R_p^M \hat{\mathbf{p}}_{\ell-} &= \frac{\sin \theta_0 \hat{\mathbf{z}} - W_\ell \hat{\mathbf{k}}}{N_\ell} + R_p^M \frac{\sin \theta_0 \hat{\mathbf{z}} + W_\ell \hat{\mathbf{k}}}{N_\ell} \\ &= \frac{1}{N_\ell} \left(\sin \theta_0 R_{p+}^M \hat{\mathbf{z}} - K_\ell R_{p-}^M \hat{\mathbf{k}} \right),\end{aligned}\quad (3.31)$$

where

$$R_l^{M\pm} \equiv 1 \pm R_l^M \quad l = s, p. \quad (3.32)$$

Using Eq. (3.14) we write Eq. (3.21) as

$$E(2\omega) = \frac{2\gamma i\omega}{cW_\ell} \hat{\mathbf{e}}^{\text{out}} \cdot \mathbf{H}_\ell \cdot \mathcal{P}(2\omega) = \frac{2\gamma i\omega}{cW_v} \mathbf{e}_\ell^{2\omega} \cdot \mathcal{P}(2\omega). \quad (3.33)$$

$$\mathbf{e}_\ell^{2\omega} = \hat{\mathbf{e}}^{\text{out}} \cdot \left[\hat{\mathbf{s}} T_s^{v\ell} R_s^{M+} \hat{\mathbf{s}} + \hat{\mathbf{P}}_{v+} \frac{T_p^{v\ell}}{N_\ell} (\sin \theta_0 R_p^{M+} \hat{\mathbf{z}} - W_\ell R_p^{M-} \hat{\mathbf{\kappa}}) \right]. \quad (3.34)$$

We pause here to reduce above result to the case where the nonlinear polarization $\mathcal{P}(2\omega)$ radiates from vacuum instead from the layer ℓ . For such case we simply take $\epsilon_\ell(2\omega) = 1$ and $\ell = v$ ($T_{s,p}^{lv} = 1$), to get

$$\mathbf{e}_v^{2\omega} = \hat{\mathbf{e}}^{\text{out}} \cdot \left[\hat{\mathbf{s}} T_s^{vb} \hat{\mathbf{s}} + \hat{\mathbf{P}}_{v+} \frac{T_p^{vb}}{\sqrt{\epsilon_b(2\omega)}} (\epsilon_b(2\omega) \sin \theta_0 \hat{\mathbf{z}} - W_b \hat{\mathbf{\kappa}}) \right], \quad (3.35)$$

which agrees with Eq. (3.10) of Ref. [94].

In the three layer model the SH polarization $\mathcal{P}(2\omega)$ is located in layer ℓ , where we evaluate the fundamental field required in Eq. (3.9). We write

$$\mathbf{E}_\ell(\omega) = E_0 \left(\hat{\mathbf{s}} t_s^{v\ell} (1 + r_s^{\ell b}) \hat{\mathbf{s}} + \hat{\mathbf{p}}_{\ell-} t_p^{v\ell} \hat{\mathbf{p}}_{v-} + \hat{\mathbf{p}}_{\ell+} t_p^{v\ell} r_p^{\ell b} \hat{\mathbf{p}}_{v-} \right) \cdot \hat{\mathbf{e}}^{\text{in}} = E_0 \mathbf{e}_\ell^\omega, \quad (3.36)$$

where \mathbf{e}^{in} is the s ($\hat{\mathbf{s}}$) or p ($\hat{\mathbf{p}}_{v-}$) incoming polarization of the fundamental electric field. Above field is composed of the transmitted field and its first reflection from the ℓb interface for s and p polarizations. The fundamental field, once inside the layer ℓ will be multiply reflected at the ℓv and ℓb interfaces, however each reflection will diminish the intensity of the fundamental field, and as the SHG yield goes with the square of this field, the contribution of the subsequent reflections, other than the one considered in Eq. (3.36), could be safely neglected. From Eq. (3.14) we find that

$$\mathbf{e}_\ell^\omega = \left[\hat{\mathbf{s}} t_s^{v\ell} t_s^{\ell b} \hat{\mathbf{s}} + \frac{t_p^{v\ell} t_p^{\ell b}}{n_\ell^2 n_b} (n_b^2 \sin \theta_0 \hat{\mathbf{z}} + n_\ell^2 w_b \hat{\mathbf{\kappa}}) \hat{\mathbf{p}}_{v-} \right] \cdot \hat{\mathbf{e}}^{\text{in}}. \quad (3.37)$$

Again, to touch base with Ref. [94], if we would like to evaluate the fields in the bulk, instead of the layer ℓ , we simply take $n_\ell = n_b$, ($t_{s,p}^{\ell b} = 1$), to obtain

$$\mathbf{e}_b^\omega = \left[\hat{\mathbf{s}} t_s^{vb} \hat{\mathbf{s}} + \frac{t_p^{vb}}{n_b} (\sin \theta_0 \hat{\mathbf{z}} + w_b \hat{\mathbf{\kappa}}) \hat{\mathbf{p}}_{v-} \right] \cdot \hat{\mathbf{e}}^{\text{in}}, \quad (3.38)$$

that is in agreement with Eq. (3.5) of Ref. [94]. Then, we can write Eq. (3.9) as

$$\mathcal{P}(2\omega) = \begin{cases} E_0^2 \chi : \mathbf{e}_\ell^\omega \mathbf{e}_\ell^\omega & (\text{cgs units}) \\ \epsilon_0 E_0^2 \chi : \mathbf{e}_\ell^\omega \mathbf{e}_\ell^\omega & (\text{MKS units}) \end{cases}, \quad (3.39)$$

where E_0 is the intensity of the fundamental electric field. Finally, with above equation we write Eq. (3.33) as

$$E(2\omega) = \frac{2\eta i\omega}{cW_v} \mathbf{e}_\ell^{2\omega} \cdot \chi : \mathbf{e}_\ell^\omega \mathbf{e}_\ell^\omega, \quad (3.40)$$

where $\eta = 2\pi$ for cgs units and $\eta = 1/2$ for MKS units. To ease on the notation, we define

$$\Upsilon_{\text{iO}} \equiv \mathbf{e}_\ell^{2\omega} \cdot \chi : \mathbf{e}_\ell^\omega \mathbf{e}_\ell^\omega, \quad (3.41)$$

where i stands for the incoming polarization of the fundamental electric field given by $\hat{\mathbf{e}}^{\text{in}}$ in Eq. (3.37), and O for the outgoing polarization of the SH electric field given by $\hat{\mathbf{e}}^{\text{out}}$ in Eq. (3.34).

From Eqs. (3.1) and (3.2) we obtain that in the cgs units ($\eta = 2\pi$)

$$\begin{aligned} |E(2\omega)|^2 &= |E_0|^4 \frac{16\pi^2 \omega^2}{c^2 W_v^2} |\Upsilon_{\text{iO}}|^2 \\ \frac{c}{2\pi} |\sqrt{N_v} E(2\omega)|^2 &= \frac{32\pi^3 \omega^2}{c^3 \cos^2 \theta_0} \left| \frac{\sqrt{N_v}}{n_\ell^2} \Upsilon_{\text{iO}} \right|^2 \left(\frac{c}{2\pi} |\sqrt{n_\ell} E_0|^2 \right)^2, \\ I(2\omega) &= \frac{32\pi^3 \omega^2}{c^3 \cos^2 \theta_0} \left| \frac{\sqrt{N_v}}{n_\ell^2} \Upsilon_{\text{iO}} \right|^2 I^2(\omega), \\ \mathcal{R}_{\text{iO}}(2\omega) &= \frac{32\pi^3 \omega^2}{c^3 \cos^2 \theta_0} \left| \frac{1}{n_\ell} \Upsilon_{\text{iO}} \right|^2, \end{aligned} \quad (3.42)$$

and in MKS units ($\eta = 1/2$)

$$\begin{aligned} |E(2\omega)|^2 &= |E_0|^4 \frac{\omega^2}{c^2 W_v^2} |\Upsilon_{\text{iO}}|^2 \\ 2\epsilon_0 c |\sqrt{N_v} E(2\omega)|^2 &= \frac{2\epsilon_0 \omega^2}{c \cos^2 \theta_0} \left| \frac{\sqrt{N_v}}{n_\ell^2} \Upsilon_{\text{iO}} \right|^2 \frac{1}{4\epsilon_0^2 c^2} (2\epsilon_0 c |\sqrt{n_\ell} E_0|^2)^2, \\ I(2\omega) &= \frac{\omega^2}{2\epsilon_0 c^3 \cos^2 \theta_0} \left| \frac{\sqrt{N_v}}{n_\ell^2} \Upsilon_{\text{iO}} \right|^2 I^2(\omega), \\ \mathcal{R}_{\text{iO}}(2\omega) &= \frac{\omega^2}{2\epsilon_0 c^3 \cos^2 \theta_0} \left| \frac{1}{n_\ell} \Upsilon_{\text{iO}} \right|^2, \end{aligned} \quad (3.43)$$

$$\mathcal{R}_{\text{iO}}(2\omega) \begin{cases} \frac{32\pi^3\omega^2}{c^3 \cos^2 \theta_0} \left| \frac{1}{n_\ell} \Upsilon_{\text{iO}} \right|^2 & (\text{cgs units}) \\ \frac{\omega^2}{2\epsilon_0 c^3 \cos^2 \theta_0} \left| \frac{1}{n_\ell} \Upsilon_{\text{iO}} \right|^2 & (\text{MKS units}) \end{cases}, \quad (3.44)$$

as the SHG yield, where $N_v = 1$ and $W_v = \cos \theta_0$. In the MKS unit system χ is given in m^2/V , since it is a surface second order nonlinear susceptibility, and \mathcal{R}_{iO} is given in m^2/W .

tal vez esto al apendice At this point we mention that to recover the results of Ref. [94] which are equivalent of those of Ref. [96], we take $\mathbf{e}_\ell^{2\omega} \rightarrow \mathbf{e}_v^{2\omega}$, $\mathbf{e}_\ell^\omega \rightarrow \mathbf{e}_b^\omega$, and then

$$\mathcal{R}(2\omega) = \frac{32\pi^3\omega^2}{c^3 \cos^2 \theta_0} |\mathbf{e}_v^{2\omega} \cdot \chi : \mathbf{e}_b^\omega \mathbf{e}_b^\omega|^2, \quad (3.45)$$

will give the SHG yield of a nonlinear polarization sheet radiating from vacuum on top of the surface and where the fundamental field is evaluated below the surface that is characterized by $\epsilon_b(\omega)$.

3.2 One SH Reflection

Therefore, the total radiated field at 2ω is

$$\begin{aligned} \mathbf{E}(2\omega) = & E_s(2\omega) \left(\mathbf{T}^{\ell v} + \mathbf{T}^{\ell v} \cdot \mathbf{R}^{\ell b} \right) \cdot \hat{\mathbf{s}} \\ & + E_{p+}(2\omega) \mathbf{T}^{\ell v} \cdot \hat{\mathbf{P}}_{\ell+} + E_{p-}(2\omega) \mathbf{T}^{\ell v} \cdot \mathbf{R}^{\ell b} \cdot \hat{\mathbf{P}}_{\ell-}. \end{aligned}$$

The first term is the transmitted s -polarized field, the second one is the reflected and then transmitted s -polarized field and the third and fourth terms are the equivalent fields for p -polarization. The transmission is from the layer into vacuum, and the reflection between the layer and the bulk. After some simple algebra, we obtain

$$\mathbf{E}(2\omega) = \frac{2\pi i \tilde{\Omega}}{K_\ell} \mathbf{H}_\ell \cdot \mathcal{P}(2\omega), \quad (3.46)$$

where,

$$\mathbf{H}_\ell = \hat{\mathbf{s}} T_s^{\ell v} \left(1 + R_s^{\ell b} \right) \hat{\mathbf{s}} + \hat{\mathbf{P}}_{v+} T_p^{\ell v} \left(\hat{\mathbf{P}}_{\ell+} + R_p^{\ell b} \hat{\mathbf{P}}_{\ell-} \right). \quad (3.47)$$

3.3 \mathcal{R}_{iF} for different polarization cases

We obtain \mathcal{R}_{iF} from Eq. (3.44) for the most commonly used polarizations of incoming and outgoing fields, i.e., $\text{iF} = pP, pS, sP$ or sS . For this, we have

to explicitly expand Υ_{iF} (Eq. (3.41)). First, by substituting Eqs. (3.7) and (3.8) into Eq. (3.34), we obtain

$$\mathbf{e}_\ell^{2\omega, \text{P}} = \frac{T_p^{v\ell}}{N_\ell} (\sin \theta_0 R_p^{M+} \hat{\mathbf{z}} - W_\ell R_p^{M-} \cos \phi \hat{\mathbf{x}} - W_\ell R_p^{M-} \sin \phi \hat{\mathbf{y}}), \quad (3.48)$$

for P ($\hat{\mathbf{e}}^{\text{F}} = \hat{\mathbf{P}}_{v+}$) outgoing polarization, and

$$\mathbf{e}_\ell^{2\omega, \text{S}} = T_s^{v\ell} R_s^{M+} (-\sin \phi \hat{\mathbf{x}} + \cos \phi \hat{\mathbf{y}}). \quad (3.49)$$

for S ($\hat{\mathbf{e}}^{\text{F}} = \hat{\mathbf{s}}$) outgoing polarization. Secondly, using again Eqs. (3.7) and (3.8), but now with Eq. (3.29), we obtain for p incoming polarization ($\hat{\mathbf{e}}^{\text{i}} = \hat{\mathbf{p}}_{v-}$),

$$\begin{aligned} \mathbf{e}_\ell^{\omega, \text{P}} \mathbf{e}_\ell^{\omega, \text{P}} = & \left(\frac{t_p^{v\ell}}{n_\ell} \right)^2 \left((r_p^{M-})^2 w_\ell^2 \cos^2 \phi \hat{\mathbf{x}} \hat{\mathbf{x}} + 2 (r_p^{M-})^2 w_\ell^2 \sin \phi \cos \phi \hat{\mathbf{x}} \hat{\mathbf{y}} + 2 r_p^{M+} r_p^{M-} w_\ell \sin \theta_0 \cos \phi \hat{\mathbf{x}} \hat{\mathbf{z}} \right. \\ & \left. + (r_p^{M-})^2 w_\ell^2 \sin^2 \phi \hat{\mathbf{y}} \hat{\mathbf{y}} + 2 r_p^{M+} r_p^{M-} w_\ell \sin \theta_0 \sin \phi \hat{\mathbf{y}} \hat{\mathbf{z}} + (r_p^{M+})^2 \sin^2 \theta_0 \hat{\mathbf{z}} \hat{\mathbf{z}} \right), \end{aligned} \quad (3.50)$$

and with Eq. (??) for s incoming polarization ($\hat{\mathbf{e}}^{\text{i}} = \hat{\mathbf{s}}$),

$$\mathbf{e}_\ell^{\omega, \text{S}} \mathbf{e}_\ell^{\omega, \text{S}} = \left(t_s^{v\ell} r_s^{M+} \right)^2 (\sin^2 \phi \hat{\mathbf{x}} \hat{\mathbf{x}} + \cos^2 \phi \hat{\mathbf{y}} \hat{\mathbf{y}} - 2 \sin \phi \cos \phi \hat{\mathbf{x}} \hat{\mathbf{y}}). \quad (3.51)$$

So to calculate \mathcal{R}_{iF} , we summarize in Table 3.4 the combination of the equations needed for all four polarization cases. In the following subsections we write down the explicit expressions for Υ_{iF} for the most general case where the surface has no symmetry other than that of noncentrosymmetry. We then develop these expressions for particular cases of the most commonly investigated surfaces, the (111), (100), and (110) crystallographic faces. For ease of writing we split Υ_{iF} as

$$\Upsilon_{\text{iF}} = \Gamma_{\text{iF}} r_{\text{iF}}, \quad (3.52)$$

and in Table 3.1 we list, for each surface, the components of χ different from zero.[\[96, 97\]](#)

3.3.1 \mathcal{R}_{pP}

Per Table 3.4, \mathcal{R}_{pP} requires Eqs. (3.48) and (3.50). After some algebra, we obtain that

$$\Gamma_{pP} = \frac{T_p^{v\ell}}{N_\ell} \left(\frac{t_p^{v\ell}}{n_\ell} \right)^2, \quad (3.53)$$

(111)- C_{3v}	(110)- C_{2v}	(100)- C_{4v}
χ_{zzz}	χ_{zzz}	χ_{zzz}
$\chi_{zxx} = \chi_{zyy}$	$\chi_{zxx} \neq \chi_{zyy}$	$\chi_{zxx} = \chi_{zyy}$
$\chi_{xxz} = \chi_{yyz}$	$\chi_{xxz} \neq \chi_{yyz}$	$\chi_{xxz} = \chi_{yyz}$
$\chi_{xxx} = -\chi_{xyy} = -\chi_{yyx}$		

Table 3.1: Components of χ for the (111), (110) and (100) crystallographic faces, belonging to the C_{3v} , C_{2v} , and C_{4v} , symmetry groups, respectively. For the (111) surface we choose the x and y axes along the $[11\bar{2}]$ and $[\bar{1}\bar{1}0]$ directions, respectively. For the (110) and (100) we consider the y axis perpendicular to the plane of symmetry.[96] We remark that in general $\chi^{(111)} \neq \chi^{(110)} \neq \chi^{(100)}$.

and

$$\begin{aligned}
r_{pP} = & -R_p^{M-} (r_p^{M-})^2 w_\ell^2 W_\ell \cos^3 \phi \chi_{xxx} - 2R_p^{M-} (r_p^{M-})^2 w_\ell^2 W_\ell \sin \phi \cos^2 \phi \chi_{xxy} \\
& - 2R_p^{M-} r_p^{M+} r_p^{M-} w_\ell W_\ell \sin \theta_0 \cos^2 \phi \chi_{xxz} - R_p^{M-} (r_p^{M-})^2 w_\ell^2 W_\ell \sin^2 \phi \cos \phi \chi_{xyy} \\
& - 2R_p^{M-} r_p^{M+} r_p^{M-} w_\ell W_\ell \sin \theta_0 \sin \phi \cos \phi \chi_{xyz} - R_p^{M-} (r_p^{M+})^2 W_\ell \sin^2 \theta_0 \cos \phi \chi_{xzz} \\
& - R_p^{M-} (r_p^{M-})^2 w_\ell^2 W_\ell \sin \phi \cos^2 \phi \chi_{yxx} - 2R_p^{M-} (r_p^{M-})^2 w_\ell^2 W_\ell \sin^2 \phi \cos \phi \chi_{yyx} \\
& - 2R_p^{M-} r_p^{M+} r_p^{M-} w_\ell W_\ell \sin \theta_0 \sin \phi \cos \phi \chi_{yxz} - R_p^{M-} (r_p^{M-})^2 w_\ell^2 W_\ell \sin^3 \phi \chi_{yyy} \\
& - 2R_p^{M-} r_p^{M+} r_p^{M-} w_\ell W_\ell \sin \theta_0 \sin^2 \phi \chi_{yyz} - R_p^{M-} (r_p^{M+})^2 W_\ell \sin^2 \theta_0 \sin \phi \chi_{yzz} \\
& + R_p^{M+} (r_p^{M-})^2 w_\ell^2 \sin \theta_0 \cos^2 \phi \chi_{zxx} + 2R_p^{M+} r_p^{M+} r_p^{M-} w_\ell \sin^2 \theta_0 \cos \phi \chi_{zzx} \\
& + 2R_p^{M+} (r_p^{M-})^2 w_\ell^2 \sin \theta_0 \sin \phi \cos \phi \chi_{zxy} + R_p^{M+} (r_p^{M-})^2 w_\ell^2 \sin \theta_0 \sin^2 \phi \chi_{zyy} \\
& + 2R_p^{M+} r_p^{M+} r_p^{M-} w_\ell \sin^2 \theta_0 \sin \phi \chi_{zzy} + R_p^{M+} (r_p^{M+})^2 \sin^3 \theta_0 \chi_{zzz},
\end{aligned} \tag{3.54}$$

Case	$\hat{\mathbf{e}}^{\text{F}}$	$\hat{\mathbf{e}}^{\text{i}}$	$\mathbf{e}_\ell^{2\omega, \text{F}}$	$\mathbf{e}_\ell^{\omega, \text{i}} \mathbf{e}_\ell^{\omega, \text{i}}$
\mathcal{R}_{pP}	$\hat{\mathbf{P}}_{v+}$	$\hat{\mathbf{p}}_{v-}$	Eq. (3.48)	Eq. (3.50)
\mathcal{R}_{pS}	$\hat{\mathbf{S}}$	$\hat{\mathbf{p}}_{v-}$	Eq. (3.49)	Eq. (3.50)
\mathcal{R}_{sP}	$\hat{\mathbf{P}}_{v+}$	$\hat{\mathbf{s}}$	Eq. (3.48)	Eq. (3.51)
\mathcal{R}_{sS}	$\hat{\mathbf{S}}$	$\hat{\mathbf{s}}$	Eq. (3.49)	Eq. (3.51)

Table 3.2: Polarization unit vectors for $\hat{\mathbf{e}}^{\text{F}}$ and $\hat{\mathbf{e}}^{\text{i}}$, and equations describing $\mathbf{e}_\ell^{2\omega, \text{F}}$ and $\mathbf{e}_\ell^{\omega, \text{i}} \mathbf{e}_\ell^{\omega, \text{i}}$ for each polarization case.

where all 18 independent components of χ valid for a surface with no symmetries contribute to \mathcal{R}_{pP} . Recall that $\chi_{ijk} = \chi_{ikj}$. Using Table 3.1, we present the expressions for each of the three surfaces being considered here. For the (111) surface we obtain

$$r_{pP}^{(111)} = R_p^{M+} \sin \theta_0 \left((r_p^{M+})^2 \sin^2 \theta_0 \chi_{zzz} + (r_p^{M-})^2 w_\ell^2 \chi_{zxx} \right) - R_p^{M-} w_\ell W_\ell \left(2r_p^{M+} r_p^{M-} \sin \theta_0 \chi_{xxz} + (r_p^{M-})^2 w_\ell \chi_{xxx} \cos 3\phi \right), \quad (3.55)$$

where the three-fold azimuthal symmetry of the SHG signal, typical of the C_{3v} symmetry group, is seen in the 3ϕ argument of the cosine function. For the (110) we have that

$$r_{pP}^{(110)} = R_p^{M+} \sin \theta_0 \left((r_p^{M+})^2 \sin^2 \theta_0 \chi_{zzz} + (r_p^{M-})^2 w_\ell^2 \left(\frac{\chi_{zyy} + \chi_{zxx}}{2} + \frac{\chi_{zyy} - \chi_{zxx}}{2} \cos 2\phi \right) \right) - 2R_p^{M-} r_p^{M+} r_p^{M-} w_\ell W_\ell \sin \theta_0 \left(\frac{\chi_{yyz} + \chi_{xxz}}{2} + \frac{\chi_{yyz} - \chi_{xxz}}{2} \cos 2\phi \right). \quad (3.56)$$

The two-fold azimuthal symmetry of the SHG signal, typical of the C_{2v} symmetry group, is seen in the 2ϕ argument of the cosine function. For the (100) surface we simply make $\chi_{zxx} = \chi_{zyy}$ and $\chi_{xxz} = \chi_{yyz}$, as seen from Table 3.1, and above expression reduces to

$$r_{pP}^{(100)} = R_p^{M+} \sin \theta_0 \left((r_p^{M+})^2 \sin^2 \theta_0 \chi_{zzz} + (r_p^{M-})^2 w_\ell^2 \chi_{zxx} \right) - 2R_p^{M-} r_p^{M+} r_p^{M-} w_\ell W_\ell \sin \theta_0 \chi_{xxz}. \quad (3.57)$$

where we mention that the azimuthal 4ϕ symmetry for the C_{4v} group of the (100) surface is absent in above expression since such contribution is only related to the bulk nonlinear quadrupolar SH term,[96] that is neglected in this work.

3.3.2 \mathcal{R}_{pS}

Per Table 3.4, \mathcal{R}_{pS} requires Eqs. (3.49) and (3.50). After some algebra, we obtain that

$$\Gamma_{pS} = T_s^{v\ell} R_s^{M+} \left(\frac{t_p^{v\ell}}{n_\ell} \right)^2, \quad (3.58)$$

and

$$\begin{aligned}
 r_{pS} = & - (r_p^{M-})^2 w_\ell^2 \sin \phi \cos^2 \phi \chi_{xxx} - 2 (r_p^{M-})^2 w_\ell^2 \sin^2 \phi \cos \phi \chi_{xxy} - 2 r_p^{M+} r_p^{M-} w_\ell \sin \theta_0 \sin \phi \cos \phi \chi_{xxz} \\
 & - (r_p^{M-})^2 w_\ell^2 \sin^3 \phi \chi_{xyy} - 2 r_p^{M+} r_p^{M-} w_\ell \sin \theta_0 \sin^2 \phi \chi_{xzy} - (r_p^{M+})^2 \sin^2 \theta_0 \sin \phi \chi_{xzz} \\
 & + (r_p^{M-})^2 w_\ell^2 \cos^3 \phi \chi_{yxx} + 2 (r_p^{M-})^2 w_\ell^2 \sin \phi \cos^2 \phi \chi_{yyx} + 2 r_p^{M+} r_p^{M-} w_\ell \sin \theta_0 \cos^2 \phi \chi_{yxz} \\
 & + (r_p^{M-})^2 w_\ell^2 \sin^2 \phi \cos \phi \chi_{yyy} + 2 r_p^{M+} r_p^{M-} w_\ell \sin \theta_0 \sin \phi \cos \phi \chi_{yzy} + (r_p^{M+})^2 \sin^2 \theta_0 \cos \phi \chi_{yzz}.
 \end{aligned} \tag{3.59}$$

In this case 12 out of the 18 components of χ valid for a surface with no symmetries, contribute to \mathcal{R}_{pS} . This is so, because there is no \mathcal{P}_z component, as the outgoing polarization is S . From Table 3.1 we obtain,

$$r_{pS}^{(111)} = - (r_p^{M-})^2 w_\ell^2 \chi_{xxx} \sin 3\phi, \tag{3.60}$$

for the (111) surface,

$$r_{sP}^{(110)} = r_p^{M+} r_p^{M-} w_\ell \sin \theta_0 (\chi_{yyz} - \chi_{xxz}) \sin 2\phi, \tag{3.61}$$

for the (110) surface, finally,

$$r_{pS}^{(100)} = 0, \tag{3.62}$$

for the (100) surface, where again, the zero value is only surface related as we neglect the bulk nonlinear quadrupolar contribution.

3.3.3 \mathcal{R}_{sP}

Per Table 3.4, \mathcal{R}_{sP} requires Eqs. (3.48) and (3.51). After some algebra, we obtain that

$$\Gamma_{sP} = \frac{T_p^{v\ell}}{N_\ell} \left(t_s^{v\ell} r_s^{M+} \right)^2, \tag{3.63}$$

and

$$\begin{aligned}
 r_{sP} = & R_p^{M-} W_\ell \left(-\sin^2 \phi \cos \phi \chi_{xxx} + 2 \sin \phi \cos^2 \phi \chi_{xxy} - \cos^3 \phi \chi_{xyy} \right) \\
 & R_p^{M-} W_\ell \left(-\sin^3 \phi \chi_{yxx} + 2 \sin^2 \phi \cos \phi \chi_{yyx} - \sin \phi \cos^2 \phi \chi_{yyy} \right) \\
 & R_p^{M+} \sin \theta_0 \left(\sin^2 \phi \chi_{zxx} - 2 \sin \phi \cos \phi \chi_{zxy} + \cos^2 \phi \chi_{zyy} \right).
 \end{aligned} \tag{3.64}$$

In this case 9 out of the 18 components of $\chi(2\omega)$ valid for a surface with no symmetries, contribute to \mathcal{R}_{sP} . This is so, because there is no $E_z(\omega)$ component, as the incoming polarization is s . From Table 3.1 we get,

$$r_{sP}^{(111)} = R_p^{M+} \sin \theta_0 \chi_{zxx} + R_p^{M-} W_\ell \chi_{xxx} \cos 3\phi, \tag{3.65}$$

for the (111) surface,

$$r_{sP}^{(110)} = R_p^{M+} \sin \theta_0 \left(\frac{\chi_{zxx} + \chi_{zyy}}{2} + \frac{\chi_{zyy} - \chi_{zxx}}{2} \cos 2\phi \right), \quad (3.66)$$

for the (110) surface, and

$$r_{sP}^{(100)} = R_p^{M+} \sin \theta_0 \chi_{zxx}, \quad (3.67)$$

for the (100) surface.

3.3.4 \mathcal{R}_{sS}

Per Table 3.4, \mathcal{R}_{sS} requires Eqs. (3.49) and (3.51). After some algebra, we obtain that

$$\Gamma_{sS} = T_s^{v\ell} R_s^{M+} \left(t_s^{v\ell} r_s^{M+} \right)^2, \quad (3.68)$$

and

$$\begin{aligned} r_{sS} = & -\sin^3 \phi \chi_{xxx} + 2 \sin^2 \phi \cos \phi \chi_{xxy} - \sin \phi \cos^2 \phi \chi_{xyy} \\ & + \sin^2 \phi \cos \phi \chi_{yxx} + \cos^3 \phi \chi_{yyy} - 2 \sin \phi \cos^2 \phi \chi_{yxy}. \end{aligned} \quad (3.69)$$

In this case 6 out of the 18 components of $\chi(2\omega)$ valid for a surface with no symmetries, contribute to \mathcal{R}_{sS} . This is so, because there is neither an $E_z(\omega)$ component, as the incoming polarization is s , nor a \sqrt{z} component, as the outgoing polarization is S . From Table 3.1, we get

$$r_{sS}^{(111)} = \chi_{xxx} \sin 3\phi, \quad (3.70)$$

for the (111) surface,

$$r_{sS}^{(110)} = 0, \quad (3.71)$$

and

$$r_{sS}^{(100)} = 0, \quad (3.72)$$

for the (110) and (100) surfaces, respectively, both being zero as the bulk nonlinear quadrupolar contribution is not considered here.

3.4 Different scenarios

In this section we present five different scenarios, alternative to the three-layer model presented above, for the placement of the nonlinear polarization $\mathcal{P}(2\omega)$ and the fundamental electric field $\mathbf{E}(\omega)$. In these scenarios we neglect the SH multiple reflections contained in $R_l^{M\pm}$ through R_l^M , Eq. (3.32) and (3.23), respectively, for which we take $R_l^M \rightarrow R_l^{\ell b}$. This is equivalent of taking only one single reflection from the ℓb interface. Within the three-layer model we neglect multiple reflections, as yet another scenario, by the same $R_l^M \rightarrow R_l^{\ell b}$ replacement in the formulae shown in the previous section. In what follows, we confine ourselves only to the the (111) surface and the pP combination of incoming-outgoing polarizations, since this is the case where the proposed scenarios differ the most. However, the other pS , sP and sS polarization cases, and (100) and (110) surfaces could be worked out along the same lines described below. For all the scenarios we have that the omission of multiple SH reflections by taking $R_p^{M\pm} \rightarrow 1 \pm R_p^{\ell b}$ (Eq. (3.32)) reduces to

$$\begin{aligned} R_p^{M+} &\rightarrow \frac{N_b}{N_\ell} T_p^{\ell b} \\ R_p^{M-} &\rightarrow \frac{N_\ell}{N_b} \frac{W_b}{W_\ell} T_p^{\ell b}, \end{aligned} \quad (3.73)$$

after using the expressions in Eq. (3.14).

3.4.1 Three layer model: without multiple reflections

Using Eq. (3.73) in Eq. (3.55) we obtain

$$\Gamma_{pP} = \frac{T_p^{\ell v} T_p^{\ell b}}{N_\ell^2 N_b} \left(\frac{t_p^{v\ell} t_p^{\ell b}}{n_\ell^2 n_b} \right)^2, \quad (3.74)$$

and

$$r_{pP}^{(111)} = N_b^2 \sin \theta_0 \left(n_b^4 \sin^2 \theta_0 \chi_{zzz} + n_\ell^4 w_b^2 \chi_{zxx} \right) - N_\ell^2 n_\ell^2 w_b W_b \left(2n_b^2 \sin \theta_0 \chi_{xxz} + n_\ell^2 w_b \chi_{xxx} \cos(3\phi) \right). \quad (3.75)$$

Now that we have neglected multiple SH reflections, we can use above two expressions for Γ_{pP} and r_{pP} to obtain the following four scenarios, by using the choices as described in each subsection bellow. We mention that by neglecting the multiple reflections the thickness d of layer ℓ disappears from the formulation, and the location of the nonlinear polarization sheet $\mathbf{P}(\mathbf{r}, t)$ (Eq. (3.3)) at d_2 (see Fig. ??), is inmaterial.

3.4.2 Two layer model

Historically, this is the model most used in the literature, and our three-layer model with multiple reflections, as mentioned in the introduction, is a clear improvement upon the simple two layer model. In the two layer model, one considers that $\mathcal{P}(2\omega)$, is evaluated in the vacuum region, while the fundamental fields are evaluated in the bulk region.[96, 94] To do this, we take the 2ω radiations factors for vacuum by taking $\ell = v$, thus $\epsilon_\ell(2\omega) = 1$, $T_p^{\ell v} = 1$, $T_p^{\ell b} = T_p^{vb}$, and the fundamental field inside medium b by taking $\ell = b$, thus $\epsilon_\ell(\omega) = \epsilon_b(\omega)$, $t_p^{v\ell} = t_p^{vb}$, and $t_p^{\ell b} = 1$. With these choices Eqs. (3.74) and (3.75) reduce to

$$\Gamma_{pP} = \frac{T_p^{vb}(t_p^{vb})^2}{n_b^2 N_b}, \quad (3.76)$$

and

$$r_{pP}^{(111)} = N_b^2 \sin \theta_0 \left(\sin^2 \theta_0 \chi_{zzz} + w_b^2 \chi_{zxx} \right) - w_b W_b \left(2 \sin \theta_0 \chi_{xxz} + w_b \chi_{xxx} \cos(3\phi) \right), \quad (3.77)$$

and these expressions are in agreement with Refs. [96] and [94].

3.4.3 Taking the nonlinear polarization and the fundamental fields in the bulk

We follow the same procedure as above considering that both the 2ω and 1ω terms will be evaluated in the bulk taking $\ell = b$, thus $\epsilon_\ell(2\omega) = \epsilon_b(2\omega)$, $T_p^{v\ell} = T_p^{vb}$, $T_p^{\ell b} = 1$, and $\epsilon_\ell(\omega) = \epsilon_b(\omega)$, $t_p^{v\ell} = t_p^{vb}$, and $t_p^{\ell b} = 1$. With these choices Eqs. (3.74) and (3.75) reduce to

$$\Gamma_{pP} = \frac{T_p^{vb}(t_p^{vb})^2}{n_b^2 N_b}, \quad (3.78)$$

and

$$r_{pP}^{(111)} = \sin^3 \theta_0 \chi_{zzz} + w_b^2 \sin \theta_0 \chi_{zxx} - 2w_b W_b \sin \theta_0 \chi_{xxz} - w_b^2 W_b \chi_{xxx} \cos 3\phi. \quad (3.79)$$

3.4.4 Taking the nonlinear polarization in ℓ and the fundamental fields in the bulk

Again, we follow the same procedure as above considering that 2ω terms are evaluated in the thin layer ℓ , and the 1ω terms will be evaluated in the

Label	$\mathcal{P}(2\omega)$	$\mathbf{E}(\omega)$
Three layer	ℓ	ℓ
Two layer	v	b
<i>Bulk</i>	b	b
<i>Hybrid</i>	ℓ	b
<i>Vacuum</i>	v	v

Table 3.3: Summary of SSHG yield models. “Label” is the name used in subsequent figures, while the remaining columns show in which medium we will consider the specified quantity. ℓ is the thin layer below the surface of the material, v is the vacuum region, and b is the bulk region of the material.

bulk by taking $\ell = b$, thus $\epsilon_\ell(\omega) = \epsilon_b(\omega)$, $t_p^{\ell\ell} = t_p^{vb}$, and $t_p^{\ell b} = 1$. With these choices Eqs. (3.74) and (3.75) reduce to

$$\Gamma_{pP}^{\ell b} = \frac{T_p^{v\ell} T_p^{\ell b} (t_p^{vb})^2}{N_\ell^2 n_b^2 N_b}, \quad (3.80)$$

and

$$r_{pP}^{(111)} = N_b^2 \sin^3 \theta_0 \chi_{zzz} + N_b^2 k_b^2 \sin \theta_0 \chi_{zxx} - 2N_\ell^2 w_b W_b \sin \theta_0 \chi_{xxz} - N_\ell^2 w_b^2 W_b \chi_{xxx} \cos 3\phi. \quad (3.81)$$

3.4.5 Taking the nonlinear polarization and the fundamental fields in the vacuum

Our last scenario considers both the $\mathcal{P}(2\omega)$ and fundamental fields evaluated in the vacuum. We take $\ell = v$, thus $\epsilon_\ell(2\omega) = 1$, $T_p^{\ell v} = 1$, $T_p^{\ell b} = T_p^{vb}$, and $\epsilon_\ell(\omega) = 1$, $t_p^{v\ell} = 1$, and $t_p^{\ell b} = t_p^{vb}$. With these choices Eqs. (3.74) and (3.75) reduce to

$$\Gamma_{pP} = \frac{T_p^{vb} (t_p^{vb})^2}{n_b^2 N_b}, \quad (3.82)$$

and

$$r_{pP}^{(111)} = n_b^4 N_b^2 \sin^3 \theta_0 \chi_{zzz} + N_b^2 w_b^2 \sin \theta_0 \chi_{zxx} - 2n_b^2 w_b W_b \sin \theta_0 \chi_{xxz} - w_b^2 W_b \chi_{xxx} \cos 3\phi. \quad (3.83)$$

We summarize all these scenarios in Table 3.3 for quick reference.

3.4.6 Summary

We present the final expressions for each polarization case in Table 3.4.

iF	Γ_{iF}^ℓ	r_{iF}^ℓ
pP	$\frac{T_p^{v\ell}}{N_\ell} \left(\frac{t_p^{v\ell} t_p^{\ell b}}{n_\ell^2 n_b} \right)^2$	$R_p^{M+} \sin \theta_0 (n_b^4 \sin^2 \theta_0 \chi_{zzz} + n_\ell^4 w_b^2 \chi_{zxx})$ $- R_p^{M-} n_\ell^2 w_b W_\ell (2n_b^2 \sin \theta_0 \chi_{xxz}$ $+ n_\ell^2 w_b \chi_{xxx} \cos 3\phi)$
pS	$T_s^{v\ell} R_s^{M+} \left(\frac{t_p^{v\ell} t_p^{\ell b}}{n_\ell^2 n_b} \right)^2$	$- n_\ell^4 w_b^2 \chi_{xxx} \sin 3\phi$
sP	$\frac{T_p^{v\ell}}{N_\ell} (t_s^{v\ell} t_s^{\ell b})^2$	$R_p^{M+} \sin \theta_0 \chi_{zxx} + R_p^{M-} W_\ell \chi_{xxx} \cos 3\phi$
sS	$T_s^{v\ell} R_s^{M+} (t_s^{v\ell} t_s^{\ell b})^2$	$\chi_{xxx} \sin 3\phi$

Table 3.4: The expressions needed to calculate the SHG yield for the (111) surface, for each polarization case.

CHAPTER 4

RESULTS

4.1 Chi2

In this section we present a relevant test case to check the consistency of our approach. We have selected a clean Si(001) surface with a 2×1 surface reconstruction. The slab for such a surface could be chosen to be centrosymmetric by creating the front and back surfaces with the same 2×1 reconstruction. However, we choose to terminate one of the surfaces with hydrogen producing an ideal terminated bulk Si surface. The H atoms simply saturate the dangling bonds of the bulk-like Si atoms at the surface, as seen in Fig. 4.1. We take the z coordinate pointing out of the surface and the x coordinate along the crystallographic [011] direction is parallel to the dimmers. The idea behind this slab configuration is that the cristalline symmetry of the H terminated surface imposes that $\chi_{\text{H}}^{xxx} = 0$. The 2×1 surface has no such restrictions, so $\chi_{2 \times 1}^{xxx} \neq 0$. This is due to the fact that along the y direction there is a mirror plane for the H-saturated surface, whereas for the 2×1 surface this mirror is lost as the dimers are asymmetric along x . Thus, calculating χ^{xxx} for the full-slab, or the half-slab containing the 2×1 surface[98] should yield the same result since the contribution from the H saturated surface is zero regardless. We must check that the following relationship is satisfied for this particular slab

$$\chi_{\text{half-slab}}^{xxx}(-2\omega; \omega, \omega) = \chi_{\text{full-slab}}^{xxx}(-2\omega; \omega, \omega),$$

where $\chi_{\text{half-slab}}^{xxx}(-2\omega; \omega, \omega)$ is calculated using $\mathcal{C}(z) = 1$ from the upper half containing the 2×1 surface reconstruction, as seen in Fig. 4.1, and $\chi_{\text{full-slab}}^{xxx}(-2\omega; \omega, \omega)$ is calculated using $\mathcal{C}(z) = 1$ through the full slab. We show the results for this comparison in the remainder of this section. Also, we checked that for the dihydride surface $\chi_{\text{half-slab}}^{xxx}(-2\omega; \omega, \omega) = 0$.

The self-consistent ground state and the Kohn-Sham states were calculated in the DFT-LDA framework using the plane-wave ABINIT code.[99] We used Troullier-Martins pseudopotentials[100] that are fully separable nonlocal pseudopotentials in the Kleinman-Bylander form.[80] The contribution of \mathbf{v}^{nl} and \mathbf{V}^{nl} to Eq. (3.1) is carried out using the DP code.[101] The

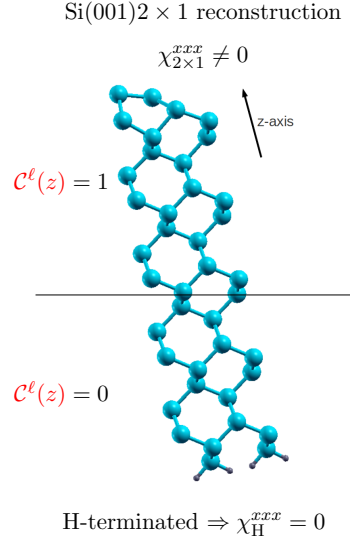


Figure 4.1: (color on line) The slab shows a clean Si(001) 2×1 front surface with an ideal terminated Si bulk back surface. The dangling bonds are H (small balls) saturated. This image depicts 12 Si atomic layers with one H atomic layer.

surfaces have been studied with the experimental lattice constant of 5.43 Å. Structural optimizations were performed with the ABINIT code.[99] The geometry optimization has been carried out in slabs of 12 atomic layers where the central four layers were fixed at the bulk positions. The structures were relaxed until the Cartesian force components were less than 5 meV/Å. The geometry optimization for the clean surface gives a dimer buckling of 0.721 Å, and a dimer length of 2.301 Å. For the Si(001) 1×1 :2H dihydride surface, we have obtained a Si-H bond distance of 1.48 Å. This results are in good agreement with previous theoretical studies.[102, 87] The vacuum size is equivalent to one quarter the size of the slab, avoiding the effects produced by possible wave-function tunneling from the contiguous surfaces of the full crystal formed by the repeated super-cell scheme.[87]

Spin-orbit, local field, and electron-hole attraction[103] effects on the SHG process are all neglected. Although these are important factors in the optical response of a semiconductor, their efficient calculation is still theoretically and numerically challenging and under debate. This merits further study but is beyond the scope of this paper. For a given slab size, we find the converged spectra to obtain the relevant parameters. The most important

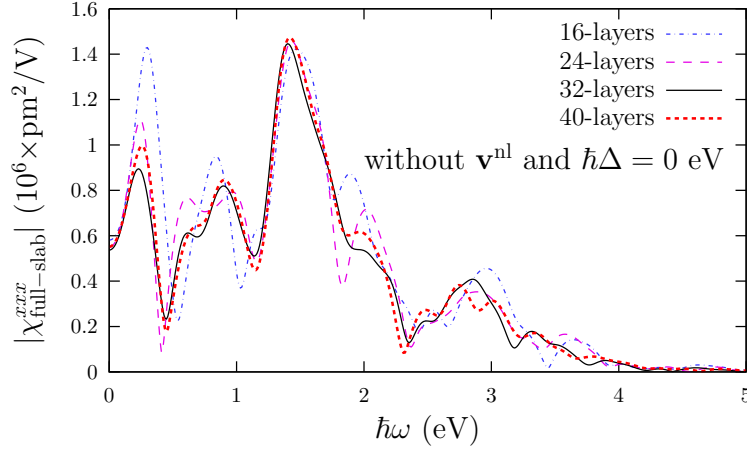


Figure 4.2: (color on line) $|\chi_{\text{half-slab}}^{xxx}|$ vs $\hbar\omega$ for the slab with 16, 24, 32, and 40 atomic Si layers. The front surface is in a clean 2×1 reconstruction and the back surface is an ideal terminated bulk H-saturated dangling bonds (see Fig. 4.1).

of these are: an energy cut-off of 10 Ha for the 16, 24, and 32 layered slabs and 13 Ha for the 40 layer slab, an equal number of conduction and valence bands, and a set of 244 \mathbf{k} -points. The \mathbf{k} -points are used for the linear analytic tetrahedron method for evaluating the 3D Brillouin Zone (BZ) integrals where special care was taken to examine the double resonances of Eq. (3.1). [104] Note that the Brillouin zone for the slab geometry collapses to a 2D-zone, with only one \mathbf{k} -point along the z -axis. All spectra were calculated with a Gaussian smearing of 0.15 eV.

We must evaluate $T_{nm}^{\text{ab}} = (i/\hbar)[r^{\text{b}}, v^{\text{nl,a}}]_{nm}$ in order to obtain Eqs. (2.87) and (??) that are required for Eq. (3.1). Computing second-order derivatives is required thus making the numerical procedure very time consuming. This adds significantly to the already lengthy time needed for the calculation of the \mathbf{v}^{nl} contribution that is proportional only to the first order derivatives. Memory requirements are also increased for both \mathbf{v}^{nl} and $[\mathbf{r}, \mathbf{v}^{\text{nl}}]$. However, the contribution from $[\mathbf{r}, \mathbf{v}^{\text{nl}}]$ is very small[90] and therefore we neglect it in this work.

4.1.1 Full-slab results

In Fig. 4.2 we show $|\chi_{\text{full-slab}}^{xxx}|$ for the slab with 16, 24, 32, and 40 Si atomic layers, without the contribution of \mathbf{v}^{nl} and with no scissors correction. Since

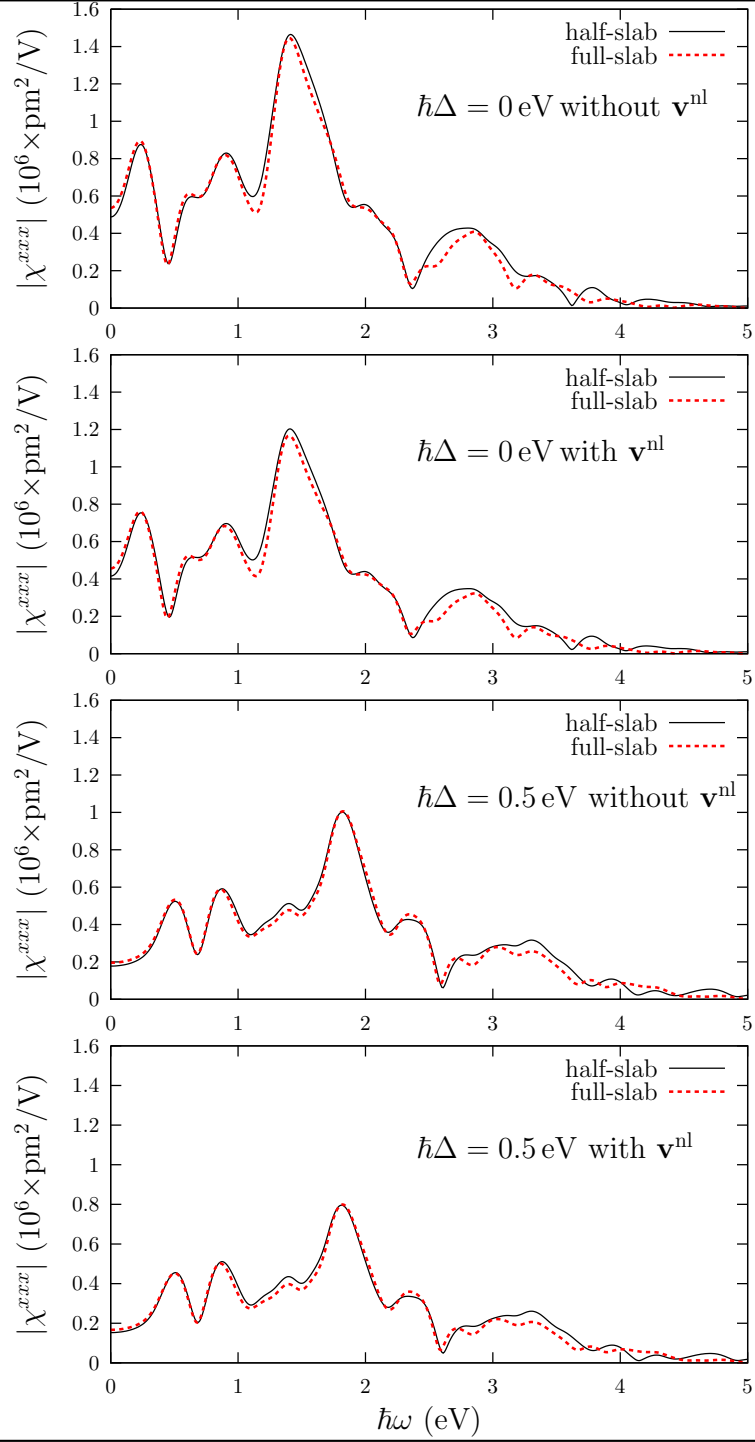


Figure 4.3: (color on line) $\chi_{\text{half-slab}}^{xxx}$ and $\chi_{\text{full-slab}}^{xxx}$ vs $\hbar\omega$ for a slab with 32 atomic Si layers plus one H layer.

the clean Si(001) surface is 2×1 , there are two atoms per atomic layer, thus the total number of atoms per slab is twice the number of atomic layers of the slab. In making the slabs larger, we add steps of 8 layers of bulk-like atomic positions. We note that the response differs substantially for 16 and 24 layers but is quite similar for 32 and 40 layers. As explained above, the calculation of the \mathbf{v}^{nl} contribution is computationally expensive. A good compromise between the accuracy in the convergence of $\chi_{\text{full-slab}}^{\text{xxx}}$ as a function of the number of layers in the slab, and the computational expense is to consider the slab with 32 Si atomic layers as an accurate representation of our system.

4.1.2 Half-slab vs. full-slab

In Fig. 4.3 we compare $\chi_{\text{half-slab}}^{\text{xxx}}$ vs. $\chi_{\text{full-slab}}^{\text{xxx}}$ for the four different possibilities between including or not including the effects of \mathbf{v}^{nl} or the scissors correction $\hbar\Delta$. For these results we chose $\hbar\Delta = 0.5$ eV, that is the GW gap reported in Refs. [105, 106]. This is justified by the fact that the surface states of the clean Si(001) surface are rigidly shifted and maintain their dispersion relation with respect to LDA according to the GW calculations of Ref. [105]. We see that for all four instances the difference between responses is quite small. Indeed, when the value $|\chi^{\text{xxx}}|$ is large the difference between the two is very small; when the value is small the difference increases only slightly, but the spectra is so close to zero that it is negligible. These differences would decrease as the number of atomic layers increases. We remark that 32 layers in the slab is more than enough to confirm that the extraction of the surface second-harmonic susceptibility from the 2×1 surface is readily possible using the formalism contained in Eq. (3.1). We have confirmed that for the dihydride surface $|\chi_{\text{half-slab}}^{\text{xxx}}| \approx 0$ (not shown). This confirms the validity of our theory and is the main result of this article; through the proposed layer formalism we can calculate the surface SH $\chi^{\text{abc}}(-2\omega; \omega, \omega)$ including the contribution of the nonlocal part of the pseudopotentials and the part of the many-body effects through the scissors correction. Our scheme should work for any slab.

4.1.3 Results for $\chi_{2 \times 1}^{\text{xxx}}(-2\omega; \omega, \omega)$

We proceed to explain some of the features seen in $|\chi_{2 \times 1}^{\text{xxx}}|$ that, as explained above, are obtained by calculating $|\chi_{\text{half-slab}}^{\text{xxx}}|$. First, from Fig. 4.3 we note a series of resonances that derive from 1ω and 2ω terms in Eq. (3.1). Notice that the 2ω resonances start below $E_g/2$ where E_g is the band gap (0.53 eV

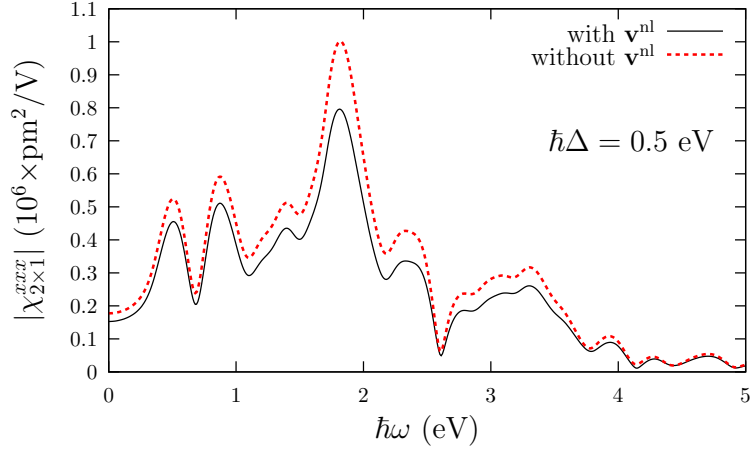


Figure 4.4: (color on line) $\chi_{2\times 1}^{xxx}$ vs $\hbar\omega$ for a slab with 32 atomic Si layers plus one H layer, with and without the contribution from \mathbf{v}^{nl} .

for LDA and 1.03 eV if the scissor is used with $\hbar\Delta = 0.5$ eV). These resonances come from the electronic states of the 2×1 surface, that lie inside the bulk band gap of Si and are the well known electronic surface states.[105] In Fig. 4.4 we see that the effect of \mathbf{v}^{nl} reduces the value of $|\chi_{2\times 1}^{xxx}|$ by 15-20% showing the importance of this contribution for a correct calculation of SSHG, in agreement with the analysis for bulk semiconductors.[107] However, the inclusion of \mathbf{v}^{nl} does not changes the spectral shape of $|\chi_{2\times 1}^{xxx}|$; this also can be confirmed from the cases of zero scissors correction from Fig. 4.3.

To see the effect of the scissors correction, we take two different finite values for $\hbar\Delta$. The first one with a value of $\hbar\Delta = 0.5$ eV, used in the above results, is the “average” GW gap taken from Ref. [105] that is in agreement with Ref. [106]. The second one with a value of $\hbar\Delta = 0.63$ eV is the “average” gap taken from Ref. [108], where more \mathbf{k} -points in the Brillouin zone were used to calculate its GW value. From Fig. 4.5 we note that the scissors correction shifts the spectra from its LDA value to higher energies as expected. However, contrary to the case of linear optics[109] the shift introduced by the scissors correction is not rigid, as pointed out in Ref. [104]. This is because the second-harmonic optical response mixes 1ω and 2ω transitions (see Eq. (3.1)), and accounts for the non-rigid shift. The reduction of the spectral strength is in agreement with previous calculations for bulk systems.[104, 110, 111] When we compare $|\chi_{2\times 1}^{xxx}|$ for the two finite values of $\hbar\Delta$, we see that the first two peaks are

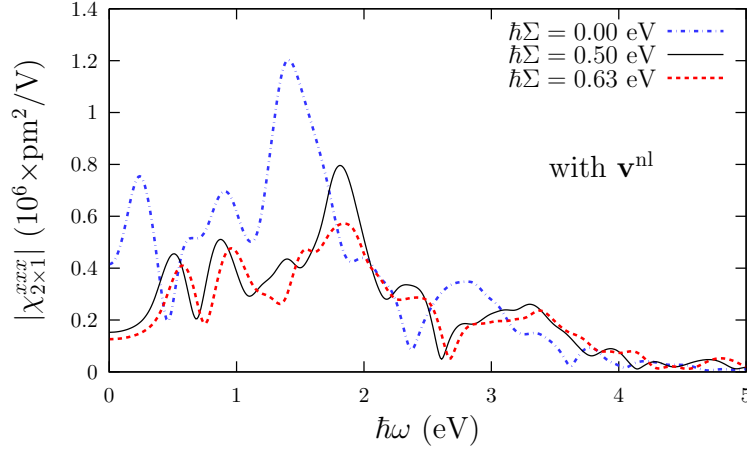


Figure 4.5: (color on line) $\chi_{2\times 1}^{xxx}$ vs $\hbar\omega$ for a slab with 32 atomic Si layers plus one H layer, for two different values of the scissors correction $\hbar\Delta$.

almost rigidly shifted with a small difference in height while the rest of the peaks are modified substantially. This behavior comes from the fact that the first two peaks are almost exclusively related to the 2ω resonances of Eq. (3.1). The other peaks are a combination of 1ω and 2ω resonances and yield a more varied spectrum. We mention that for large gap materials, the 1ω and 2ω would be split showing a small interference effect, but still the 2ω would strongly depend on the surface states. This way we see that small changes in the value of the scissors shift can in general affect the SSH susceptibility spectrum quite dramatically. In Ref. [112], the authors already remarked that nonlinear optical response of bulk materials is more influenced by the electronic structure of the material than the linear case. In the case of semiconducting surfaces the problem is even more intricate due to the presence of electronic surface states. The high sensitivity of SSHG to the energy position of surface states, as seen in Fig. 4.5, makes SSHG a good benchmark spectroscopical tool for testing the validity of the inclusion of many-body effects, and in particular the quasi-particle correction to the electronic states.

Although local fields are neglected they should, in principle, be small parallel to the interface as the electric field is continuous. So, we would expect that the xxx component of $\chi(-2\omega; \omega, \omega)$ would have a small influence from the local fields. Also, the excitonic effects ought to be explored, but their efficient calculation is theoretically and numerically challenging[103] and beyond the scope of this article. Unfortunately the experimental mea-

surement of the xxx component of $\chi(-2\omega; \omega, \omega)$ is not possible as the SH radiated intensity would be proportional not only to this component but also to the other components of $\chi(-2\omega; \omega, \omega)$. However, in a forthcoming publication we will present a study of SSHG from several Si surfaces with comparison to experimental results.

4.2 SHG Yield

4.3 Method

We constructed the Si(111)(1×1):H surface with the experimental lattice constant of 5.43 Å, and then performed structural optimizations with the ABINIT[113, 99] code. The structures were relaxed until the Cartesian force components were less than 5 meV/Å, yielding a final Si-H bond distance of 1.50 Å. The energy cutoff used was 20 Ha, and we used Troullier-Martin LDA pseudopotentials.[100] The resulting atomic positions are in good agreement with previous theoretical studies, [114, 115, 116, 117, 118] as well as the experimental value for the Si-H distance.[119]

We also evaluated the number of layers required for convergence and settled on a slab with 48 atomic Si planes. The geometric optimizations mentioned above are therefore carried out on slabs of 48 atomic layers without fixing any atoms to the bulk positions. All of the calculations involve $\epsilon_{\text{half-slab}}^{\text{ab}}$ and $\chi_{\text{half-slab}}^{\text{abc}}$, which are calculated with $\mathcal{C}(z) = 1$ for the upper half of our slab. This encompasses 24 layers of Si and the single layer of H that terminates the top surface. The vacuum size is equivalent to one quarter the size of the slab, avoiding the effects produced by possible wave-function tunneling from the contiguous surfaces of the full crystal formed by the repeated super-cell scheme.[87]

The electronic wave-functions, $\psi_{n\mathbf{k}}(\mathbf{r})$, were also calculated with the ABINIT code using a planewave basis set with an energy cutoff of 15 Hartrees. $\chi^{\text{abc}}(-2\omega; \omega, \omega)$ was properly converged with 576 \mathbf{k} points in the irreducible Brillouin zone, which are equivalent to 1250 \mathbf{k} points if we disregard symmetry relations. The contribution of \mathbf{V}^{nl} in Eq. (??) was carried out using the DP[101] code with a basis set of 3000 planewaves. Convergence for the number of bands was achieved at 200, which includes 97 occupied bands and 103 unoccupied bands.

All spectra were produced using a scissors value of 0.7 eV in the $\chi^{\text{abc}}(-2\omega; \omega, \omega)$ and $\epsilon_{\ell}(\omega)$ calculations. This value was obtained from Ref. [120], in which the authors carry out a G_0W_0 calculation on this surface for increasing num-

bers of layers. They calculated the LDA and G_0W_0 band gaps, and found that the difference between the two tends towards ~ 0.7 eV as more layers are added, culminating in a value of 0.68 eV for bulk Si. This calculation is completely *ab-initio*, so we choose 0.7 eV as a very reasonable value for the scissors correction.

Our method of calculation is as follows. We first calculated $\varepsilon_b(\omega)$, $\varepsilon_\ell(\omega)$, and then $\chi^{\text{abc}}(-2\omega; \omega, \omega)$ from Eq. (??). We used these for the Fresnel factors and in Eqs. (??), (??), and (??), and finally, those into Eq. (??) to obtain the theoretical SHG yield for different polarizations that can then be compared with the experimental data.

4.4 Results

In this section, we present our theoretical results compared with the appropriate experimental data. For full details on these experiments, see Refs. [121, 122, 118, 123]. This analysis provides information on the physics behind the SHG yield and how it is affected by a variety of factors.

4.4.1 Calculating $\chi(-2\omega; \omega, \omega)$ using relaxed atomic positions

The pioneering work presented in Ref. [118] showed the effect of artificially moving the atomic position on the resulting SSHG spectra. In this section, we address the more practical and relevant case of atomic relaxation. More precisely, we compare the fully relaxed structure described in Sec. 4.3 with an unrelaxed structure where all the Si atoms are at the ideal bulk positions. Note that in both cases, the Si-H bond distance is the same 1.5 Å.

We compare the calculated $\chi^{xxx}(-2\omega; \omega, \omega)$ with experimental data for this surface taken from Ref. [121]. This data provides an excellent point of comparison as it was presented in absolute units and was measured at a very low temperature of 80 K. We used both relaxed (as detailed in Sec. 4.3) and unrelaxed atomic positions to calculate the nonlinear susceptibility tensor. The calculation with the unrelaxed coordinates was done with the same parameters mentioned above.

We can see from Fig. 4.6 that the relaxed coordinates have an improved peak position that is very slightly blueshifted with respect to the experimental peak near 1.7 eV. In contrast, the unrelaxed coordinates have a peak that is redshifted close to 0.05 eV from experiment. There is also a feature between 1.5 eV and 1.6 eV that appears in the relaxed spectrum that coincides partially with the experimental data. It is important to note that this data was taken at low temperature (80 K); this further favors the comparison, as

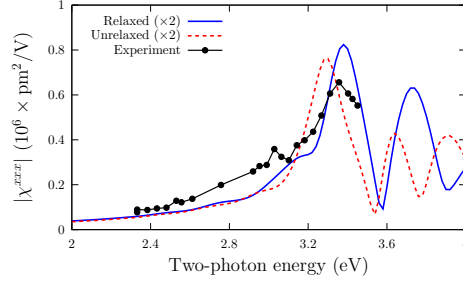


Figure 4.6: (Color online) Comparison of $\chi^{xxx}(-2\omega; \omega, \omega)$ calculated using relaxed and unrelaxed atomic positions, with the experimental data presented in Ref. [121]. Theoretical curves are broadened with $\sigma = 0.05$ eV.

the theory neglects the effects of temperature. We can also see from Ref. [121] that the peaks in the spectrum redshift as the temperature increases. Intensity for both the relaxed and unrelaxed curves are roughly half the intensity of the experimental spectrum. We have converted the units of the experimental data from CGS to MKS units for easier comparison.

Therefore, the most accurate theoretical results are given by using relaxed atomic positions for the calculation of $\chi(-2\omega; \omega, \omega)$. Although this process can be very time consuming for large numbers of atoms, we consider it a crucial step. From a numerical standpoint, this further demonstrates that SSHG is very sensitive to the surface atomic positions. In particular, our results show that a correct value of the Si-H bond length is not enough to obtain the most accurate SSHG spectra, and that a full relaxation of the structure is required. Additionally, experiments that are conducted under very low temperature conditions will also yield improved similarity with theory.

4.4.2 Calculated \mathcal{R}_{pS} compared to experiment

All calculations presented from this point on were done using the relaxed atomic positions described in previous sections. We now move on to the theoretical SHG yield compared with experiment. We first compare the calculated \mathcal{R}_{pS} spectra with room temperature experimental data from Ref. [118]. We adhere to the experimental setup by taking an angle of incidence $\theta = 65^\circ$ and an azimuthal angle of $\phi = 30^\circ$ with respect to the x -axis. This azimuthal angle maximizes r_{pS} , as shown in Eq. (??). In Fig. 4.7, we see that the three layer model accurately reproduces the lineshape of the experimental spectrum which includes the peaks corresponding to both

the E_1 (3.4 eV) and E_2 (4.3 eV) critical points of bulk silicon, and a smaller feature at around 3.8 eV. The calculated E_1 and E_2 peaks are redshifted by 0.1 eV and 0.06 eV, respectively, compared with the experimental peaks. The intensity using this model is very close to that measured in the experiment.

The main issue to address here is the discrepancy between the intensity of the E_1 peak. In the theoretical curves, the peaks differ only slightly in overall intensity. Conversely, the experimental E_1 peak is significantly smaller than the E_2 peak. This may be due to the effects of oxidation on the surface. Ref. [123] features similar data to those of Ref. [118] but focuses on the effects of surface oxidation. We can see that as time passes during the experiment, the surface becomes more oxidized, and the E_1 peak diminishes substantially, as shown by the experimental data taken 5 hours after initial H-termination. This may be enough time to slightly reduce the E_1 peak intensity, as can be observed here.

In Fig. 4.8, we compare the theoretical \mathcal{R}_{pS} with experimental data from Ref. [122]; this data, however, only encompasses the E_1 peaks, and was obtained at room temperature. We consider an angle of incidence $\theta = 45^\circ$ and an azimuthal angle $\phi = 30^\circ$ to match these experimental conditions. As in the previous comparison, the E_1 peak is slightly redshifted compared to experiment. The intensity of the theoretical yield is smaller than the experimental yield for all three models. The measurements presented in Ref. [122] were taken very shortly after the surface had been prepared, and the surface itself was prepared with a high degree of quality and measured at room temperature. Peak position compared to theory is slightly improved under these conditions. As before, the three layer model is closer in intensity to the experimental spectrum.

In both comparisons, the E_1 peak position is slightly redshifted. It is well known that temperature causes shifting in the peak position of SHG spectra.[124] We showed in the previous section that our calculation is closer to low temperature measurements. It is likely that low temperature measurements for the SHG yield will lead to more closely matched results.

Both the two layer and bulk models are identical and roughly 3 times smaller than the experiment. We can see from Eq. (??) that \mathcal{R}_{pS} only has 1ω terms ($\varepsilon_\ell(\omega)$ and k_b). For both of these models, the fundamental fields are evaluated in the bulk, which means that the only change to Eq. (??) is that $\varepsilon_\ell(\omega) \rightarrow \varepsilon_b(\omega)$. Additionally, Γ_{pS}^ℓ also remains identical between the two models and has no 2ω terms in the denominator. Therefore, r_{pS} is identical between these two models. Ultimately, the three layer model best reproduces both the lineshape and the intensity of the experimental spectrum.

Per Eq. (??), the intensity of \mathcal{R}_{pS} depends only on $\chi_{\parallel\parallel\parallel\parallel}$, which is not affected by local field effects.[125] These effects are neglected in this calculation, but \mathcal{R}_{pS} maintains an accurate lineshape and provides a good quantitative description of the experimental SHG yield. We note that both the calculated and experimental spectra show two-photon resonances at the energies corresponding to the critical point transitions of bulk Si. We also see that the SHG yield drops rapidly to zero below E_1 , which is consistent with the absence of surface states due to the H saturation on the surface. This observation holds true for all three polarization cases studied here.

Lastly, in Fig. 4.9 we provide an overview of the different levels of approximation proposed in this article. All curves here were calculated using the three layer model. The long dashed line depicts the effect of excluding the contribution from the nonlocal part of the pseudopotentials. This is consistent with the results reported in Ref. [126], where the exclusion of this term increases the intensity of the components of $\chi(-2\omega; \omega, \omega)$ by approximately 15% to 20%. We also notice that the E_1 peak is larger than the E_2 peak, contrasting with the experiment, where the E_1 peak is smaller than E_2 . Lastly, the thin solid line depicts the full calculation with a scissors value of $\hbar\Delta = 0$. We notice that the spectrum is almost rigidly redshifted as this H-saturated surface has no electronic surface states.[126] Thus, this demonstrates the importance of including the scissors correction to accurately reproduce the experimental spectrum. In summary, the inclusion of the contribution from the nonlocal part of the pseudopotentials and the scissors operator on top of the three layer model gives a much better comparison with the experimental data.

4.4.3 Calculated \mathcal{R}_{sP} compared to experiment

Next, we analyze and compare the calculated \mathcal{R}_{sP} spectra with experimental data from Ref. [118]. We again adhere to the experimental setup by taking an angle of incidence $\theta = 65^\circ$ and an azimuthal angle $\phi = 30^\circ$. From Fig. 4.10, we can immediately appreciate that the overall intensity of \mathcal{R}_{sP} is one order of magnitude lower than \mathcal{R}_{pS} . The experimental data is far noisier than in the other cases but we can still discern the E_1 and E_2 peaks. As with our previous comparisons, the three layer model accurately matches both the intensity and the lineshape of the experimental spectrum. It produces a curve that is very close to the experimental intensity with good proportional heights for the calculated E_1 and E_2 peaks. In contrast, the two layer model is 100 times more intense than experiment and produces an enlarged E_2 peak. The bulk model is ten times smaller with a good lineshape.

The differences between the two layer and bulk models are not derived from Eq. (??), as the $\varepsilon_b(2\omega)$ does not change and the second term vanishes for this azimuthal angle of $\phi = 30$. However, Γ_{sP}^ℓ does cause a significant change in the intensity as there is an $\varepsilon_\ell(2\omega)$ term in the denominator. This will become $\varepsilon_v(2\omega) = 1$ for the two layer model, and $\varepsilon_b(2\omega)$ in the bulk model. This accounts for the significant difference between the intensity of the two models, while the lineshape remains mostly consistent.

At higher energies, the theoretical curve is blueshifted as compared to the experiment. We consider that the likely explanation for this is the inclusion of the scissor operator, which does not adequately correct the transitions occurring at these higher energies. A full GW calculation would be well suited for this task, but is beyond the scope of this paper.

4.4.4 Calculated \mathcal{R}_{pP} compared to experiment

We present \mathcal{R}_{pP} compared to experimental data from Ref. [118] in Fig. 4.11. We note that peak position for the three layer model is similar to experiment with the overall intensity being only two times larger. The E_2 peak is blueshifted by around 0.3 eV, and the yield does not go to zero after 4.75 eV. The two layer model has good lineshape, but it is 40 times more intense than experiment. The calculated E_2 peak is similar, but the E_1 peak lacks the sharpness present in the experiment. The bulk model is very close to the lineshape of the three layer model, but with four times less intensity. From Eq. (??), we see that \mathcal{R}_{pP} has several 2ω terms that will change between models. This will have a deep effect on the lineshape. Coupled to Γ_{pP}^ℓ , which also has $\varepsilon_\ell(2\omega)$ in the denominator, and we have a significant difference in both lineshape and intensity between the two layer and bulk models.

Reviewing Eq. (??), we see that \mathcal{R}_{pP} is by far the most involved calculation, since it includes all four nonzero components. In particular, $\chi_{\perp\perp\perp}$ and $\chi_{\parallel\parallel\perp}$ include out-of-plane incoming fields. These are affected by local field effects that can change both intensity and peak position.[125] Including these effects is computationally very expensive and is beyond the scope of this paper. We speculate that \mathcal{R}_{pP} requires the proper inclusion of these effects in order to accurately describe the experimental peaks.

Lastly, in Fig. 4.12 we compare to Ref. [122]. The three layer model is, as before, very close in both peak position and intensity. Intensity is improved with the calculated spectrum at almost the same intensity as the experiment. This provides a more compelling argument against the two layer model than Fig. 4.11. The two layer model is 20 times more intense and blueshifted

by around 0.1 eV. As mentioned before, this surface is of very high quality with measurements taken shortly after surface preparation. As before, the bulk model is intermediate in both intensity and lineshape. Under these conditions, the three layer model very accurately reproduces the E_1 peak over the two layer and bulk models.

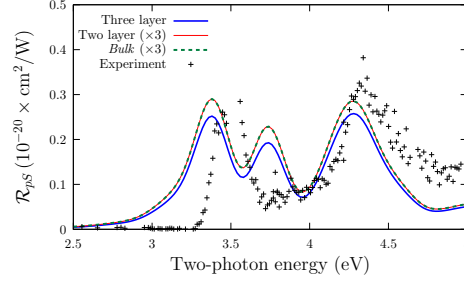


Figure 4.7: (Color online) Comparison between theoretical models (see Table 3.3) and experiment for \mathcal{R}_{pS} , for $\theta = 65^\circ$. We use a scissors value of $\hbar\Delta = 0.7$ eV. The $\chi^{\text{abc}}(-2\omega; \omega, \omega)$ components are broadened with $\sigma = 0.05$ eV, and then \mathcal{R}_{pS} is broadened with $\sigma = 0.10$ eV. Experimental data taken from Ref. [118].

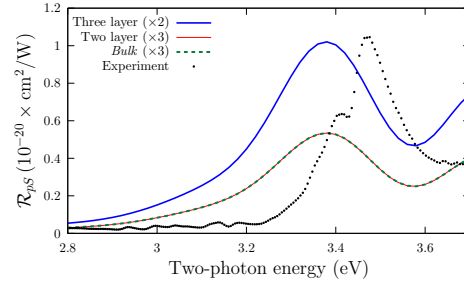


Figure 4.8: (Color online) Comparison between theoretical models (see Table 3.3) and experiment for \mathcal{R}_{pS} , for $\theta = 45^\circ$. We use a scissors value of $\hbar\Delta = 0.7$ eV. The $\chi^{\text{abc}}(-2\omega; \omega, \omega)$ components are broadened with $\sigma = 0.05$ eV, and then \mathcal{R}_{pS} is broadened with $\sigma = 0.10$ eV. Experimental data taken from Ref. [122].

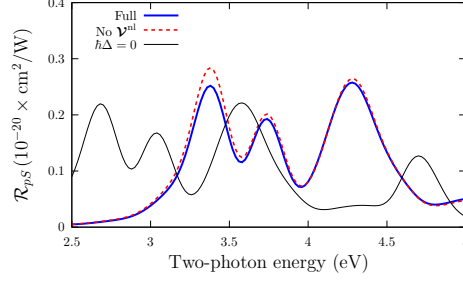


Figure 4.9: (Color online) Calculated results for \mathcal{R}_{pS} for the different levels of approximation proposed in this article. All curves were calculated using the three layer model. We take $\theta = 65^\circ$ for this plot. See text for full details. The $\chi^{\text{abc}}(-2\omega; \omega, \omega)$ components are broadened with $\sigma = 0.05$ eV, and then \mathcal{R}_{pS} is broadened with $\sigma = 0.10$ eV.

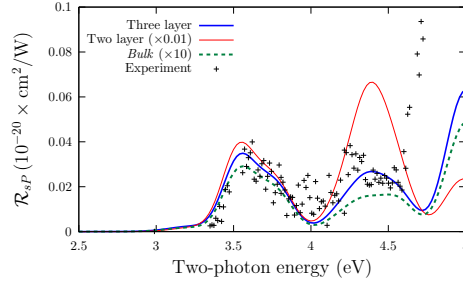


Figure 4.10: (Color online) Comparison between theoretical models (see Table 3.3) and experiment for \mathcal{R}_{sP} , for $\theta = 65^\circ$. We use a scissors value of $\hbar\Delta = 0.7$ eV. The $\chi^{\text{abc}}(-2\omega; \omega, \omega)$ components are broadened with $\sigma = 0.05$ eV, and then \mathcal{R}_{sP} is broadened with $\sigma = 0.10$ eV. Experimental data taken from Ref. [118].

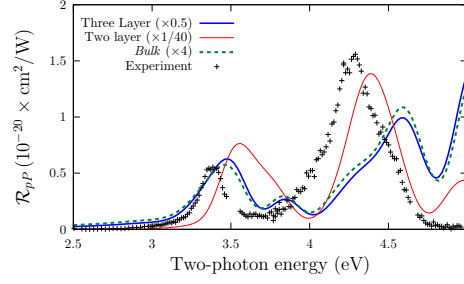


Figure 4.11: (Color online) Comparison between theoretical models (see Table 3.3) and experiment for \mathcal{R}_{pP} , for $\theta = 65^\circ$. We use a scissors value of $\hbar\Delta = 0.7$ eV. The $\chi^{\text{abc}}(-2\omega; \omega, \omega)$ components are broadened with $\sigma = 0.05$ eV, and then \mathcal{R}_{pP} is broadened with $\sigma = 0.10$ eV. Experimental data taken from Ref. [118].

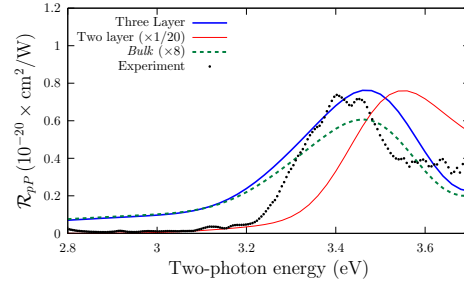


Figure 4.12: (Color online) Comparison between theoretical models (see Table 3.3) and experiment for \mathcal{R}_{pP} , for $\theta = 45^\circ$. We use a scissors value of $\hbar\Delta = 0.7$ eV. The $\chi^{\text{abc}}(-2\omega; \omega, \omega)$ components are broadened with $\sigma = 0.05$ eV, and then \mathcal{R}_{pP} is broadened with $\sigma = 0.10$ eV. Experimental data taken from Ref. [122].

BIBLIOGRAPHY

- [1] B. Baroli, M.G. Ennas, F. Loffredo, M. Isola, R. Pinna, and M.A. López-Quintela. Penetration of metallic nanoparticles in human full-thickness skin. *Journal of Investigative Dermatology*, 127(7):1701–1712, 2007.
- [2] K. Lindfors, T. Kalkbrenner, P. Stoller, and V. Sandoghdar. Detection and spectroscopy of gold nanoparticles using supercontinuum white light confocal microscopy. *Physical Review Letters*, 93(3):37401, 2004.
- [3] H. Haick. Chemical sensors based on molecularly modified metallic nanoparticles. *Journal of Physics D: Applied Physics*, 40:7173, 2007.
- [4] S. Berciaud, D. Lasne, G.A. Blab, L. Cognet, and B. Lounis. Photothermal heterodyne imaging of individual metallic nanoparticles: Theory versus experiment. *Physical Review B*, 73(4):045424, 2006.
- [5] A. Kamyshny, M. Ben-Moshe, S. Aviezer, and S. Magdassi. Ink-jet printing of metallic nanoparticles and microemulsions. *Macromolecular Rapid Communications*, 26(4):281–288, 2005.
- [6] J.R. Krenn, A. Dereux, J.C. Weeber, E. Bourillot, Y. Lacroute, J.P. Goudonnet, G. Schider, W. Gotschy, A. Leitner, and F.R. Aussenegg. Squeezing the optical near-field zone by plasmon coupling of metallic nanoparticles. *Physical Review Letters*, 82(12):2590–2593, 1999.
- [7] S. Pillai, K.R. Catchpole, T. Trupke, and M.A. Green. Surface plasmon enhanced silicon solar cells. *Journal of Applied Physics*, 101:093105, 2007.
- [8] Z.F. Li and E. Ruckenstein. Water-soluble poly (acrylic acid) grafted luminescent silicon nanoparticles and their use as fluorescent biological staining labels. *Nano Letters*, 4(8):1463–1467, 2004.
- [9] P. Figliozzi, L. Sun, Y. Jiang, N. Matlis, B. Mattern, M.C. Downer, S.P. Withrow, C.W. White, W.L. Mochán, and B.S. Mendoza. Single-beam and enhanced two-beam second-harmonic generation from silicon nanocrystals by use of spatially inhomogeneous femtosecond pulses. *Physical Review Letters*, 94(4):47401, 2005.

- [10] R.W. Boyd. *Nonlinear Optics*. Academic Press, 2003.
- [11] J.C. Diels and W. Rudolph. *Ultrashort Laser Pulse Phenomena*. Academic Press, 2006.
- [12] Y.R. Shen. *The Principles of Nonlinear Optics*, volume 1. Wiley-Interscience, 1984.
- [13] A.L. Schawlow and C.H. Townes. Infrared and optical masers. *Physical Review*, 112(6):1940–1949, Dec 1958.
- [14] P.A. Franken, A.E. Hill, C.W. Peters, and G. Weinreich. Generation of optical harmonics. *Physical Review Letters*, 7(4):118–119, Aug 1961.
- [15] J.A. Armstrong, N. Bloembergen, J. Ducuing, and P.S. Pershan. Interactions between light waves in a nonlinear dielectric. *Physical Review*, 127(6):1918–1939, Sep 1962.
- [16] N. Bloembergen and P.S. Pershan. Light waves at the boundary of nonlinear media. *Physical Review*, 128(2):606–622, Oct 1962.
- [17] R.W. Terhune, P.D. Maker, and C.M. Savage. Optical harmonic generation in calcite. *Physical Review Letters*, 8(10):404–406, May 1962.
- [18] B. Lax, J.G. Mavroides, and D.F. Edwards. Nonlinear interband and plasma effects in solids. *Physical Review Letters*, 8(4):166–168, 1962.
- [19] N. Bloembergen, R.K. Chang, S.S. Jha, and C.H. Lee. Optical second-harmonic generation in reflection from media with inversion symmetry. *Physical Review*, 174(3):813–822, Oct 1968.
- [20] C. Flytzanis and J. Ducuing. Second-order optical susceptibilities of III-V semiconductors. *Physical Review*, 178(3):1218–1228, Feb 1969.
- [21] A.E. Siegman. *Lasers*. University Science Books, 1986.
- [22] C.K. Chen, A.R.B. de Castro, and Y.R. Shen. Surface-enhanced second-harmonic generation. *Physical Review Letters*, 46(2):145–148, Jan 1981.
- [23] P. Guyot-Sionnest and Y.R. Shen. Bulk contribution in surface second-harmonic generation. *Physical Review B*, 38(12):7985–7989, Oct 1988.
- [24] Y.R. Shen. Surface properties probed by second-harmonic and sum-frequency generation. *Nature*, 337(6207):519–525, February 1989.

- [25] J.L.P. Hughes and J.E. Sipe. Calculation of second-order optical response in semiconductors. *Physical Review B*, 53(16):10751–10763, Apr 1996.
- [26] B.S. Mendoza and W.L. Mochán. Exactly solvable model of surface second-harmonic generation. *Physical Review B*, 53(8):4999–5006, Feb 1996.
- [27] B.S. Mendoza, W.L. Mochán, and J.A. Maytorena. Visible-infrared sum and difference frequency generation at adsorbate-covered Au. *Physical Review B*, 60(20):14334–14340, Nov 1999.
- [28] B.S. Mendoza and W.L. Mochán. Polarizable-bond model for second-harmonic generation. *Physical Review B*, 55(4):2489–2502, Jan 1997.
- [29] J.A. Maytorena, B.S. Mendoza, and W.L. Mochán. Theory of surface sum frequency generation spectroscopy. *Physical Review B*, 57(4):2569–2579, Jan 1998.
- [30] M.C. Downer, Y. Jiang, D. Lim, L. Mantese, P.T. Wilson, B.S. Mendoza, and V.I. Gavrilenko. Optical second harmonic spectroscopy of silicon surfaces, interfaces and nanocrystals. *Physica Status Solidi A*, 188(4):1371–1381, 2001.
- [31] G. Lüpke. Characterization of semiconductor interfaces by second-harmonic generation. *Surface Science Reports*, 35(3-4):75 – 161, 1999.
- [32] P.F. Moulton. Spectroscopic and laser characteristics of $\text{Ti:Al}_2\text{O}_3$. *Journal of the Optical Society of America B*, 3(1):125–133, Jan 1986.
- [33] D. Strickland and G. Mourou. Compression of amplified chirped optical pulses. *Optics Communications*, 55(6):447 – 449, 1985.
- [34] A.M. Janner. *Second-Harmonic Generation, a Selective Probe for Excitons*. PhD thesis, 1998.
- [35] N. Bloembergen. Surface nonlinear optics: A historical overview. *Applied Physics B: Lasers and Optics*, 68(3):289–293, 1999.
- [36] J.E. Sipe, V. Mizrahi, and G.I. Stegeman. Fundamental difficulty in the use of second-harmonic generation as a strictly surface probe. *Physical Review B*, 35(17):9091–9094, 1987.

- [37] Y.R. Shen. Surface contribution versus bulk contribution in surface nonlinear optical spectroscopy. *Applied Physics B: Lasers and Optics*, 68(3):295–300, 1999.
 - [38] J.F. McGilp. A review of optical second-harmonic and sum-frequency generation at surfaces and interfaces. *Journal of Physics D: Applied Physics*, 29:1812, 1996.
 - [39] J.F. McGilp. Second-harmonic generation at semiconductor and metal surfaces. *Surface Review and Letters*, 6(3-4):529–558, 1999.
 - [40] O.A. Aktsipetrov, A.A. Fedyanin, A.V. Melnikov, J.I. Dadap, X.F. Hu, M.H. Anderson, M.C. Downer, and J.K. Lowell. D.C. electric field induced second-harmonic generation spectroscopy of the Si(001)-SiO₂ interface: Separation of the bulk and surface non-linear contributions. *Thin Solid Films*, 294(1-2):231–234, 1997.
 - [41] T. Scheidt, E.G. Rohwer, H.M. von Bergmann, and H. Stafast. Optical second harmonic imaging: A versatile tool to investigate semiconductor surfaces and interfaces. *The European Physical Journal Applied Physics*, 27(1-3):393–397, 2004.
 - [42] R. Huber, H. Satzger, W. Zinth, and J. Wachtveitl. Noncollinear optical parametric amplifiers with output parameters improved by the application of a white light continuum generated in CaF₂. *Optics Communications*, 194(4-6):443–448, 2001.
 - [43] J. Wei, A. Wirth, M.C. Downer, and B.S. Mendoza. Second-harmonic and linear optical spectroscopic study of silicon nanocrystals embedded in SiO₂. *Physical Review B*, 84:165316, Oct 2011.
 - [44] N. Bodnar. A dual-pumping geometry for non-collinear optical parametric amplification. *Electrical Engineering*, 2010.
 - [45] G.M. Gale, M. Cavallari, T.J. Driscoll, and F. Hache. Sub-20-fs tunable pulses in the visible from an 82-MHz optical parametric oscillator. *Optics Letters*, 20(14):1562–1564, 1995.
 - [46] T. Wilhelm, J. Piel, and E. Riedle. Sub-20-fs pulses tunable across the visible from a blue-pumped single-pass noncollinear parametric converter. *Optics Letters*, 22(19):1494–1496, 1997.
 - [47] C.K. Lee. Cascaded nonlinear optical mixing in a noncollinear optical parametric amplifier. *Advances in Optical Amplifiers*, 2011.
-

- [48] J.I. Dadap, J. Shan, K.B. Eisenthal, and T.F. Heinz. Second-harmonic Rayleigh scattering from a sphere of centrosymmetric material. *Physical Review Letters*, 83(20):4045–4048, 1999.
 - [49] J.I. Dadap, J. Shan, and T.F. Heinz. Theory of optical second-harmonic generation from a sphere of centrosymmetric material: Small-particle limit. *Journal of the Optical Society of America B*, 21(7):1328–1347, 2004.
 - [50] J. Shan, J.I. Dadap, I. Stiopkin, G.A. Reider, and T.F. Heinz. Experimental study of optical second-harmonic scattering from spherical nanoparticles. *Physical Review A*, 73(2):023819, 2006.
 - [51] V.L. Brudny, B.S. Mendoza, and W.L. Mochán. Second-harmonic generation from spherical particles. *Physical Review B*, 62(16):11152, 2000.
 - [52] W.L. Mochán, J.A. Maytorena, B.S. Mendoza, and V.L. Brudny. Second-harmonic generation in arrays of spherical particles. *Physical Review B*, 68(8):085318, 2003.
 - [53] M.W. Klein, M. Wegener, N. Feth, and S. Linden. Experiments on second-and third-harmonic generation from magnetic metamaterials. *Optics Express*, 15(8):5238–5247, 2007.
 - [54] N. Feth, S. Linden, M.W. Klein, M. Decker, F.B.P. Niesler, Y. Zeng, W. Hoyer, J. Liu, S.W. Koch, and J.V. Moloney. Second-harmonic generation from complementary split-ring resonators. *Optics Letters*, 33(17):1975–1977, 2008.
 - [55] Y. Zeng, W. Hoyer, J. Liu, S.W. Koch, and J.V. Moloney. Classical theory for second-harmonic generation from metallic nanoparticles. *Physical Review B*, 79(23):235109, 2009.
 - [56] S. Link and M.A. El-Sayed. Optical properties and ultrafast dynamics of metallic nanocrystals. *Annual Review of Physical Chemistry*, 54(1):331–366, 2003.
 - [57] S. Cattaneo and M. Kauranen. Determination of second-order susceptibility components of thin films by two-beam second-harmonic generation. *Optics Letters*, 28(16):1445–1447, 2003.
-

- [58] F.X. Wang, F.J. Rodríguez, W.M. Albers, R. Ahorinta, J.E. Sipe, and M. Kauranen. Surface and bulk contributions to the second-order nonlinear optical response of a gold film. *Physical Review B*, 80(23):233402, 2009.
- [59] A. Wirth, J. Wei, J.J.H. Gielis, P. Figliozzi, J. Rafaelsen, Y.Q. An, and M.C. Downer. Second-harmonic spectroscopy of Si nanocrystals embedded in silica. *Physica Status Solidi C*, 5(8):2662–2666, 2008.
- [60] L. Sun, P. Figliozzi, Y.Q. An, M.C. Downer, W.L. Mochan, and B.S. Mendoza. Quadrupolar SHG enhancement in isotropic materials using two orthogonally polarized laser beams. In *Quantum Electronics and Laser Science Conference*, volume 1, pages 274–276. IEEE, 2005.
- [61] M. C. Downer, B. S. Mendoza, and V. I. Gavrilenko. Optical second harmonic spectroscopy of semiconductor surfaces: advances in microscopic understanding. *Surf. Interface Anal.*, 31(10):966–986, 2001.
- [62] G. Lüpke. Characterization of semiconductor interfaces by second-harmonic generation. *Surf. Sci. Rep.*, 35(3):75–161, 1999.
- [63] B. S. Mendoza, M. Palummo, G. Onida, and R. Del Sole. Ab initio calculation of second-harmonic-generation at the si(100) surface. *Phys. Rev. B*, 63(20):205406, 2001.
- [64] D. Lim, M. C. Downer, J. G. Ekerdt, N. Arzate, B. S. Mendoza, V. I. Gavrilenko, and R. Q. Wu. Optical second harmonic spectroscopy of boron-reconstructed si (001). *Phys. Rev. Lett.*, 84(15):3406–3409, 2000.
- [65] V. I. Gavrilenko, R. Q. Wu, M. C. Downer, J. G. Ekerdt, D. Lim, and P. Parkinson. Optical second harmonic spectra of silicon-adatom surfaces: theory and experiment. *Thin Solid Films*, 364(1):1–5, 2000.
- [66] B. S. Mendoza, W. L. Mochán, and J. A. Maytorena. Visible-infrared sum and difference frequency generation at adsorbate-covered au. *Phys. Rev. B*, 60(20):14334, 1999.
- [67] B. S. Mendoza, A. Gaggiotti, and R. Del Sole. Microscopic theory of second harmonic generation at si (100) surfaces. *Phys. Rev. Lett.*, 81(17):3781–3784, 1998.

- [68] B. S. Mendoza and W. L. Mochán. Local-field effect in the second-harmonic-generation spectra of Si surfaces. *Phys. Rev. B*, 53(16):10473–10476, 1996.
- [69] B. S. Mendoza and W. L. Mochán. Polarizable-bond model for second-harmonic generation. *Phys. Rev. B*, 55(4):2489, 1997.
- [70] P. Guyot-Sionnest, A. Tadjeddine, and A. Liebsch. Electronic distribution and nonlinear optical response at the metal-electrolyte interface. *Phys. Rev. Lett.*, 64(14):1678–1681, 1990.
- [71] B. S. Mendoza. Longitudinal Gauge Theory of Second Harmonic Generation at Semiconductor Surfaces. In *Epioptics-7: Proceedings of the 24th Course of the International School of Solid State Physics: Erice, Italy, 20-26 July 2002*, volume 23, page 52, 2004.
- [72] N. Arzate and B. S. Mendoza. Microscopic study of surface second-harmonic generation from a clean si(100) c(4×2) surface. *Phys. Rev. B*, 63(12):125303, 2001.
- [73] C. Aversa and J. E. Sipe. Nonlinear optical susceptibilities of semiconductors: Results with a length-gauge analysis. *Phys. Rev. B*, 52(20):14636–14645, 1995.
- [74] J. E. Sipe and A. I. Shkrebtii. Second-order optical response in semiconductors. *Phys. Rev. B*, 61(8):5337, 2000.
- [75] W. R. L. Lambrecht and S. N. Rashkeev. From band structures to linear and nonlinear optical spectra in semiconductors. *Phys. Status Solidi B*, 217(1):599–640, 2000.
- [76] E. N. Adams. The crystal momentum as a quantum mechanical operator. *J. Chem. Phys.*, 21(11):2013–2017, November 1953.
- [77] E. I. Blount, F. Seitz, and D. Turnbull. Formalisms of band theory. *Solid State Phys.*, 13:305, 1962.
- [78] S. Ismail-Beigi, E. K. Chang, and S. G. Louie. Coupling of nonlocal potentials to electromagnetic fields. *Phys. Rev. Lett.*, 87(8):087402, August 2001.
- [79] C. Motta, M. Giantomassi, M. Cazzaniga, K. Gaál-Nagy, and X. Gonze. Implementation of techniques for computing optical properties in 0-3 dimensions, including a real-space cutoff, in ABINIT. *Comput. Mater. Sci.*, 50(2):698–703, 2010.

- [80] L. Kleinman and D. M. Bylander. Efficacious form for model pseudopotentials. *Phys. Rev. Lett.*, 48(20):1425–1428, 1982.
- [81] B. Adolph, V. I. Gavrilenko, K. Tenelsen, F. Bechstedt, and R. Del Sole. Nonlocality and many-body effects in the optical properties of semiconductors. *Phys. Rev. B*, 53(15):9797–9808, 1996.
- [82] L. Reining, R. Del Sole, M. Cini, and J. G. Ping. Microscopic calculation of second-harmonic generation at semiconductor surfaces: As/Si(111) as a test case. *Phys. Rev. B*, 50(12):8411–8422, 1994.
- [83] H. Sano, G. Mizutani, W. Wolf, and R. Podloucky. Ab initio study of linear and nonlinear optical responses of si(111) surfaces. *Phys. Rev. B*, 66(19):195338, November 2002.
- [84] J. E. Mejía, B. S. Mendoza, and C. Salazar. Layer-by-layer analysis of second harmonic generation at a simple surface. *Revista Mexicana de Física*, 50(2):134–139, 2004.
- [85] C. Hogan, R. Del Sole, and G. Onida. Optical properties of real surfaces from microscopic calculations of the dielectric function of finite atomic slabs. *Phys. Rev. B*, 68(3):035405, 2003.
- [86] C. Castillo, B. S. Mendoza, W. G. Schmidt, P. H. Hahn, and F. Bechstedt. Layer-by-layer analysis of surface reflectance anisotropy in semiconductors. *Phys. Rev. B*, 68(4):041310, 2003.
- [87] B. S. Mendoza, F. Nastos, N. Arzate, and J. Sipe. Layer-by-layer analysis of the linear optical response of clean and hydrogenated si(100) surfaces. *Phys. Rev. B*, 74(7):075318, 2006.
- [88] Nicolas Tancogne-Dejean private communication. Indeed, one can compute the layered contribution of the non-local contribution to \mathbf{v} with an analytic expression. However, one needs to compute this within the DP code.
- [89] S. N. Rashkeev, W. R. L. Lambrecht, and B. Segall. Efficient ab initio method for the calculation of frequency-dependent second-order optical response in semiconductors. *Phys. Rev. B*, 57(7):3905–3919, 1998.
- [90] Valérie Vénier, E. Luppi, and H. Hübener. unpublished.

- [91] Neil W. Ashcroft and N. David Mermin. *Solid State Physics*. Saunders College, Philadelphia, 1976.
- [92] Robert W. Boyd. *Nonlinear Optics*. AP, New York, 2007.
- [93] Michele Cini. Simple model of electric-dipole second-harmonic generation from interfaces. *Physical Review B*, 43(6):4792–4802, February 1991.
- [94] V. Mizrahi and J. E. Sipe. Phenomenological treatment of surface second-harmonic generation. *J. Opt. Soc. Am. B*, 5(3):660–667, 1988.
- [95] J. E. Sipe. New Green-function formalism for surface optics. *Journal of the Optical Society of America B*, 4(4):481–489, 1987.
- [96] J. E. Sipe, D. J. Moss, and H. M. van Driel. Phenomenological theory of optical second- and third-harmonic generation from cubic centrosymmetric crystals. *Phys. Rev. B*, 35(3):1129–1141, January 1987.
- [97] S. V. Popov, Yu. P. Svirko, and N. I. Zheludev. *Susceptibility Tensors for NonLinear Optics*. IOP, Bristol, 1995.
- [98] The half-slab layer extends to the middle of the vacuum region between consecutive (front-back or back-front) surfaces of the repeated super cell scheme.
- [99] The ABINIT code is a common project of the Université Catholique de Louvain, Corning Incorporated, and other contributors (URL <http://www.abinit.org>).
- [100] N. Troullier and J. L. Martins. Efficient pseudopotentials for plane-wave calculations. *Phys. Rev. B*, 43(3):1993–2006, January 1991.
- [101] V. Olevano, L. Reining, and F. Sottile. <http://dp-code.org>.
- [102] L. Caramella, C. Hogan, G. Onida, and R. Del Sole. High-resolution electron energy loss spectra of reconstructed si(100) surfaces: First-principles study. *Phys. Rev. B*, 79:155447, Apr 2009.
- [103] For bulk calculations schemes of the SH susceptibility tensor beyond the independent particle approximation see for instance Refs. [112, 111, 110, 127, 128, 129, 130, 131].

- [104] F. Nastos, B. Olejnik, K. Schwarz, and J. E. Sipe. Scissors implementation within length-gauge formulations of the frequency-dependent nonlinear optical response of semiconductors. *Phys. Rev. B*, 72(4):045223, 2005.
- [105] M. Rohlfing, P. Krüger, and J. Pollmann. Efficient scheme for GW quasiparticle band-structure calculations with applications to bulk si and to the si(001)-(21) surface. *Phys. Rev. B*, 52(3):1905–1917, July 1995.
- [106] P. García-González and R. W. Godby. GW self-energy calculations for surfaces and interfaces. 137(1):108–122, June 2001.
- [107] Eleonora Luppi, Hans-Christian Weissker, Sandro Bottaro, Sottile Francesco, Valérie Vénard, Lucia Reining, and Giovanni Onida. Accuracy of the pseudopotential approximation in *ab initio* theoretical spectroscopies. *Phys. Rev. B*, 78:245124, 2008.
- [108] R. Asahi, W. Mannstadt, and A. J. Freeman. Screened-exchange lda methods for films and superlattices with applications to the si(100)2x1 surface and inasinsb superlattices. *Phys. Rev. B*, 62:2552, 2000.
- [109] J. Cabellos, B. Mendoza, M. Escobar, F. Nastos, and J. Sipe. Effects of nonlocality on second-harmonic generation in bulk semiconductors. *Phys. Rev. B*, 80(15):155205, 2009.
- [110] E. Luppi, H. Hübener, and V. Vénard. Ab initio second-order nonlinear optics in solids: Second-harmonic generation spectroscopy from time-dependent density-functional theory. *Phys. Rev. B*, 82:235201, 2010.
- [111] R. Leitsmann, W. Schmidt, P. Hahn, and F. Bechstedt. Second-harmonic polarizability including electron-hole attraction from band-structure theory. *Phys. Rev. B*, 71(19):195209, 2005.
- [112] B. Adolph and F. Bechstedt. Influence of crystal structure and quasiparticle effects on second-harmonic generation: Silicon carbide polytypes. *Phys. Rev. B*, 62:1706, 2000.
- [113] X. Gonze, B. Amadon, P. . M. Anglade, J. . M. Beuken, F. Bottin, P. Boulanger, F. Bruneval, D. Caliste, R. Caracas, M. Cote, T. Deutsch, L. Genovese, Ph. Ghosez, M. Giantomassi, S. Goedecker, D. R. Hamann, P. Hermet, F. Jollet, G. Jomard, S. Leroux, M.

- Mancini, S. Mazevet, M. J. T. Oliveira, G. Onida, Y. Pouillon, T. Rangel, G. . M. Rignanese, D. Sangalli, R. Shaltaf, M. Torrent, M. J. Verstraete, G. Zerah, and J. W. Zwanziger. ABINIT: First-principles approach to material and nanosystem properties. *Comput. Phys. Commun.*, 180(12):2582–2615, December 2009.
- [114] E. Kaxiras and J. D. Joannopoulos. Hydrogenation of semiconductor surfaces: Si and Ge (111). *Phys. Rev. B*, 37(15):8842–8848, May 1988.
- [115] F. Jona, W. A. Thompson, and P. M. Marcus. Experimental determination of the atomic structure of a H-terminated Si(111) surface. *Phys. Rev. B*, 52(11):8226–8230, September 1995.
- [116] D. R. Alfonso, C. Noguez, D. A. Drabold, and S. E. Ulloa. First-principles studies of hydrogenated Si(111)-7 \times 7. *Phys. Rev. B*, 54(11):8028–8032, September 1996.
- [117] F. Cargnoni, C. Gatti, E. May, and D. Narducci. Geometrical reconstructions and electronic relaxations of silicon surfaces. I. An electron density topological study of H-covered and clean Si(111)(1 \times 1) surfaces. *J. Chem. Phys.*, 112(2):887–899, January 2000.
- [118] J. E. Mejía, B. S. Mendoza, M. Palummo, G. Onida, R. Del Sole, S. Bergfeld, and W. Daum. Surface second-harmonic generation from si (111)(1 \times 1) h: Theory versus experiment. *Phys. Rev. B*, 66(19):195329, 2002.
- [119] R. C. Weast, M. J. Astle, and W. H. Beyer. *CRC handbook of chemistry and physics*, volume 69. CRC press Boca Raton, FL, 1988.
- [120] Y. Li and G. Galli. Electronic and spectroscopic properties of the hydrogen-terminated Si(111) surface from ab initio calculations. *Phys. Rev. B*, 82(4):045321, July 2010.
- [121] U. Höfer. Nonlinear optical investigations of the dynamics of hydrogen interaction with silicon surfaces. *Appl. Phys. A*, 63(6):533–547, December 1996.
- [122] S. A. Mitchell, M. Mehendale, D. M. Villeneuve, and R. Boukherroub. Second harmonic generation spectroscopy of chemically modified Si(111) surfaces. *Surf. Sci.*, 488(3):367–378, August 2001.

- [123] S. Bergfeld, B. Braunschweig, and W. Daum. Nonlinear Optical Spectroscopy of Suboxides at Oxidized Si(111) Interfaces. *Phys. Rev. Lett.*, 93(9):097402, August 2004.
- [124] J. I. Dadap, X. F. Hu, M. H. Anderson, M. C. Downer, J. K. Lowell, and O. A. Aktsipetrov. Optical second-harmonic electroreflectance spectroscopy of a Si(001) metal-oxide-semiconductor structure. *Phys. Rev. B*, 53(12):R7607–R7609, March 1996.
- [125] Nicolas Tancogne-Dejean. *Ab initio description of second-harmonic generation from crystal surfaces*. PhD thesis, Ecole polytechnique, September 2015.
- [126] S. M. Anderson, N. Tancogne-Dejean, B. S. Mendoza, and V. Vénard. Theory of surface second-harmonic generation for semiconductors including effects of nonlocal operators. *Phys. Rev. B*, 91(7):075302, February 2015.
- [127] E. Luppi, H. Hübener, and V. Vénard. Communications: Ab initio second-order nonlinear optics in solids. *J. Chem. Phys.*, 132(24):241104, 2010.
- [128] H. Hübener, E. Luppi, and V. Vénard. Ab initio calculation of many-body effects on the second-harmonic generation spectra of hexagonal silic polytypes. *Phys. Rev. B*, 83:115205, 2011.
- [129] Mads L. Trolle, Gotthard Seifert, and Thomas G. Pedersen. Theory of excitonic second-harmonic generation in monolayer MoS₂. *Phys. Rev. B*, 89(23):235410, June 2014.
- [130] C. Attacalite and M. Grüning. Nonlinear optics from an ab initio approach by means of the dynamical berry phase: Application to second- and third-harmonic generation in semiconductors. *Phys. Rev. B*, 88:235113, 2013.
- [131] M. Grüning and C. Attacalite. Second harmonic generation in *h*-bn and mos₂ monolayers: Role of electron-hole interaction. *Phys. Rev. B*, 89:081102, 2014.